UNIVERSITÄT PADERBORN
Die Universität der Informationsgesellschaft

FACULTY OF SCIENCE
DEPARTMENT OF PHYSICS

DISSERTATION

Down- and Up-Conversion in Fluorozirconate-Based Glasses and Glass Ceramics for Photovoltaic Application

BERND AHRENS

PADERBORN
2009

Abstract

Sol omnibus lucet.
Satyricon, 100
TITUS PETRONIUS

Mono-gap solar cells, like commercial silicon solar cells, are unable to use the whole solar spectrum. In particular, photons with high energy have thermalization losses and photons with an energy lower than the bandgap energy can not be absorbed. Materials, which convert one UV photon into one or more visible photons, so called down-converters, or which convert two or more sub-bandgap photons into photons with an energy higher than the bandgap energy, so called up-converters, are of great interest for photovoltaic applications.

In this work new materials were investigated for their optical properties and their potential as down- or up-converters.

For down-conversion applications, barium chloride and barium bromide single crystals, as well as fluorozirconate-based (FZ) glasses, were doped with samarium. The glasses were additionally doped with bromide ions in order to initiate the formation of barium bromide nanocrystals in the glass upon thermal processing. Optical measurement techniques determined the divalent charge state of samarium in both single crystals. The FZ glasses show a different behavior: samarium enters the glass matrix either in its divalent or in its trivalent state. Fluorescence measurements indicate that during the annealing process Sm^{2+} ions enter the nanocrystals leading to enhanced fluorescence efficiency and to changes in the fluorescence lifetime.

For up-conversion applications, $BaCl_2$ single crystals, as well as FZ-based glasses, were doped with neodymium. Upon excitation at 796 nm, Nd^{3+}-doped $BaCl_2$ single crystals show several up-converted fluorescence bands in the visible spectral range, with the most intense bands at 530, 590, and 660 nm, in addition to the typical fluorescence bands in the infrared spectral range. The power dependence of the infrared fluorescence and of the two-photon

up-conversion fluorescence intensities as well as the corresponding radiative lifetimes have been investigated. An enhanced up-converted fluorescence in Nd^{3+}-doped fluorozirconate (FZ) glasses which were additionally doped with chlorine ions was found. Upon annealing between 240 and 290 °C, hexagonal phase $BaCl_2$ nanocrystals between 20 and 180 nm in diameter were formed in the glass. During thermal processing, some of the Nd^{3+} ions enter the nanocrystals leading to additional splitting of the up-converted fluorescence and infrared fluorescence spectra.

Nd-doped glass ceramics are useful as a model system, but are not applicable due to the excitation of the up-conversion at $\sim$ 800 nm, which is light that can be absorbed by a silicon solar cell itself. However, erbium-doped FZ glasses were found to be more applicable systems for up-conversion-based silicon solar cells due to their excitation at 1540 nm. To show their potential the external quantum efficiency (EQE) of a commercial monocrystalline silicon solar cell with an Er-doped FZ glass on top of it was determined. For an excitation power of 18 mW at a wavelength of 1540 nm an EQE of almost 1.5 % was found for a 5 mol % Er-doped FZ glass.

Contents

1 Introduction

One of today's major challenges is the energy managing a supply of power for an growing population. Due to the limited supply of energy sources, like coal, oil, gas, or uranium, a replacement of most currently used power supplies with renewable energy sources is paramount. Even in the case of an infinite amount of these fossil fuels, using them is harmful to the earth due to the creation of global warming. Today, about $28 \cdot 10^{12}$ kg of CO_2 per year [1], a daily output of 76 million tonnes, are released in the atmosphere. "First effects of global warming are already visible and determined action is required to restrict the negative consequences for mankind, the environment and subsequent generations. Renewable energies are essential contributors to the energy supply portfolio as they provide opportunities for mitigating greenhouse gases" [2]. The renewable energy sources include water, geothermal, wind, and solar [1].

Solar cells convert solar radiation into electrical energy, by the photovoltaic effect, first reported by Becquerel [3] in 1839. Today a commercial silicon solar cell has an efficiency of around 22 % [4]; ratio of incident to useable energy. The two major loss mechanisms (see figure 1.1) are thermalization losses due to high energy photons and transmission losses of sub band gap photons. Ther-

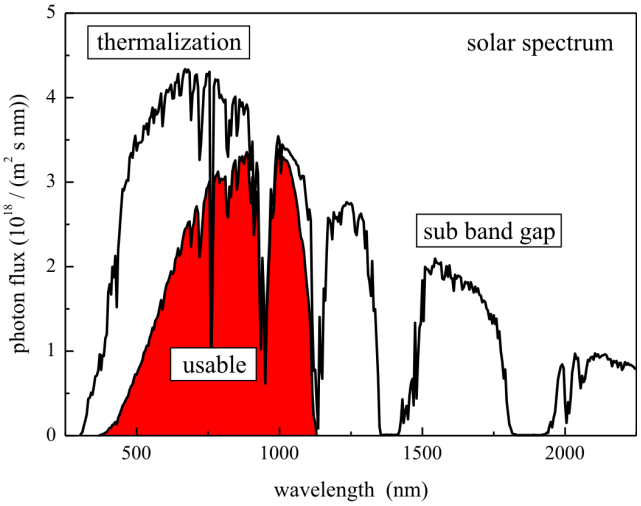

Figure 1.1: Solar spectrum AM1.5. The red area can be used by a commercial silicon solar cell to generate current. The number of photons per square-meter, second and nanometer are plotted versus the wavelength.

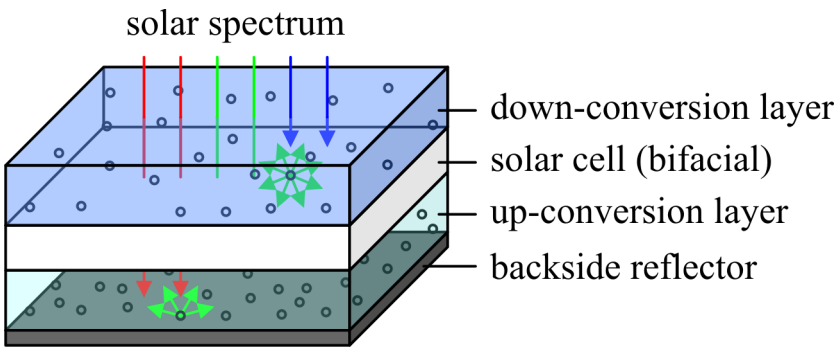

Figure 1.2: Bifacial solar cell with down- and up-converter.

malization losses can be reduced significantly in a solar cell when more than one electron-hole pair is generated per incident photon. A maximum EQE of nearly 40 % for a silicon solar cell can be theoretically achieved [5] by using a down-converter with a high band gap solar cell. With an up-converting layer it is possible to use sub band gap light that cannot be absorbed by the solar cell to generate high energy photons that can be absorbed. Trupke, Green, and Würfel found the upper EQE limit of up-conversion solar cell systems can be enhanced to 47.6 % for single junction cells [6]. Gibart *et al.* [7] reported in 1996 the first application of an up-converter on a bifacial gallium arsenide solar cell. Seven years later Shalav *et al.* [8] demonstrated the first up-converter on a silicon solar cell. A schematic system containing, down- and up-converter with a bifacial solar cell is shown in figure 1.2.

A brief introduction to the background on down- and up-conversion, rare earth ions, fluorozirconate based glasses and thermal treatment is given in chapter 2 along with methods like photoluminescence and x-ray diffraction. In chapter 3 the results of Sm-doped materials for down-converting processes are shown. Part one deals with $BaCl_2$ and $BaBr_2$ single crystals doped with divalent Sm. These investigations are the basis for the glass ceramics in part two, where $BaCl_2$ and $BaBr_2$ nanoparticles are formed in the glasses to enhance their optical properties. The results of the Nd-doped single crystals ($BaCl_2$) and glass ceramics are presented in chapter 4 section one. In the second section results on erbium doping are presented. Conclusions are presented in in chapter 5.

Parts of the present work have already been published; a publication list is added at the end of this thesis in the appendix.

2 Basics - Physical Background

2.1 Photon Conversion

2.1.1 Down-Conversion and Quantum Cutting

The process of down-conversion or down-shifting describes the conversion of one high-energy photon (e.g. UV-photon) into one photon with a lower energy (e.g. a visible photon) - normally called photoluminescence (PL). By absorbing a photon an optically active center (e.g. an ion) goes into an excited state. By emitting one photon with the same or less energy compared to the exciting one the ground state can be reached. Quantum cutting occurs if one high-energy photon is converted into two or more photons with lower energies. In 1974 Sommerdijk *et al.* [11] and Piper *et al.* [12] observed after a high energy excitation a subsequent emission of two photons (photo cascade emission) in YF_3:Pr^{3+} and $NaYF_4$:Pr^{3+}. A luminescent quantum efficiency of nearly 140 % was observed for this process. Quantum cutting can be realized by a single ion or by a combination of centers due to energy transfers. The first case is based on one optically active center with three energy levels. Excited to state E_2, the ion subsequently emits two photons to relax stepwise into the ground state (see figure 2.1 (a)). The second possibility is to obtain quantum cutting uses two ions. The excited ion (I) can relax from state E_2 into E_1 by energy transfer to the second ion (II), shown in figure 2.1 (b). After the energy transfer both ions can emit a photon to reach the ground state. The energy resonance condition had to be fulfilled - meaning that the energy difference for the energy transfer transitions in both ions have to be equal. A well known example for this type of quantum cutting is an Eu-Gd-system, which is shown in figure 2.2 [9, 10]. In the third concept, shown in figure 2.1 (c), quantum cutting occurs by the use of three optically active centers. Ion (I) is excited by a photon. Through a co-operative sensitization the energy can be transferred simultaneously to two nearby centers (II + III). After the energy is transferred these centers both emit a photon.

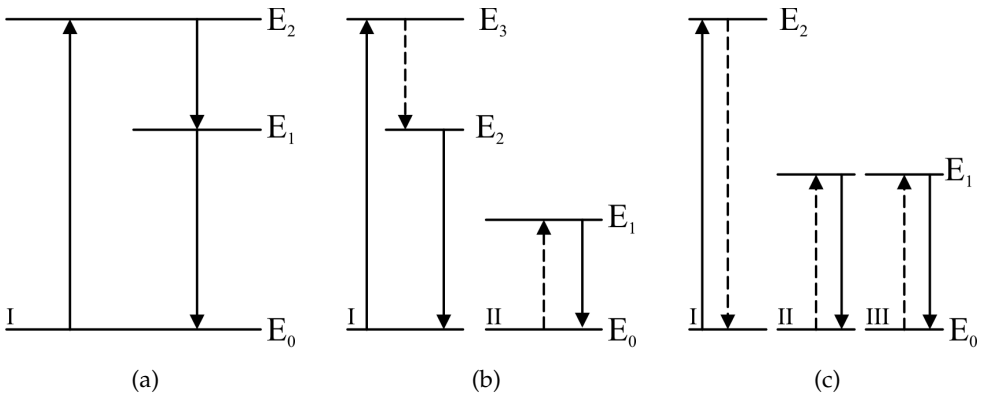

Figure 2.1: Concepts of quantum cutting. Relaxation and excitation by energy transfers were marked as dashed arrows. (a) One optically active center (ion) subsequently emits two photons after being excited into the energy level E_2. In (b) quantum cutting with two ions is shown. After an energy transfer both ions emit a photon. Using three ions, the excited ion (I) can relax into the ground state, E_0, by transferring the energy to two nearby ions - shown in (c).

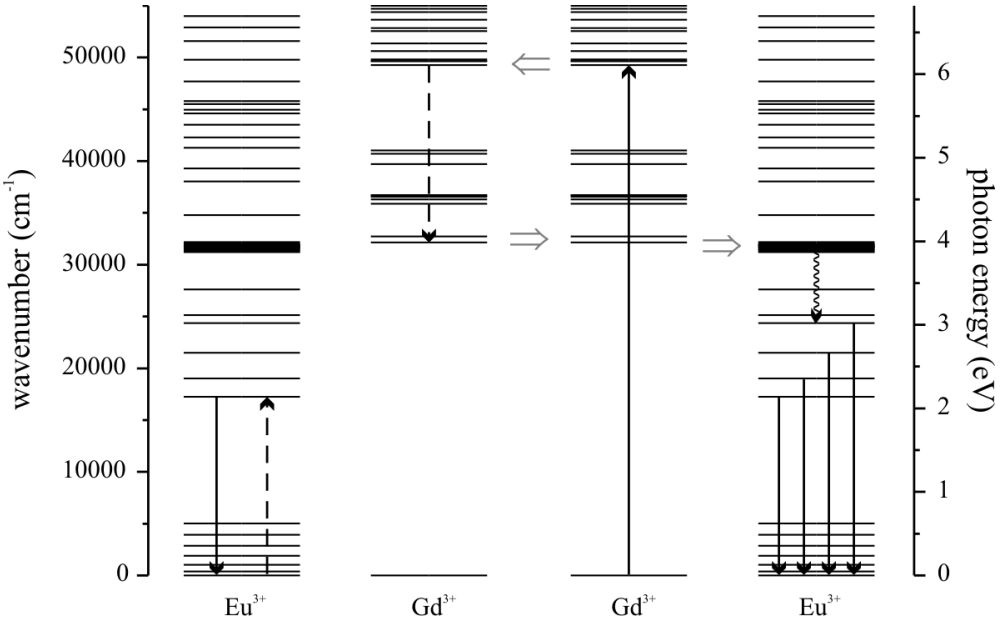

Figure 2.2: Energy level diagram for a Gd^{3+}-Eu^{3+} system, showing the possibility for visible quantum cutting by two-step energy transfer from Gd^{3+} to Eu^{3+} upon excitation in the ^6G_J levels of Gd^{3+} [9, 10]

2.1.2 Up-Conversion

The process of frequency-up-conversion describes the conversion of two or more low-energy photons (e.g. IR-photons) into one or more photons with a higher energy (e.g. a visible photon). The sum of the energies of the absorbed photons must be greater or equal to the energies of the emitted photons, i.e.

$$\sum_n E_{\text{emitted},n} \quad = \quad \sum_n E_{\text{absorbed},n} + E_{\text{loss}}. \tag{2.1}$$

The up-conversion-processes can occur via three mechanisms. These mechanisms are excited-state-absorption, direct two-photon-absorption, and energy-transfer-up-conversion [13].

Excited-State-Absorption: ESA

Excited-state-absorption is a single-ion process. Initially the ion is in its ground-state (E_0). A photon with an energy E_2 is absorbed. After the first absorption and a possible radiationless relaxation into a metastable state (dashed arrow, figure 2.3, another photon with an energy which is equal to the energy difference of the E_1 and E_3 levels is absorbed and leads to a second transition. The ion gets from this (metastable) state E_1 into a higher energy level E_3. This is shown in figure 2.3(a). The subsequent relaxation to the ground state can be observed as up-converted fluorescence. The energy of the final state is almost equal to the sum of the two-photon energies.

Direct Two-Photon-Absorption: TPA

The direct two-photon-absorption is also a single-ion process. Two photons containing in the sum the energy of the excited state E_1 are simultaneously absorbed upon exciting the ion into a virtual intermediate excited state. This virtual state is indicated by the dashed line in figure 2.3(b).

Energy-Transfer-Up-Conversion: ETU

Two kinds of energy transfers are considered here. First, there is the *cross relaxation* between ions in their excited states. In this case, the energy absorbed by the first ion (**I**) is transferred to the second ion (**II**), which is already in an excited state, and reaches by this way the final state (see figure 2.3). In the second case – *cooperative sensitization* – the energy, accumulated by two excited ions, is transferred by the relaxation of these two ions to a third ion. The time dependence of the anti-Stokes fluorescence, which may be calculated using rate equations, does not only depend on the final-state relaxations, but also on the relaxation rates of the intermediate states and the energy transfer probability. Auzel *et al.* [14] have shown that excited-state absorption and energy

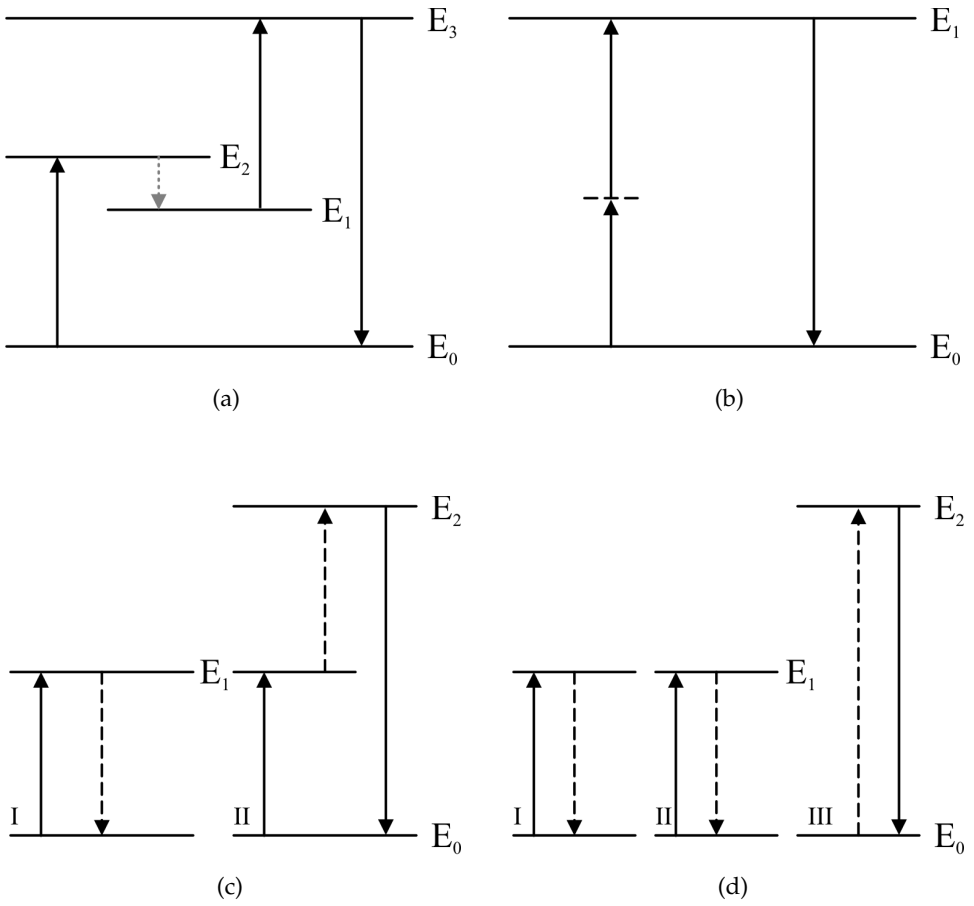

Figure 2.3: (a) Scheme of the ESA-process. Stepwise absorption of photons excite the ion into a higher energy level E_3. (b) Illustration of the TPA-up-conversion-process. The excited state is reached via a virtual state by simultaneous absorption. (c) shows the cross-relaxation at the ETU-process. While one ion (**I**) is relaxing into the ground state another ion (**II**) is excited in an energetically higher level. The cooperative sensitization (ETU) is shown in (d). A third ion (**III**) is excited by the relaxation of two other ions (**I+II**). Relaxation and excitation by energy transfers were marked as dashed arrows.

mechanism	efficiency
ETU cross relaxation	$\sim 10^{-3}$
Excited State Absorption (ESA)	$\sim 10^{-5}$
ETU cooperative sensitization	$\sim 10^{-6}$
Two-Photon Absorption (TPA)	$\sim 10^{-13}$

Table 2.1: Comparison of the different up-conversion mechanisms regarding their efficiencies [14].

transfer up-conversion are usually much more probable than the direct-two-photon absorption by about 10 orders of magnitude. The different efficiencies are listed in table 2.1.

Up-Conversion Rate Equations

Pollnau [15] *et al.* analyzed up-conversion rate equations for m-level systems. For the calculations the following assumptions were made: (a) almost constant ground-state population density, (b) a continuous wave pumped system by ground-state absorption, (c) only ETU and ESA up-conversion mechanisms and (d) a decay rate of $A_i = \tau_i^{-1}$. The rate equations for a three energy level system ($m = 2$) are for ETU

$$dN_1/dt = \rho_p \sigma_0 N_0 - 2W_1 N_1^2 - A_1 N_1 \quad (2.2)$$

$$dN_2/dt = W_1 N_1^2 - A_2 N_2 \quad (2.3)$$

and for ESA

$$dN_1/dt = \rho_p \sigma_0 N_0 - \rho_p \sigma_1 N_1 - A_1 N_1 \quad (2.4)$$

$$dN_2/dt = \rho_p \sigma_1 N_1 - A_2 N_2, \quad (2.5)$$

where σ_j is the absorption cross section from state j and W_1 the up-conversion parameter. The pump parameter ρ_p can be described by: $\rho_p = \lambda_p/(hc\pi w_p^2)P_{\text{in}}$, with the pump wavelength λ_p, the incident power P_{in}, Planck's constant h, the speed of light in vacuum c, and the pump radius w_p. With the assumption that the glasses used have low maximum phonon frequencies - decay to the next lowest levels are negligible and luminescence directly to the ground state is predominant - in this case the equations can be solved. Three limiting situations can be distinguished. The power dependence of the population density for an m-energy level system is given in table 2.2. For systems with a small up-conversion rate the power dependence is given by $N_m \sim P^m$, whereas it is limited to $N_m \sim P_{\text{in}}^1$ for systems with the up-conversion being the predominant process. For systems in which both processes are present the exponent of the power dependency has to be between these two limits, one and m.

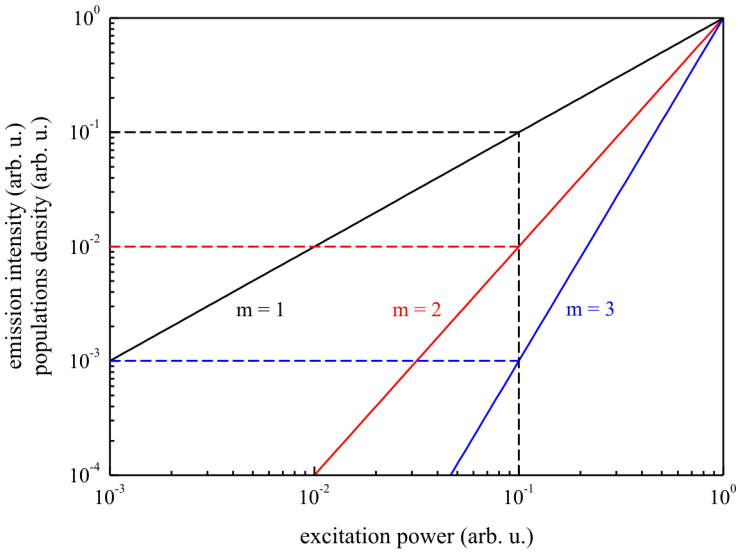

Figure 2.4: Schematically shown power dependency of different levels.

In figure 2.4 the power dependency is shown schematically for different systems. The black curve has a slope of $m = 1$ and displays the limit of a dominant up-conversion decay. The red line is the other limit for the 2 photon up-conversion, representing the system with a nearly negligible up-conversion process compared to the PL. When we now look at three photon up-conversion, the limits expand to a slope of three. In this case the excited states relax mainly due to normal PL. Therefore, systems with a low slope in the double logarithmic plot or low exponents for the power dependency, respectively, are preferable. These systems show an enhancement in the emission intensity or population density, respectively, for the same excitation power when compared to systems which are PL dominated.

From the short circuit current I_{sc} of a solar cell we can also calculate the external quantum efficiency (EQE) of the up-converting-layer on a solar cell system. The EQE is given by the ratio between generated electron hole pairs

influence of up-conversion	up-conversion mechanism	power dependence	from level
(1) low	(a) ETU & (b) ESA	$N_i \sim P_{in}^{i}$	$i = 1 \dots m$
(2) high	(a) ETU	$N_i \sim P_{in}^{1/2}$	$i = 1 \dots m-1$
		$N_i \sim P_{in}^{1}$	$i = m$
	(b) ESA	$N_i \sim P_{in}^{i}$	$i = 1 \dots m$
		$N_i \sim P_{in}^{1}$	$i = m$

Table 2.2: Power dependence of the population of up-conversion levels.

$I_{sc}(\lambda)/e$ and incoming photons $P_{in}(\lambda)/h\nu$ [16]:

$$\text{EQE} = \frac{I_{sc}(\lambda)}{e}\frac{h\nu}{P_{in}(\lambda)} \tag{2.6}$$

where $I_{sc}(\lambda)$ is the short circuit current of the solar cell and $P_{in}(\lambda)$ the power of the incident light. λ and ν are the wavelength and frequency of the incident light, respectively. h is Planck's constant, c the speed of light in vacuum, and e the charge of an electron. Since $I_{sc}(\lambda) \propto P_{in}^{m}$ we obtain from equation 2.6:

$$\text{EQE} \propto \frac{P_{in}^{m}}{P_{in}} = P_{in}^{m-1}. \tag{2.7}$$

2.2 Glasses and Glass Ceramics

2.2.1 Phonons

A phonon is a quantized vibration mode occurring in a crystal lattice. Another description for a phonon is quantized thermal energy. Phonons play an important role for excited states. An ion excited to an energetically higher state has two options to relax into a lower level (e.g. ground state). First, it can emit a photon, carrying the energy difference between the two states, to get into the lower level. The second possibility to get to a lower level is a non-radiative process. Hereby, the energy difference between the excited states is transferred to one or more phonons. This relaxation is normally described as a leakage process.

To reach luminescence from an ion with high radiative emission efficiencies the non-radiative relaxation caused by multiphonon relaxation (MPR) has to be minimized. For this case large energy-gaps (in the region of some 1000 cm^{-1} for some rare earth elements) between the excited states and the next lowest levels are useful. Additionally minimizing the highest-phonon-energy of the hosts $\hbar\omega_{max}$ and ν_{max}, respectively, leads to an increase of the number of required phonons for the MPR to bridge this energy gab. Figure 2.5 shows a trivalent neodymium energy level diagram as an example. For four different glasses - borate, silicate, germanate, and zirconium-fluoride - the number of phonons with maximum phonon frequency which is required to reach the next lowest level is shown. The more phonons are needed to bridge the gap, the higher the efficiency of the radiative depopulation; this expands the detectable lifetime of the exited state. The lifetime τ_a of an excited state, a, is represented by formula 2.8, where T_{ab} and W_{ab} are the the radiative and non-radiative transition probabilities from level a to level b, and the summation is over all ground states b.

$$\frac{1}{\tau_a} = \sum_b (T_{ab} + W_{ab}) \tag{2.8}$$

Host glass	Notation	$\hbar\omega_{max}$ (cm^{-1})	C (s^{-1})	α (10^{-3}cm)
Borate	B_2O_3	1400	$2.9 \cdot 10^{12}$	3.8
Phosphate	P_2O_5	1200	$5.4 \cdot 10^{12}$	4.7
Silicate	SiO_2	1100	$1.4 \cdot 10^{12}$	4.7
Germanate	GeO_2	900	$3.4 \cdot 10^{10}$	4.9
Tellurite	TeO_2	700	$6.3 \cdot 10^{10}$	4.7
ZrF_4-based	ZrF_4	500	$1.9 \cdot 10^{10}$	5.8
$ZnCl_2$-based	$ZnCl_2$	300	$5.0 \cdot 10^{7}$	4.1

Table 2.3: Host-dependent parameters of multiphonon relaxation in glasses [17, 19].

Non-radiative processes include, in addition to the MPR, relaxation by direct ion-ion energy transfer. For low dopant concentrations the energy transfer is not the predominant mechanism so that it is negligible and the MPR rate can reasonably be described with an exponential law. Equation (2.9) is often called the *energy-gap law* [17].

$$W_{ab} = C \cdot \exp(-\alpha \Delta E) \tag{2.9}$$

The parameters C and α are the positive host-dependent constants and depend on the host crystal and strength of ion-lattice coupling. With rare exceptions these constants are independent of the specific RE ion or electronic states [18]. Some examples for these parameters for different glasses are given in table 2.3. In figure 2.6 the MPR rate for different glasses and rare earth elements are given with respect to the energy gap. Figure 2.7 shows the reflexion spectra of different glasses. The measured maximum phonon frequency is in good agreement with the literature [19, 21].

2.2.2 ZBLAN glasses

In 1974 Poulain *et al.* [22] discovered the heavy metal fluoride glasses (HMFG) based on zirconium (Zr) and/or hafnium (Hf) fluoride. The most important feature is high transparency over a large spectral range from the near UV ($\sim$ 0.2 μm) to the mid-IR ($\sim$ 7.0 μm) [23]. In figure 2.8 three glasses were compared in respect to their transparency in the IR spectral range. Fluorozirconate (FZ), fluorochlorozirconate (FCZ), and fluorobromozirconate (FBZ) glasses and glass ceramics are based on the well-known ZBLAN composition [21] and belong to the HMFG. These glasses and glass ceramics are characterized by a low maximum phonon energy (<580 $cm^{-}1$). This leads to increased fluorescence efficiencies from rare-earth ions due to minimized non-radiative decay processes. Energy levels that are separated from the next lowest levels by more than a few times the maximum phonon energies decay mainly by radiation. These glasses also possess a low refractive index, low material

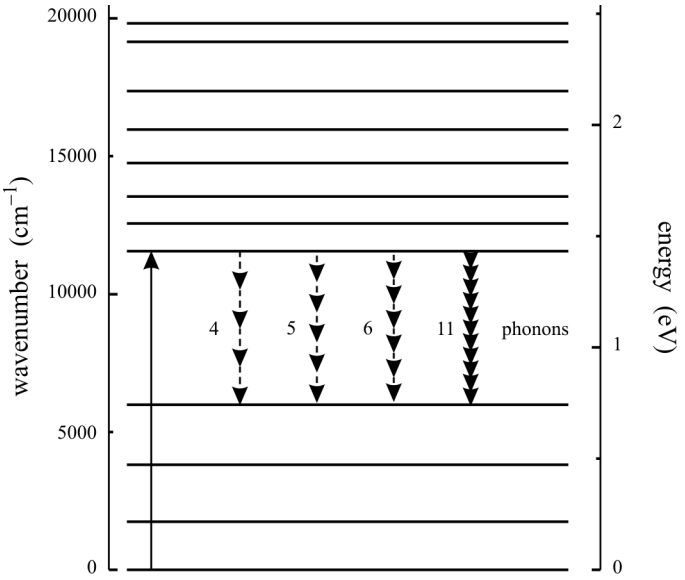

Figure 2.5: Advantage of low phonon glasses using the example of trivalent neodymium. The number of phonons with maximum phonon frequency which are required to depopulate the $^4F_{3/2}$ to the next lower energy level is shown for different glasses. From left to right: borate (4), silicate (5), germanate (6), zirconiumfluoride (11) based glasses.

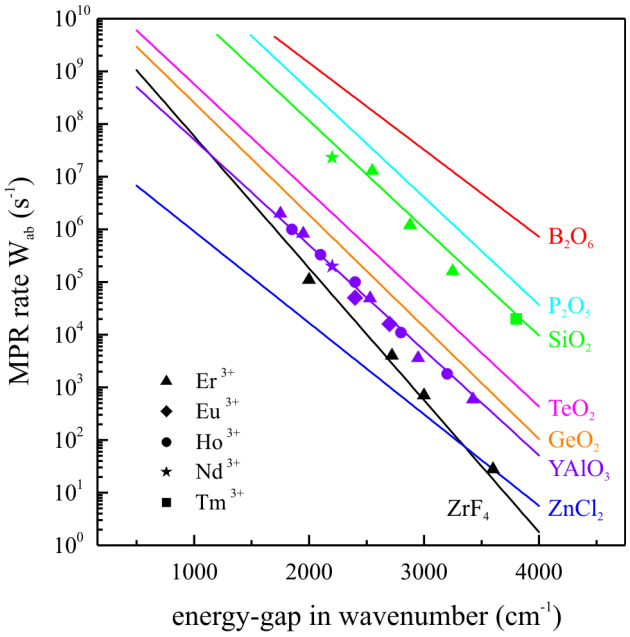

Figure 2.6: Multiphonon relaxation rates for rare-earth ions in different host materials plotted as a function of the energy gap to the next lower level [17]. For demonstration some data points [18–20] of $YAlO_2$ (yttrium orthoaluminate), SiO_2-, and ZrF_4-based glasses are shown.

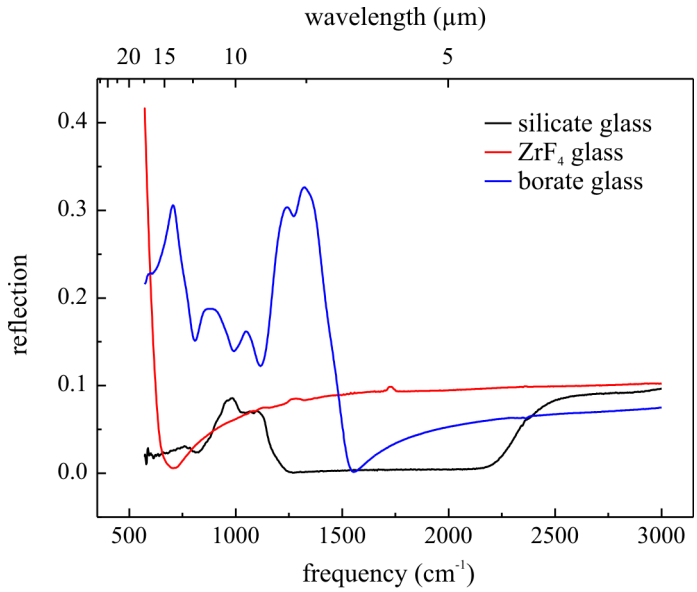

Figure 2.7: Reflection spectra of silicate (black curve), ZrF4 (red curve), and borate (blue curve) glasses. The maximum phonon frequency of the samples can be determined from these measurements. A FTIR IFS66 spectrometer was used.

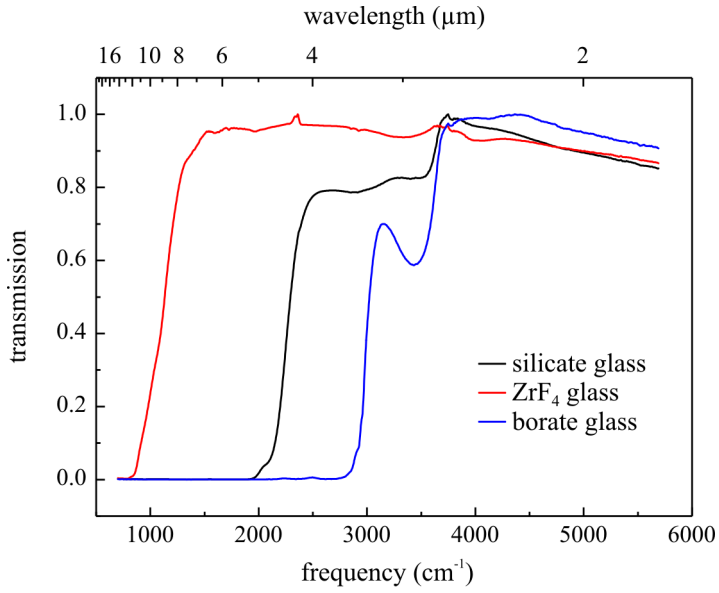

Figure 2.8: Transparency of a normal SiO_2 glass (black curve), borate glass (blue) and an as-made FCZ glass ceramic (red curve). All samples have a thickness of 1 mm. The measurements were performed with a Bruker Hyperion spectrometer.

Material	FZ		FCZ		FBZ	
ZrF_4	53.0	-x	53.0	-x	53.0	-x
BaF_2	20.0		10.0		10.0	
$BaCl_2$	-		10.0		-	
$BaBr_2$	-		-		10.0	
LaF_3	3.5		3.5		3.5	
AlF3	3.0		3.0		3.0	
NaF	20.0		-		-	
$NaCl_2$	-		20.0	(-x)	-	
$NaBr_2$	-		-		20.0	(-x)
InF	0.5		0.5		0.5	
Rare Earth	-	+x	-	+x	-	+x
KCl	-		-	(+x)	-	(+x)

Table 2.4: Composition of ZBLAN glasses. The left column shows the basic version of doped glasses. The compositions for FCZ and FBZ glass ceramics are listed in the middle and right column, respectively. For some dopings (e.g. NdF_3) a charge compensation is required - this is realized by the (x)-components. The compositions are in mol%.

dispersion, low linear scattering loss, and good chemical durability [24–26]. All these attributes are useful and/or essential for a fibre material. Thus, rare-earth doped HMFG are interesting to the telecommunication and data transfer industries. Also for digital radiography, FZ glasses have been doped with europium and chlorine ions resulting in very efficient glass-ceramic radiation detectors [27, 28] where the RE ion, europium, is incorporated into the glass as well as in the barium chloride nanocrystals formed in the glass upon annealing. FZ-based glass ceramics offer a broad range of applications; the functionality can be modified not only by appropriate thermal processing but also by appropriate rare-earth doping.

The glasses are prepared as followed: The base composition of chemicals were additionally doped with RE ions. In table 2.4 the chemicals used and their compositions in mol-% are given for FZ, FCZ, and FBZ glasses. The ingredients should be high purity chemicals. In order to minimize impurities the preparation process has to be done in an inert atmosphere. The constituent chemicals were pulverized and mixed in a mortar. They were melted in a glassy carbon crucible at 745 °C for 30 minutes, cooled down to 650 °C and then poured into a brass mold that was at a temperature of 200 °C, i.e. below the glass transition temperature of 262 °C for a FZ-based glass [21], before being slowly cooled to room temperature.

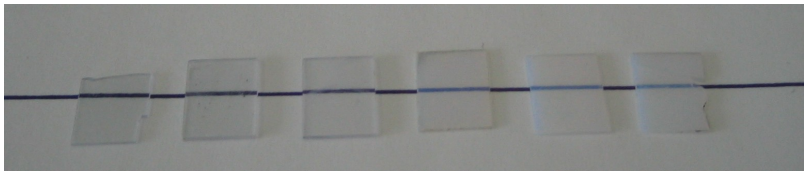

Figure 2.9: FCZ glass ceramics. All samples were annealed for 20 minutes. From left to right: as-made, 260, 270, 280, 285, and 290 °C.

2.2.3 Thermal Processing and Nano-Particles

In section 2.2.1 it was described that phonons and their maximum frequency affect the observable lifetime of the excited states. However, the phonon frequency is not only given by the matrix but also by the size of the crystallites; in nanocrystals, only low-phonon frequencies are found [29].

Through subsequent annealing in the vicinity of the glass transition temperature nanoparticles are formed in the glass. Therefore the FZ glasses have to be doped beforehand with chlorine for FCZ or with bromide for FBZ glasses. The glass transition temperature is at about 260 °C and depends on the composition and doping of the glasses. The glass transition temperature can be determined with differential scanning calorimetry (DSC). Figure 2.9 shows a series of FCZ samples. The annealing time for all samples was 20 minutes, and the temperature was varied from 260 to 290 °C. With higher annealing temperature the nanocrystals in the glass ceramics became larger. When the particle size reaches the region of a few hundreds nanometers, visible scattering effects can be observed. To determine the size of the particles XRD spectra or TEM images can be used. The subsequent annealing steps after glass processing (to form the nanoparticles) as well as the glass production were performed in an inert nitrogen atmosphere.

2.3 Rare Earth Ions

Lanthanides and actinides are generally known as rare earth (RE) elements. The potential application of these elements are manifold. The REs, in common with the actinides, have the most complicated fluorescence spectra of any elements [30] (see figure 2.10). This is caused by an incompletely filled 4f shell. At first, the origin of the sharp peaks seen in these spectra puzzled the scientific community. Bethe, Kramers and Bequerel suggested that the lines could be attributed to transitions within the 4f configuration. In 1937 van Vleck [41] showed that the parity forbidden 4f $\rightarrow$ 4f transitions become partly allowed as electric dipole transitions by the admixture of configurations of opposite parity. Many low lying energy levels are produced due to the transition within the 4f shell. Additionally due to an effect called lanthanide contraction the

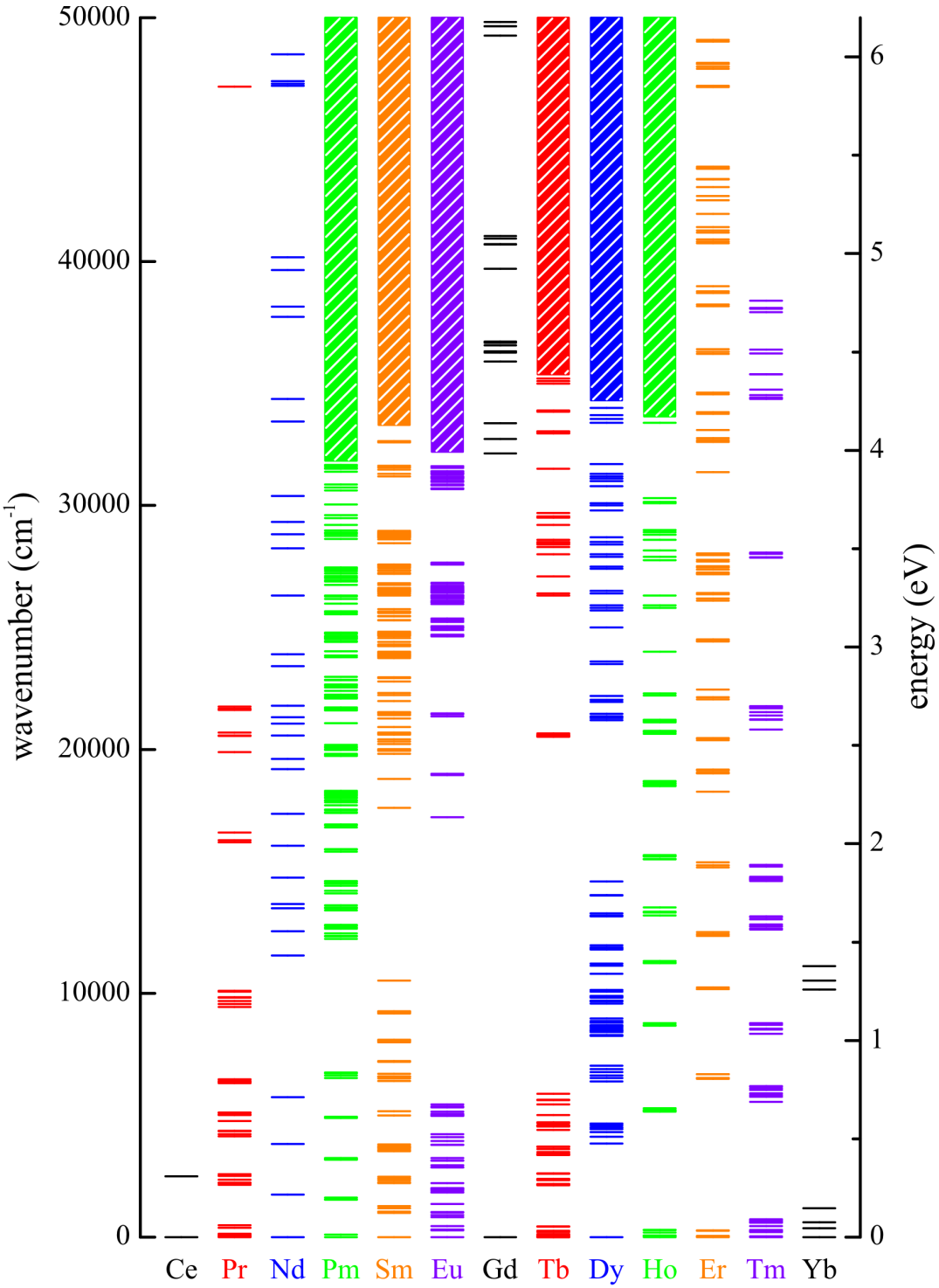

Figure 2.10: Energy levels of the $4f^n$ configurations of the trivalent rare earth ions [30–40]. Closely spaced levels are depicted as bands.

4f shell is surrounded by the completely filled $5s^2$ and $5p^6$ orbitals, shielding the 4f shell nearly completely from its surrounding. Atomic lattice vibrations (phonons) or other influences from the host are minimized because of this energetic shielding. This is a reason for the similar chemical and physical attributes of the RE elements. The position of the energy levels and the transitions itselfs depend only barely on the host material the RE element is incorporated in. Upon the fact of forbidden 4f $\rightarrow$ 4f transitions and the energetic shielding, minimizing the of interactions between the RE ion and the host material, the excited states have relatively long lifetimes; up to milliseconds. A selection of trivalent RE element energy levels is given in figure 2.10, it is the so called 'Dieke diagram'.

Different applications like lasers use the up-conversion process. The following RE elements are known for these applications: Tm, Er, Ho, Nd, and Pr; all in their trivalent state. Figure 2.11 shows the energy level diagram of these elements. Up-conversion routes are not shown for clarity. A grey background was added to the excited states of the energy level diagrams. The well-known trivalent RE ions used for down-conversion and/or quantum cutting are shown with their energy level diagram in figure 2.12. These are Tb, Eu, Ho, Sm, and Gd. A grey background for the excited states was added, too.

2.4 Analyzing Methods

2.4.1 Photoluminescence

For fluorescence and fluorescence excitation spectra a single-beam spectrometer in which a 0.22 m (Spex 1681) and a 0.55 m (Horiba Jobin Yvon iHR550) monochromator were available for excitation and emission. For excitation and absorption measurements two lamps, a halogen (300 - 800 nm) and a xenon lamp (250 - 500 nm), were used. For the up-conversion process more powerful excitations sources were needed. Here continuous wave (CW) infrared laser diodes operating at 796 nm (Toptica Photonics #LD-0795-0150-2), at $\sim$ 811 nm (OEC GmbH 1010-C), and at 1542 nm (Anritsu GB5A016) were used. The fluorescence was detected in the visible spectral range with a cooled photomultiplier (Hamamatsu R943-02) and in the infrared spectral range with a cooled germanium detector (Edinburgh Instruments). Silicon, InGaAs, and PbS photo diodes were available for measurements. All detectors were used in lock-in-technique (SRS-SR830). The spectra have not been corrected for spectral sensitivity of the experimental setup.

For the fluorescence lifetime measurements, the excitation sources were modulated by a square wave signal from a generator (Rhode & Schwarz AFS) or by a mechanical chopper, depending on the expected lifetimes. By switching

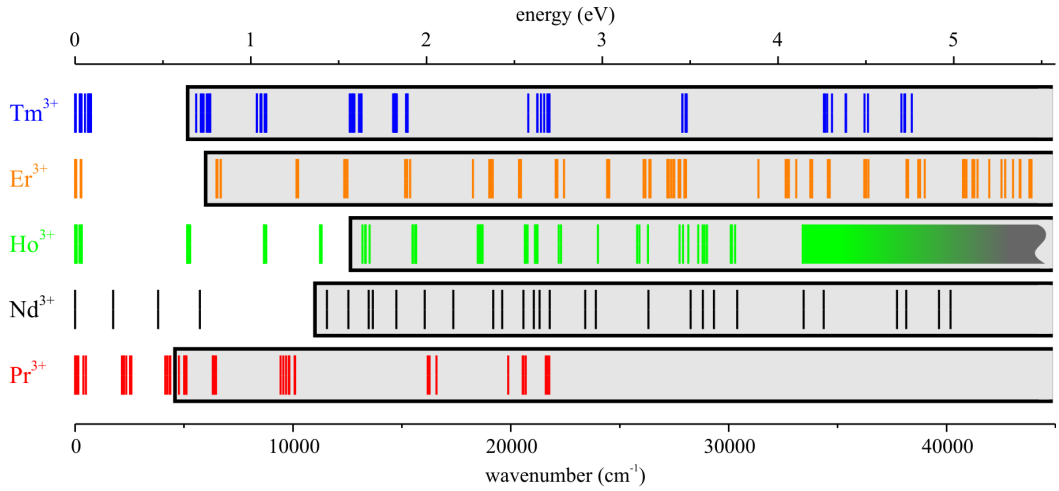

Figure 2.11: Trivalent RE elements known for up-conversion processes. The excited states have a grey background. Closely spaced levels are depicted as bands.

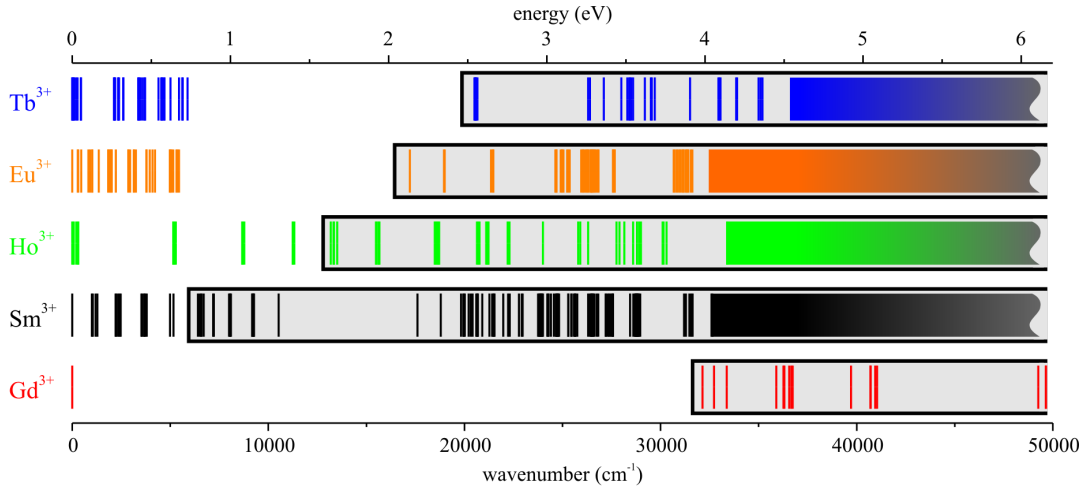

Figure 2.12: Rare earth elements in its trivalent state known for down-conversion processes. The excited states have a grey background. Closely spaced levels are depicted as bands.

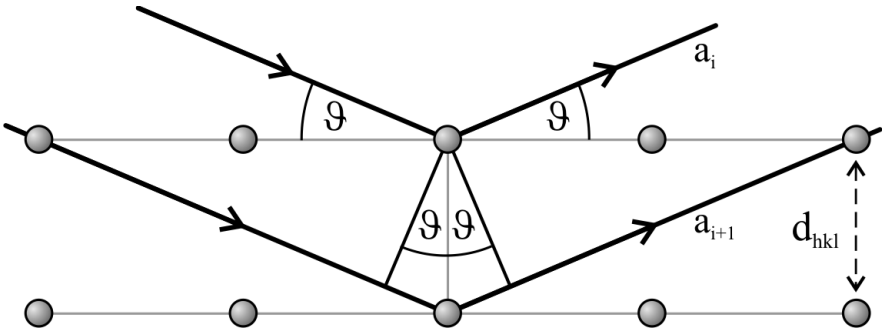

Figure 2.13: Bragg scattering in a crystal. The x-rays (a_i and a_{i+1}) are scattered and reflected by the periodic structure. The scattered x-ray beams build a "reflected" interference pattern.

the excitation source on and off only the fluorescence decay was observed. The fluorescence signal was detected with the photomultiplier amplified and recorded with a digital oscilloscope (Tektronix TDS 1012B).

For power dependence measurements of the fluorescence and up-converted fluorescence intensities versus the excitation power a power meter with a silicon optical sensor (Thorlabs S121B) was used. The different excitation powers were achieved by adjusting the laser current or by setting neutral density filters into the optical axis.

2.4.2 X-Ray Diffraction

X-ray diffraction (XRD) is a method to characterize the structure of crystals. It can also be used to analyze the size of nano-crystals or particles. Interference of incident x-rays with the periodic structure of crystals is measured. The condition for constructive interference is given by the "*Bragg's law*":

$$2 \cdot d_{hkl} \cdot \sin \vartheta_B \quad = \quad n \cdot \lambda, \tag{2.10}$$

with d_{hkl} the lattice distance between the crystal layers, ϑ_B the angle of incidence, n the order of the diffraction, and λ the wavelength of the incident wave. The index *hkl* is defined by the Miller indices and describes a series of crystallographic planes.

The nano-crystallites in the FCZ glass ceramics have no preferred orientation. These give essentially powder-diffraction conditions. For a powder, x-ray diffraction occurs for orientation that fulfills *Bragg's law*. This produces the *Debye Scherrer rings* in a plane behind the sample, which are symmetric about the origin, $\vartheta = 0$. By detecting the x-ray intensity on a line of this plane, an angular dependent XRD spectrum can be observed.

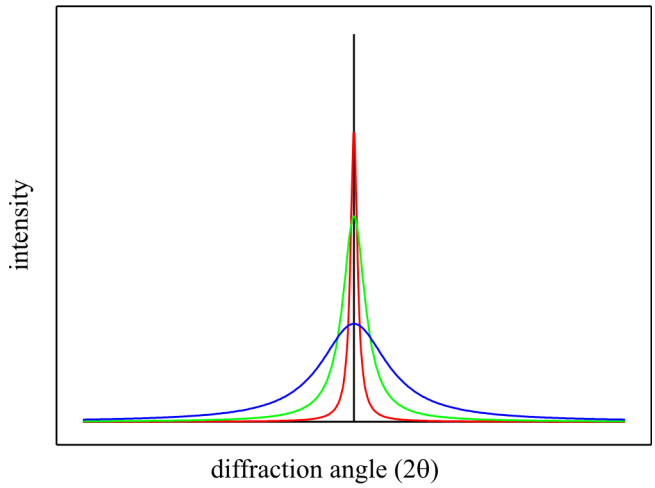

Figure 2.14: The broadening of XRD reflection peaks: the ideal XRD peak (black), with broadening due instrumental resolution (red). The green line is additionally broaden due to instrumental and crystal size effects. The blue line describes the reflection with all named effects before combined with strain and stress.

Line Width and Crystal Size Determination

A Bragg reflection from a monochromatic x-ray tube diffracted for an infinite, perfect crystal is a δ-function, but a crystal with imperfections produces a Gaussian like reflection peak. These imperfections are based on crystals that are not free from strain or stress. Also faulting and lattice defects or non-infinite crystals e.g. small crystal sizes produce a broadening effect. Additional to the broadening caused by the parameters of the diffracting crystals there is an external broadening, the so called instrumental broadening. The instrumental broadening depends on resolution and the natural linewidth. Wavelength dispersion of the incident and reflected beam also affects the linewidth. Slit width, sample size or incorrect x-ray focusing causes a broadening of the detected diffraction peak. Because of these effects the ideal delta peak of the measurement signal is widened as shown in figure 2.14.

The broadening effect based on the crystal size can be used to determine the size of nano-crystals formed in glasses i.e. glass ceramics. The first investigation of particle size broadening was due to Scherrer [42]. To analyze the size of the crystals the instrumental broadening has to be subtracted from the x-ray diffraction pattern. To determine the instrumental broadening a reflection peak from a sample in which the particle size is nearly infinite has to be taken, consequently obtaining a signal with only the instrumental broadening. With this result the instrumental broadening can be corrected for all measurements taken under the same conditions.

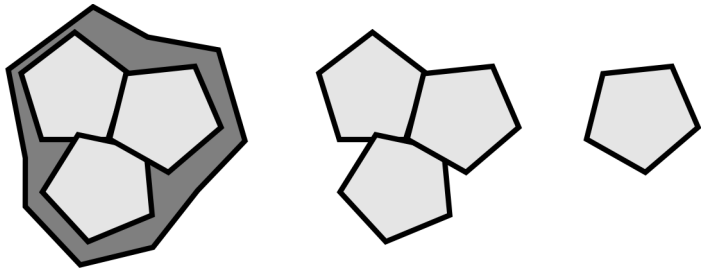

Figure 2.15: In (a) the grain or particle size is schematic shown, (b) and (c) show the crystal and crystallite size, respectively.

With the known instrumental broadening and the assumption of strain- and stress-free crystals a determination of crystal sizes is possible. Therefore, we estimate the particle sizes by using the Scherrer formula [42]

$$d = \frac{K \cdot \lambda}{(\Delta - 0.085^\circ) \cdot \cos(\vartheta)} \tag{2.11}$$

with d the particle size, K the Scherrer constant, λ the wavelength of the incident x-ray beam, 2ϑ the peak position of the reflection, and Δ the full width at half maximum of the reflection (FWHM). The Scherrer constant depends on the crystal structure and on the reflection indices i.e. the reflection crystallographic plane [43]. However the constant varies only slightly for the different structures and planes between 0.9 and 1.0. For first estimations of crystal sizes the Scherrer constant K can be set to one. A complete derivation of the Scherrer formula can be found in [44].

Unfortunately, there is enormous confusion in literature concerning the definition of size of particles, crystals, and crystallites. Going from large to small, it starts with the particle or grain. It consists of one or more crystals. All crystals in this particle may be separated by large angle differences as well as amorphous or crystalline intersections (see figure 2.15(a)). It is worth mentioning that it is not really possible to determine the particle size by X-ray diffraction measurements; the crystals consists of one or more crystallites with size equal to or smaller than the size of a particle (fig. 2.15(b)). As well as the particle the crystal size itself cannot be detected or measured. The size of a crystallite is typically less than or equal to the crystal size (fig. 2.15(c)). The size of the crystals can be determined - in the absence of crystal domains - by analyzing x-ray diffraction patterns.

3 Down-Conversion based on Sm

By a process, in which high energy (UV) photons were effectively converted or cut into one or more low energy photons with an energy higher than the band gap energy, the efficiency of a solar cell can be increased significantly. In the quantum cutting process one high energy photon is cut into two or more photons in the visible or near-infrared that can be absorbed by a solar cell. Trupke *et al.* [6] calculated the theoretical limit of a single junction solar cell which uses additional quantum cutting processes to an over-all external quantum efficiency of 39.63 %. The down-conversion process requires an optically active center. Rare earth ions are known for a discrete energy levels that can be used for the conversion process. When embedded in a low phonon glass matrix the loss mechanisms can be reduced. A good choice due to their low phonon frequencies of around 500 cm^{-1} are glasses based on the well known ZBLAN composition [21]. From prior investigations it is known that glass ceramics with embedded nanocrystals containing rare earths show an enhanced fluorescence efficiency.

3.1 Simulations

Trupke *et al.* [5] made several theoretical assumptions in their calculations and vary the band gap to reach the the theoretical maximum external quantum efficiency. To determine more realistic limits, further calculations were performed; the details appear in appendix B. Figure 3.1 shows the results of the calculations as a contour plot as a function of the absorption bang edge of the down-converting layer and the internal quantum efficiency (IQE), given in nm and %, respectively. The absorption of the down-conversion layer was set to one for this calculation. All points were normalized to the initial system without an down-converting layer. The maximum enhancement, for a absorption band edge at 818 nm and 100 % IQE, is at 1.198, which means an enhancement of 19.8 % in comparison to the system without a down-converter. In fact of the down-conversion layer in front of the solar cell, the ratio can be less than 1 in fact of low internal quantum efficiencies. These areas are colored in blue to green; see the color scale in the figure. A dashed line at 500 nm marks the "position" where the next calculation (see figure 3.2 take place. With a fixed absorption edge at 500 nm, the internal quantum efficiency and absorption (both given in %) were varied for the calculations. Figure 3.2 shows normalized

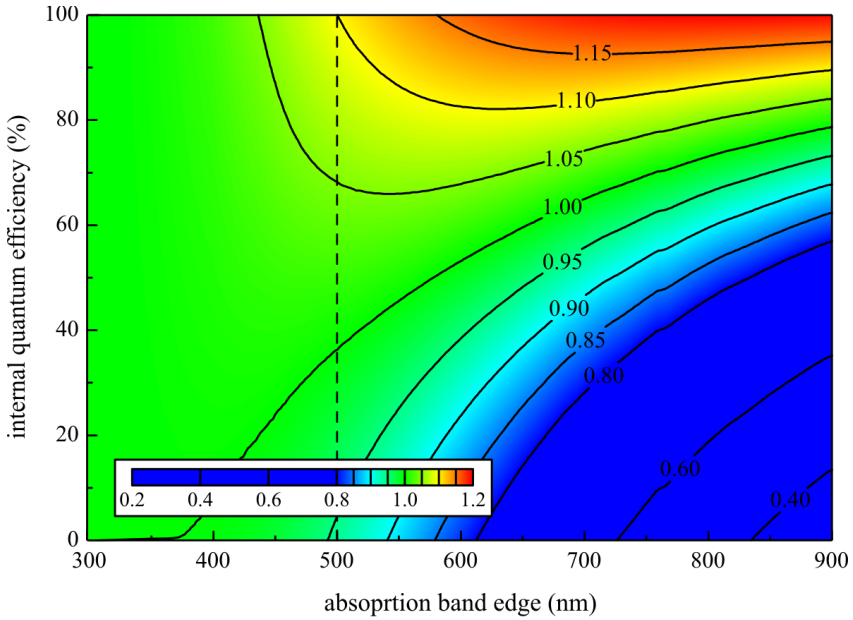

Figure 3.1: Calculated ratio between solar cell with and without a down-converting layer in dependency of the absorption edge of the layer and the internal quantum efficiency. The absorption is set to 100 %. A maximum for for 818 nm as the absorption band edge and 100 % internal quantum efficiency of 1.198 was calculated; 0.282 for the minimum. The color stands for the calculated ratio (see color scale in the lower left corner).

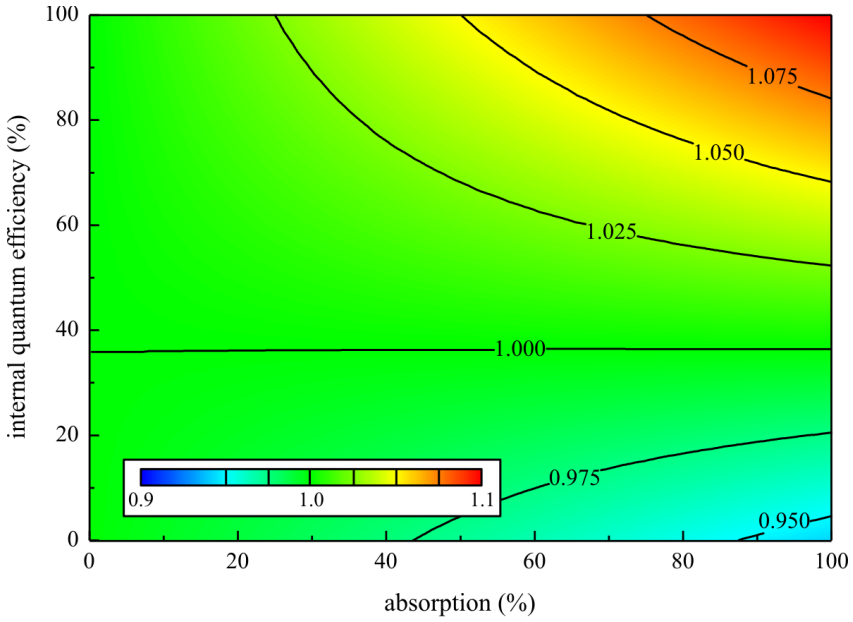

Figure 3.2: Calculated ratio between solar cell with and without a down-converting layer in dependency of the absorption of the layer and the internal quantum efficiency. The absorption band edge is set to 500 nm. A maximum for 100 % absorption and internal quantum efficiency of 1.100 was calculated; 0.943 for the minimum. The color stands for the calculated ratio (see color scale in the lower left corner).

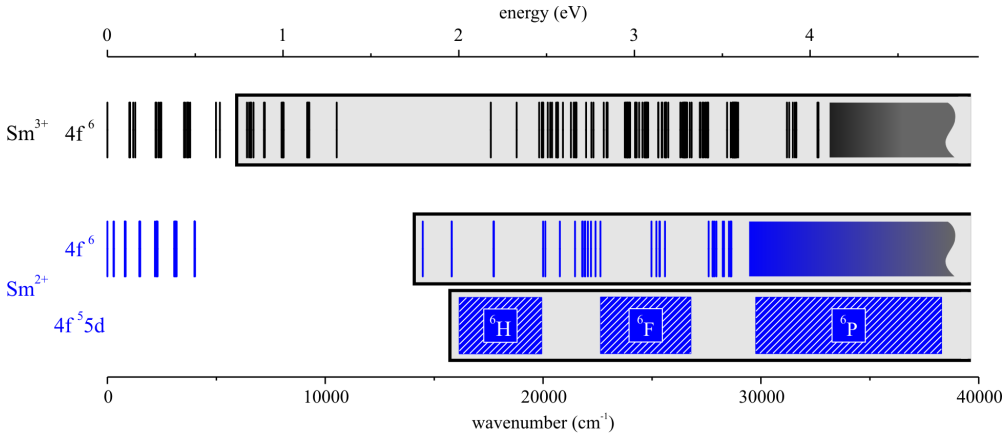

Figure 3.3: Energy level diagram of trivalent (black) and divalent (blue) samarium. The Sm^{2+} energy levels are a combination of the $4f^6$ and the $4f^55d$ states [45, 46]. The $4f^55d$ states of Sm^{3+} are in the far VUV (with energies of about 70,000 cm^{-1}) [30]. All excited states are highlighted with a grey background. Closely spaced levels are depicted as bands.

results for the solar cell without a down-converting layer. A minimum and maximum of 0.943 and 1.100, respectively, were calculated. In both cases the absorption of the down-converting layer is 100 %, whereas the internal quantum efficiency is zero for the minimum and 100 % for the maximum value. For all absorption values the plot shows a horizontal line with a value of one at an IQE of 36.36 %, i.e. that a silicon solar cell with a down-converter of 36.36% IQE on top has the same overall efficiency as the silicon solar cell itself.

3.2 Dopant: Samarium

3.2.1 Motivation

For down-conversion applications an optically active center is needed. Good RE candidates for efficient down-conversion, both quantum cutting and normal PL, are given in chapter 2 in figure 2.12. They all have many absorption lines and absorption bands in the UV and blue spectral range. Some elements even have energy levels that absorb in the lower energetic spectral range. Intense emission lines and bands in the green, red or near-infrared spectral range are required for a down-converter. Samarium is listed in this figure; in its trivalent state. By comparing the trivalent energy level of Sm with the divalent one (see figure 3.3) it can be seen that Sm^{2+} offers some advantages. The normal $4f^6$ energy levels are superimposed by the broad energy levels of the $4f^55d$. These energy levels mainly increase the absorption in the green, blue and UV spectral range.

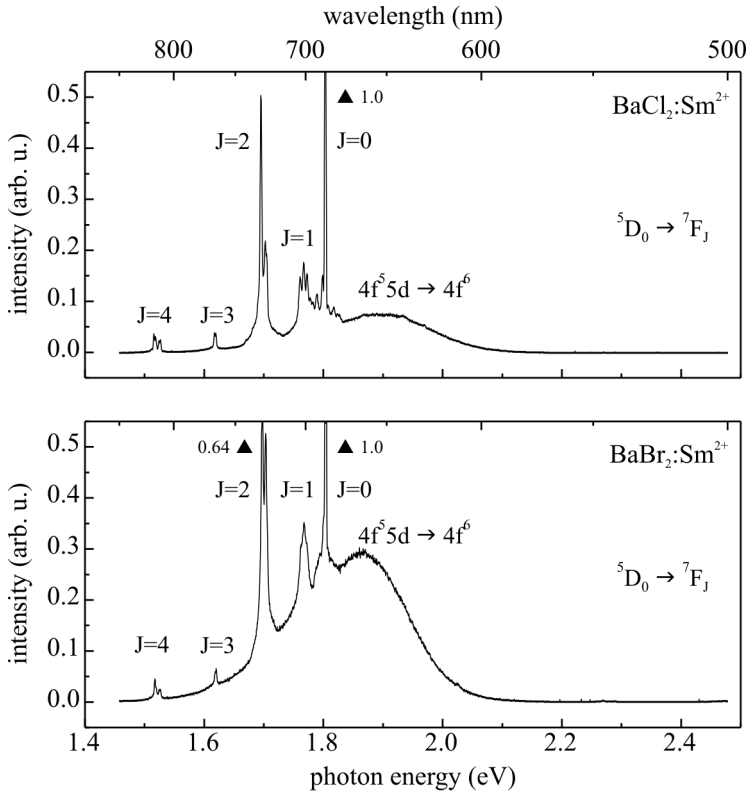

Figure 3.4: Normalized fluorescence spectra of 0.1 mol% Sm^{2+}-doped $BaCl_2$ and $BaBr_2$ single crystals. The emission was recorded under continuous laser excitation with the 476 nm line of an Ar^+ laser. The lines were attributed to $^5D_0 \rightarrow {}^7F_J$ and $4f^55d \rightarrow 4f^6$ transitions [31]. The measurements were carried out at RT.

3.2.2 Barium Chloride and Barium Bromide

Single crystals of $BaCl_2$ and $BaBr_2$ were grown in the crystal growth laboratory at the University of Paderborn using the Bridgman method. Before the crystal growth process the $BaCl_2$ and $BaBr_2$ powders were dried in a vacuum with subsequent melting in a $SiCl_4$ and $SiBr_4$ atmosphere, respectively to reduce possible oxygen contamination of the starting materials. The powders were melted in a quartz ampoule under the $SiCl_4$ and $SiBr_4$ atmosphere. 1000 molar ppm of $SmCl_2$ and $SmBr_2$, respectively were added as dopant to the powder. The single crystals were slowly cooled through the cubic-orthorhombic phase transition near 920 °C for $BaCl_2$ [47] and 800 °C for $BaBr_2$ [48], respectively.

Fluorescence and X-Ray Excited Luminescence

Fig. 3.4 shows the fluorescence spectra of $BaCl_2$ (top) and $BaBr_2$ (bottom) with 0.1 mol% Sm^{2+} doped single crystals in the visible spectral range between 500 and 830 nm. The samples were excited with an Ar^+ laser at 487 nm. The observed intense sharp emissions at 687, 702, and 728 nm combined with the

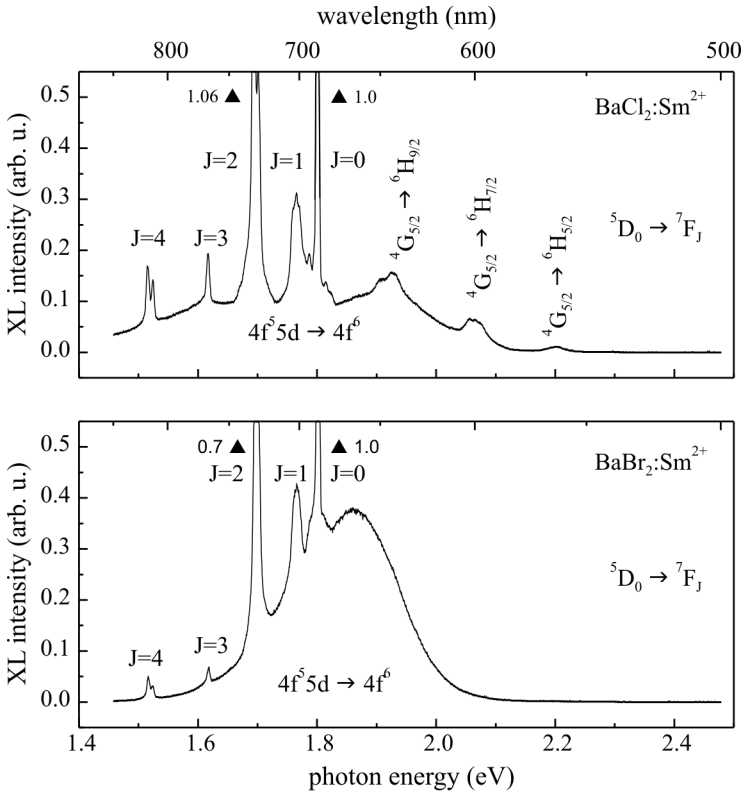

Figure 3.5: X-ray excited fluorescence spectra of 0.1 mol% Sm^{2+}-doped $BaCl_2$ (top) and $BaBr_2$ (bottom) single crystals. Both spectra were normalized to the emission at 728 and 687 nm, respectively. The emission lines were attributed to $^5D_0 \rightarrow {}^7F_J$ with $J = \{0, 1, 2, 3, 4\}$ and $4f^5 5d \rightarrow 4f^6$ transitions of Sm^{2+} [31]. The Sm-doped $BaCl_2$ crystals show additional Sm^{3+} emissions [49]. The measurements were carried out at RT.

broad band emission ranging from around 600 up to 800 nm are typical for Sm^{2+}. The sharp emissions can be assigned to $^5D_0 \rightarrow {}^7F_J$ transitions with $J = \{0, 1, 2, 3, 4\}$. The broad emission band is not from a 4f $\rightarrow$ 4f transition but it can be assigned to a $4f^5 5d \rightarrow 4f^6$ transition. All emissions associated with the 4f $\rightarrow$ 4f transitions of Sm^{2+} are noticeably split by the crystal field [46]. Both spectra were normalized to their most intense emission at 687 nm.

For a closer look all emissions of the doped crystals the samples were excited with x-rays. In figure 3.5 the normalized x-ray excited luminescence (XL) spectra of 0.1 mol% Sm^{2+} doped $BaCl_2$ and $BaBr_2$ are shown. Comparing the X-ray excited spectra with the normal fluorescence spectra shows no evident differences. The intense sharp emissions can be attributed to the $^5D_0 \rightarrow {}^7F_J$ transitions with $J = \{0, 1, 2, 3, 4\}$ as depicted in the figure. The broad band emission of Sm^{2+} can be seen in both XL spectra. Only one main exception can be observed comparing the XL with the normal fluorescence spectra. There were three emissions on the shoulder of the $4f^5 5d \rightarrow 4f^6$ emission for the Sm-doped

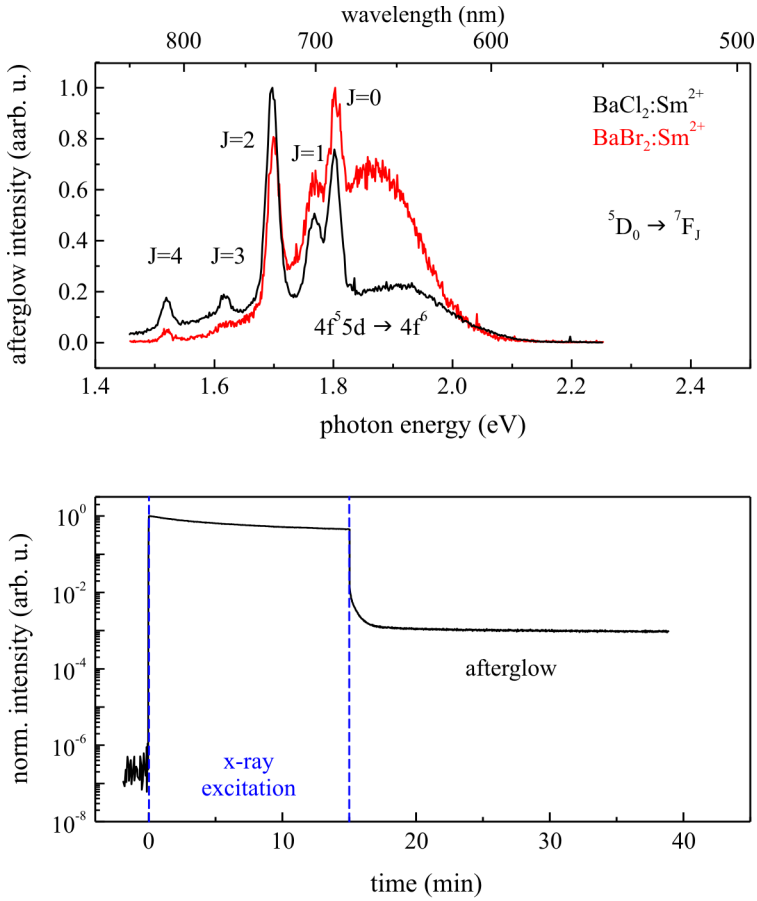

Figure 3.6: Afterglow spectra of 0.1 mol% Sm^{2+}-doped $BaCl_2$ (black curve) and $BaBr_2$ single crystals (red curve). Both spectra were normalized to the most intense emission at 687 and 730 nm. The lines can be attributed to $^5D_0 \rightarrow {}^7F_J$ and $4f^55d \rightarrow 4f^6$ transitions of Sm^{2+} [31]. The measurements were carried out at RT. The lower graph shows the intensity of the 687 nm emission ($BaCl_2$:Sm) during and after x-ray irradiation.

$BaCl_2$. These three emissions can be attributed to transitions of a trivalent Sm ion. The energetically highest emissions of the three at 560 nm results from a $^4G_{5/2} \rightarrow {}^6H_{5/2}$ transition. The other two transitions although arise from the same excited state but relax to different ground states; to the $^6H_{7/2}$ and $^6H_{9/2}$ for the 595 and the 640 nm, respectively. No further emissions can be observed - co-doping due to impurities can be excluded. The Sm^{3+} emissions are only in the XL spectra observable, which could be an evidence for a charge transformation upon x-ray irradiation.

The Sm-doped crystals show an afterglow after they were excited with x-rays. The afterglow spectra of $BaCl_2$ and $BaBr_2$ doped with divalent Sm are shown in figure 3.6 (a). In contrast to a XL spectrum an afterglow spectrum is recorded after and not during the x-ray excitation. The spectra show the typical Sm^{2+} emission. In the near infrared sharp emissions arising from the $^5D_0 \rightarrow {}^7F_J$ transitions with $J = \{0, 1, 2, 3, 4\}$ can be observed. The broad band

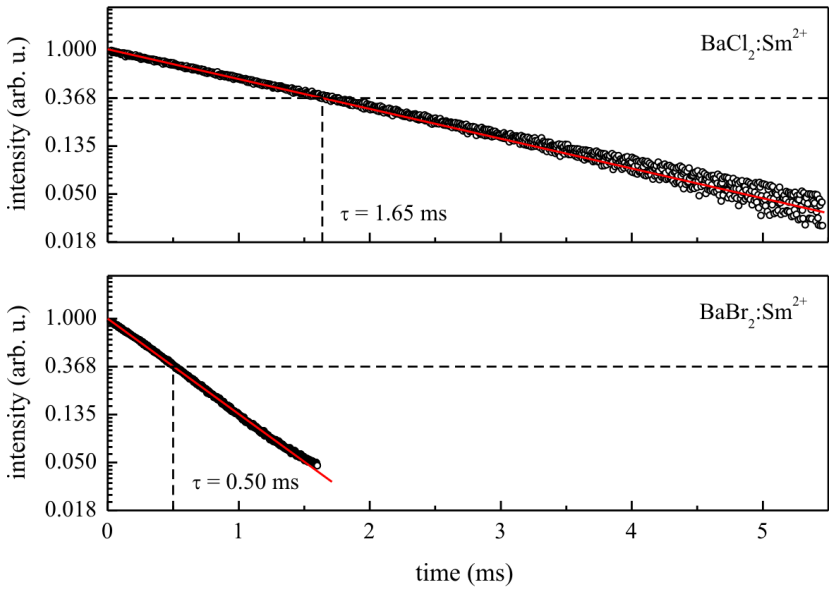

Figure 3.7: Decay of the Sm^{2+} fluorescence in $BaCl_2$ and $BaBr_2$. The Sm^{2+} doping concentration is 0.1 mol%. The emission was detected at 687 nm, which corresponds to the $^5D_0 \rightarrow {}^7F_0$ transition of Sm^{2+}. The fluorescence lifetimes of the $^5D_0 \rightarrow {}^7F_J$ and the $4f^55d \rightarrow 4f^6$ transitions are identical within experimental error. An Ar^+ laser was used for the excitation at 476 nm.

emission can be attributed to the $4f^55d \rightarrow 4f^6$ transition. The afterglow spectra were recorded after a radiation time of 15 minutes. The spectra were recorded 30 minutes after the excitation. The afterglow decay time is relatively slow - measurements performed 45 minutes after the sample was x-radiated compared to measurements after 60 minutes show a loss of only 3 to 5 % in its intensity. Therefore further investigations were performed on this effect. The measured intensity of the 687 nm emission in dependency of the time during and after the x-ray excitation is plotted in figure 3.6 (b). The start and end of the x-ray excitation can be seen in figure 3.6, marked as dashed blue lines. The afterglow signal is 5 to 6 orders of magnitude stronger than the measured dark signal and has a relatively long decay time.

Lifetime Measurements

Lifetime measurements of the $^5D_0$ level have been performed at a wavelength of 687 nm (see figure 3.7) which corresponds to the $^5D_0 \rightarrow {}^7F_0$ transition of Sm^{2+}. These measurements yielded different lifetimes for different host materials: The measured lifetime of the Sm-doped $BaCl_2$ sample is (1.65 ± 0.02) ms, the lifetime for $BaBr_2$ as host material for the Sm^{2+} ions is (0.5 ± 0.01) ms. The measured lifetimes correspond very well with the literature [31].

3.2.3 Zirconium Fluoride Glass and Glass Ceramics

Preliminary investigations of Sm-doped $BaCl_2$ and $BaBr_2$ single crystals were done in the last section. Now Sm-doped glass ceramics which were co-doped with chlorine or bromine ions are investigated. In theses glasses were during a subsequent annealing process $BaCl_2$ or $BaBr_2$ nanoparticles formed. Samarium can enter the glass matrix either in its divalent form and/or as a trivalent ion. The different energy levels were shown in the last section (see figure 3.3). The composition of the samarium doped glasses are given in table 3.1.

Some problems occurred during the production process of the Sm-doped FZ glasses with the charge level of the dopant. The first glasses became immediately ceramic on pouring. This was solved by decreasing the temperature of the mold from 200 °C down to 150 °C, which enabled the glasses to remain transparent. FBZ 95 and FBZ 104 have a reddish color which originates from Sm^{2+}; the other glasses stay colorless. However, fluorescence measurements show Sm^{3+}. An attempt to reduce Sm^{3+} was made by adding LiH (2 wt%) or NH_4HF_2 (2 wt%), then remelted and pouring the mixture. FBZ 114 was made with new $SmBr_2$ material, but also stayed colorless. In [50] a procedure to reduce the Sm^{3+} within an H_2-N_2 atmosphere was described, but was not successful in this case.

Fluorescence

The fluorescence spectrum of FBZ glass ceramics containing Sm^{2+} ions (Fig. 3.8 (a), solid curve) shows relatively sharp lines of Sm^{2+} at 690, 700, 730, 765, and 815 nm which originate from $^5D_0 \rightarrow {}^7F_J$ transitions with $J = \{0, 1, 2, 3, 4\}$. In addition to the narrow line emissions, a broadband emission peaking at $\sim$ 700 nm can be observed; the broadband emission can be attributed to a

	ZrF_4	BaF_2	BaX_2	LaF_3	AlF_3	NaF	NaX_3	YF_3	InF_3	SmX_2
FBZ 93	52	20	-	1.5	3	5	15	1.5	1	1
FBZ 95	52	5	15	1.5	3	5	15	1.5	1	1
FBZ 104	52	20	-	1.5	3	5	15	1.5	1	1
FCZ 108	52	10	10	3.5	3	-	20	-	0.5	1
FZ 109	52	20	-	3.5	3	20	-	-	0.5	1*
FBZ 114	52	20	-	1.5	3	5	15	1.5	1	1
FCZ 115	52	10	10	1.5	3	-	20	1.5	1	1*

Table 3.1: Composition of the Sm-doped glasses in mole percent. The name of the samples is a composition of the abbreviation fluorobromo- (FBZ) or fluorochlorozirconate (FCZ) given by the compounds of the FZ glasses and an inventory number. For both glasses marked with an asterisk (*) SmF_2 was used. Only the red marked glasses contain divalent Sm as dopant.

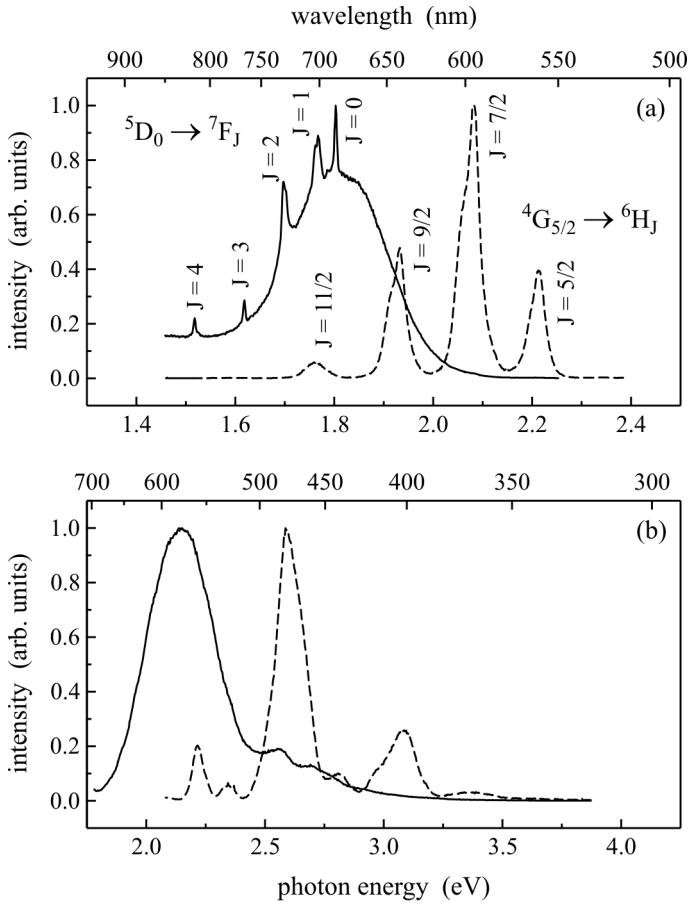

Figure 3.8: Normalized fluorescence spectra of FBZ glasses containing Sm^{2+} (solid curves) or Sm^{3+} (dashed curves). (a) Emission spectra excited at 590 nm (Sm^{2+}) and at 476 nm (Sm^{3+}), (b) excitation spectra detected at 730 nm (Sm^{2+}) and at 640 nm (Sm^{3+}). All spectra were recorded at room temperature.

$4f^55d \rightarrow 4f^6$ transition [31]. The Sm^{2+} excitation spectrum is shown in figure 3.8 (b), solid curve. The spectrum was detected for the 730 nm emission arising from the $^5D_0 \rightarrow {}^7F_2$ transition. It shows a broad band peaking at 583 nm with a full width at half maximum of around 80 nm. These excitation bands can be attributed to the closely spaced ^6H energy levels of the $4f^55d$ state. The two smaller peaks on the shoulder of the broad excitation band in the blue spectral range result from the transition of the ground state $^7F_0$ into the excited states $^5L_7$ (481 nm) and $^5L_8$ (460 nm). Both are $4f \rightarrow 4f$ transitions of Sm^{2+}.

The dashed curve in figure 3.8 (a) shows the Sm^{3+} emission bands in FBZ glasses. These emissions are caused by transitions starting from the same excited state $^4G_{5/2}$ but relaxing to different ground state levels: $^6H_{5/2}$ (560 nm), $^6H_{7/2}$ (595 nm), $^6H_{9/2}$ (640 nm), and $^6H_{11/2}$ (705 nm), respectively. The results

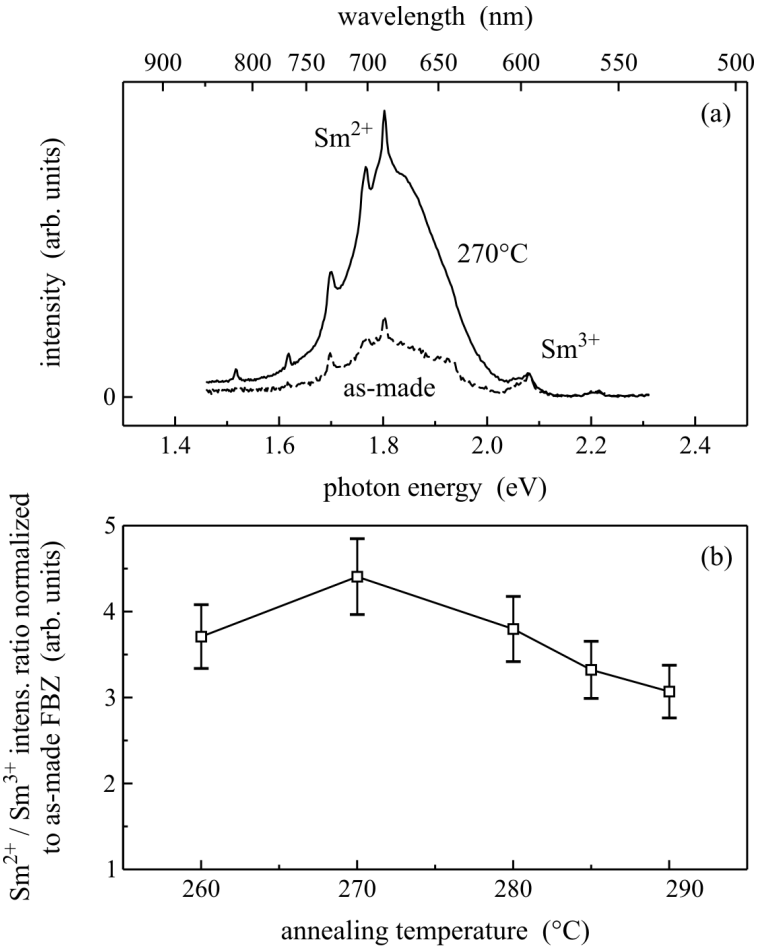

Figure 3.9: (a) Emission spectra of FBZ glasses containing both Sm^{2+} and Sm^{3+}, as-made and annealed for 20 min at 270°C. (b) Sm^{2+} / Sm^{3+} fluorescence intensity ratio vs. annealing temperature normalized to as-made FBZ. The line is a guide to the eye.

agree with previous findings in Sm^{3+}-doped FZ fibers [51]. The corresponding excitation spectrum is depicted in figure 3.8 (b), dashed curve. The spectrum was recorded for the 640 nm emission depending on the $^4G_{5/2} \rightarrow {}^6H_{9/2}$ transition. In the case of Sm^{3+} the $4f \rightarrow 4f^5 5d$ transitions are all in the far VUV (energies about 70.000 cm^{-1} [30] or about 8.7 eV). So all detectable excitations depend on the $4f \rightarrow 4f$ transition. The observed excitation bands can be attributed to the transitions starting at the ground state $^6H_{5/2}$ to the $^4G_{3/2}$ (559 nm), $^4F_{3/2}$ (527 nm) energy levels in the green spectral range. Due to overlapping energy levels like the $^4I_{11/2}$ and $^4I_{13/2}$ or $^6P_{5/2}$, $^4M_{19/2}$, $^4L_{13/2}$, $^6P_{3/2}$, and $^4F_{7/2}$ with their maximum at 478 nm and 402 nm, respectively, broad excitation bands were formed in the blue [52]. Between these bands lies another excitation at 440 nm corresponding to the $^6H_{5/2} \rightarrow {}^4I_{15/2}$. In combination the energy levels $^4F_{9/2}$, $^4D_{3/2}$, and $^6P_{5/2}$ produces a wider excitation band in the UV at around 368 nm.

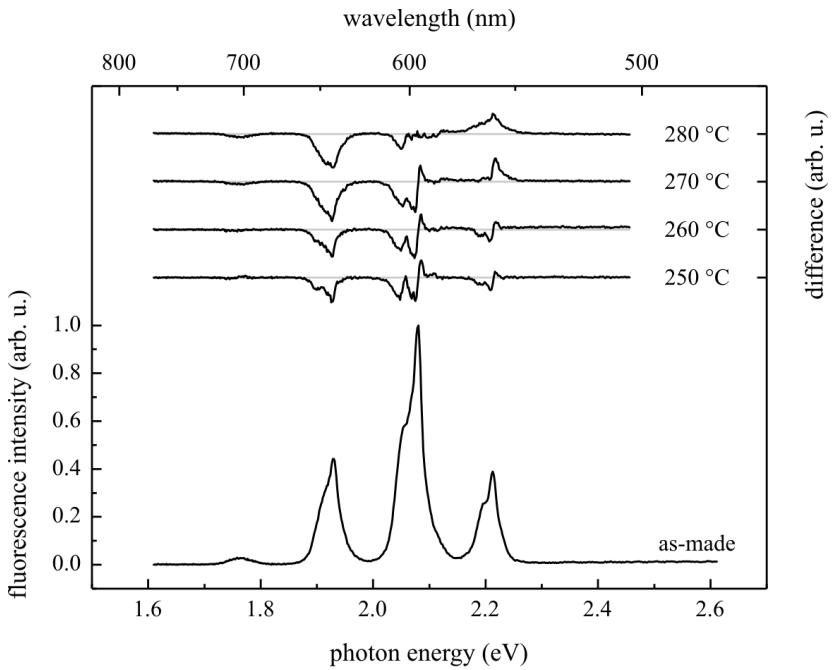

Figure 3.10: Emission spectra of FCZ 115 glass samples containing only Sm^{3+}. The measured spectrum of the as-made glass is shown. For the samples annealed for 20 min at 250 °C, 260 °C, 270 °C, and 280 °C the differences in the signal compared to the as-made are plotted.

Fig. 3.9 (a) shows the fluorescence spectra of the FBZ 104 glass samples. When this emission spectra is compared to figure 3.8 (a) a combination of the Sm^{2+} and Sm^{3+} fluorescence spectra can be seen. This FBZ glass contains Sm^{2+} and Sm^{3+} ions. Upon annealing the Sm^{2+} fluorescence intensity is increased by a factor of 4-5 with respect to the 270°C annealed sample (solid curve); the Sm^{3+} intensity does not change upon annealing within the experimental error. The Sm^{2+}/Sm^{3+} ratio versus annealing temperature is plotted in figure 3.9 (b). For an annealing temperature of 270 °C for 20 minutes a maximum increase for the Sm^{2+} fluorescence intensity in comparison with the Sm^{3+} intensity can be achieved. The Sm^{2+}/Sm^{3+} ratio was normalized to the value of the as-made sample.

Figure 3.10 shows the emission spectra of the as-made glass of the FCZ 115 glass series. The four observed emissions can be assigned to a Sm^{3+} doping, all starting from the $^4G_{5/2}$ energy level. No evidence of Sm^{2+} ions can be found. Upon annealing the shape and intensity of the spectra change. The difference between the intensities of the emission spectra of the annealed sample and the as-made glass was calculated for all annealing temperatures and is also shown this figure. The emission corresponding to the $^4G_{5/2} \rightarrow {}^6H_{7/2}$ shifts from

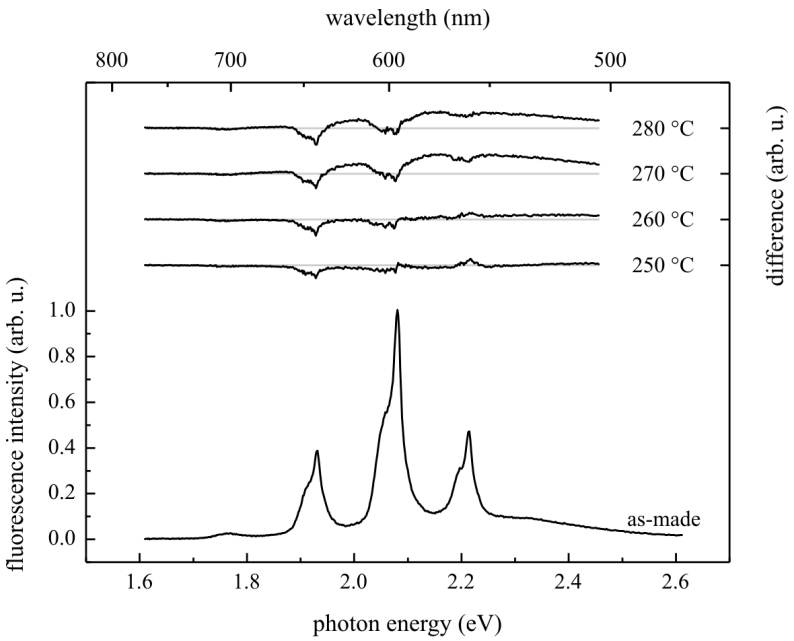

Figure 3.11: Emission spectra of FCZ 114 glass samples containing only Sm^{3+}. The measured spectrum of the as-made glass is shown. For the samples annealed for 20 min at 250 °C, 260 °C, 270 °C, and 280 °C the differences in the signal compared to the as-made are plotted.

595.6 nm for the as-made glass to 595 nm for the glass ceramics annealed at 250, 260, and 270 °C, observable in the difference spectra as a minimum-maximum structure at around 595 nm. Additionally a decrease of the emission intensity around 640 nm ($^4G_{5/2} \rightarrow {}^6H_{9/2}$) is observable. In the spectral range between 620 and 780 nm where Sm^{2+} emits a broad band ($4f^55d \rightarrow 4f^6$) superimposed by sharp emissions ($^5D_0 \rightarrow {}^7F_J$ with $J = \{0, 1, 2, 3, 4\}$) no increase in the emission intensity can be found. In figure 3.11 the spectra of a different Sm-doped FCZ glass is shown. Only Sm^{3+} emissions are observable. A broad background in the range between 500 and 750 nm increases during the thermal treatment process. Once again, no emission bands or peaks of Sm^{2+} appear in these spectra.

X-Ray Diffraction

The XRD data of FBZ glass ceramics containing Sm^{2+} ions are comprised of very broad peaks at about 26° and 47°, typical for glasses close to the ZBLAN formulation for copper $K_{\alpha 1}$ radiation [53]. In addition, relatively sharp peaks are superimposed on the broad glass background; these peaks grow upon annealing for 20 min at temperatures between 260 and 290°C. Fig. 3.12 (a) shows the XRD data for the as-made, the 270°C, and the 290°C sample. The sharp peaks can be identified as reflections from hexagonal $BaBr_2$; the bar graph

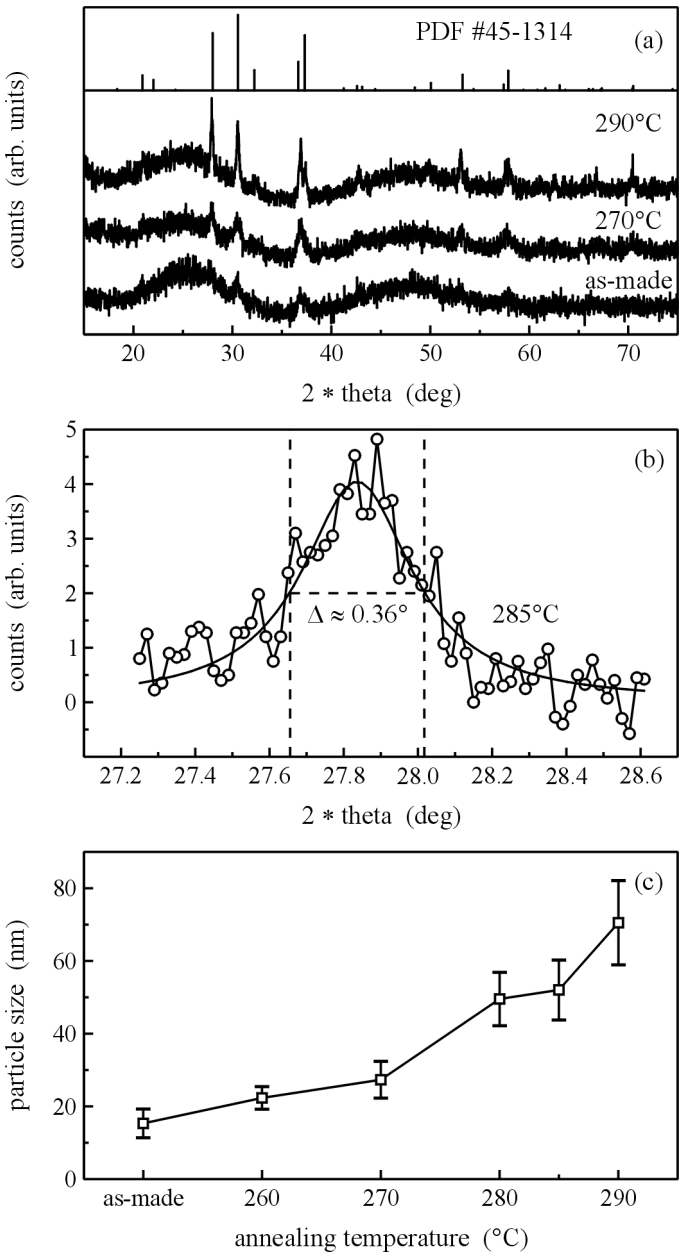

Figure 3.12: (a) XRD data for Sm^{2+}-doped FBZ glasses as-made and annealed for 20 min at 270 and 290 °C. The line pattern of hexagonal phase $BaBr_2$ (PDF #45-1314) is shown for comparison. (b) XRD peak used for the particle analysis of the 285 °C sample and the corresponding Lorentzian fitting curve. (c) Particle size versus annealing temperature. The line is a guide to the eye.

in figure 3.12 (a) represents the corresponding powder diffraction data; powder diffraction file (PDF #45-1314) [54]. There is no phase transition from the hexagonal to orthorhombic phase $BaBr_2$ as was found in Eu-doped FBZ glass ceramics [55].

The XRD peaks are wider than the instrumental resolution of 0.085°, suggesting size-broadening effects. The particle size can be determined by using the Scherrer formula [42]

$$d = \frac{K \cdot \lambda}{(\Delta - 0.085^\circ) \cdot \cos(\vartheta)} \tag{3.1}$$

with d the particle size, K the Scherrer constant (which is set to one in our analysis), λ the wavelength of the incident x-ray beam, 2ϑ the peak position of the reflection, and Δ the full width at half maximum of the reflection. Stress or strain effects which may also lead to additional line broadening are not considered. The Scherrer formula is applied to the (111) reflection of hexagonal phase $BaBr_2$ at around 28°. For fitting the line profile a Lorentzian was used. Figure 3.12 (b)) gives an example for the fitted function to the XRD pattern of the 285 °C annealed sample.

The particle sizes of the as-made sample and after thermal processing at 260 and 270°C are between 15 and 30 nm; for annealing temperatures at 280°C and above the particles grow from 50 nm to about 70 nm (Fig. 3.12 (c). Despite the poor signal-to-noise ratio of the XRD reflections, the Scherrer analysis provides a first estimate of the particle size; there is a trend to bigger particles for higher annealing temperatures. The particle growth proceeds from the precipitation of small hexagonal nanocrystals through Ostwald ripening: Small particles will re-dissolve, and the larger ones will grow at the expense of the smaller ones.

Fluorescence Lifetime

Fig. 3.13 (a) and (b) show the fluorescence decay curves for Sm^{2+} and Sm^{3+} in as-made FBZ and FBZ glass ceramics annealed for 20 min at different temperatures. The Sm^{2+} decay was recorded for the $^5D_0 \rightarrow {}^7F_0$ transition (690 nm) and the Sm^{3+} decay for the $^4G_{5/2} \rightarrow {}^6H_{7/2}$ transition (595 nm). The fluorescence lifetimes of the narrow line ($^5D_0 \rightarrow {}^7F_J$) and the broad band ($4f^55d \rightarrow 4f^6$) emissions of Sm^{2+} are identical within experimental error. Fig. 3.13 shows that the Sm^{2+} fluorescence lifetime in FBZ glass ceramics increases upon annealing. The lifetime of Sm^{3+}, however, does not change upon thermal processing; it is (2.2±0.2) ms for the as-made and all annealed samples.

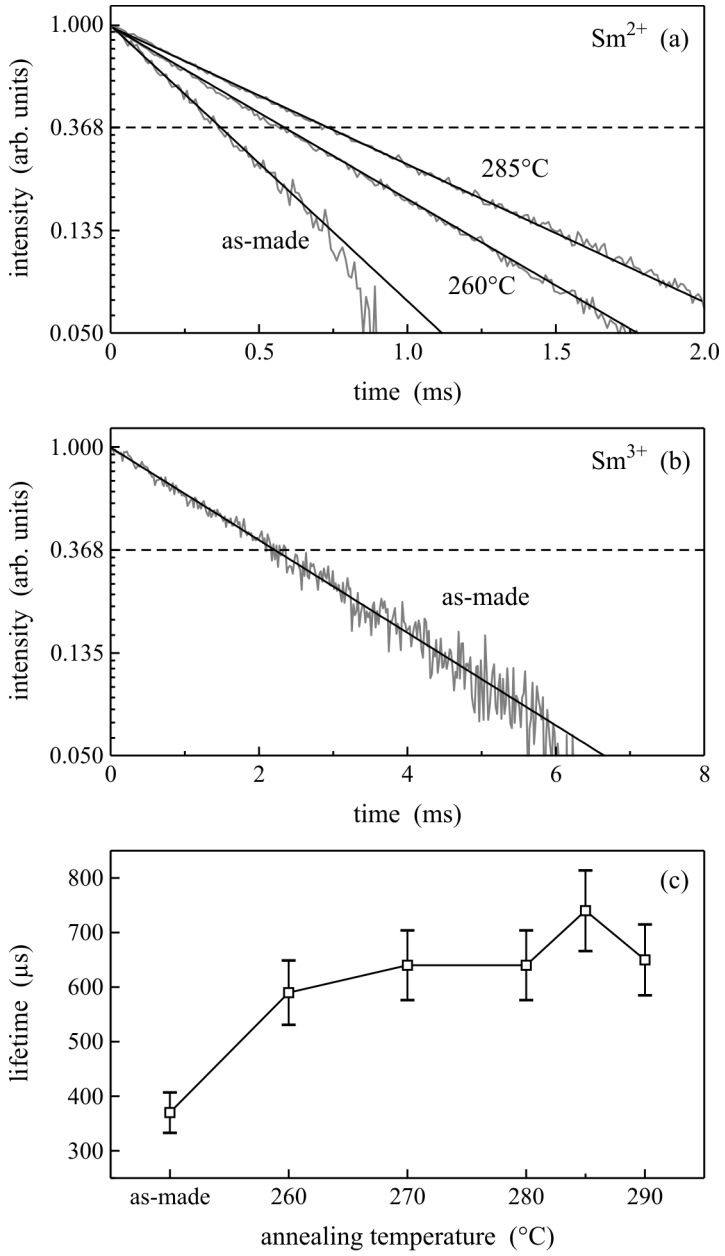

Figure 3.13: Decay of the Sm fluorescence in FBZ glasses. (a) The Sm^{2+} emission was detected at 690 nm ($^5D_0 \rightarrow {}^7F_0$). (b) The Sm^{3+} emission was detected at 595 nm ($^4G_{5/2} \rightarrow {}^6H_{7/2}$). (c) Decay time of the Sm^{2+} fluorescence in FBZ glass ceramics versus annealing temperature. The line is a guide to the eye. All measurements were carried out at room temperature; the fluorescence was excited at 590 nm for Sm^{2+} and at 476 nm for Sm^{3+}.

3.3 Discussion

Fluorescence, x-ray excited fluorescence and afterglow spectra show that Sm^{2+} can be incorporated into $BaCl_2$ and $BaBr_2$ single crystals and elucidates therein its characteristic optical properties. In particular, a broad band emission superimposed by narrow emissions when excited in the blue-UV spectral range is found. Both the fluorescence efficiency and lifetime of Sm^{2+} in FBZ glass ceramics can be significantly increased upon appropriate annealing. The investigation of samples which contain Sm^{2+} and Sm^{3+} ions showed that the annealing affects the fluorescence properties of Sm^{2+} while those of Sm^{3+} remain unchanged.

Most photons were emitted due to the broad band emission of Sm^{2+} arising from the $4f^55d \rightarrow 4f^6$ transition (figure 3.4). By comparing the emission spectra of the Sm-doped $BaCl_2$ to the $BaBr_2$ crystals, the $BaCl_2$ doped crystals show a less intense broad band emission and narrow emissions with smaller line width. Some of the Sm-doped ZBLAN glasses show an Sm^{3+}.

Lifetime measurement were performed for Sm^{2+} in $BaBr_2$, $BaCl_2$ and FBZ glass ceramics, whereas the Sm^{3+} fluorescence decay was only measured in fluorozirconate based glasses. The fluorescent decay lifetime of the 687 nm emission ($^5D_0 \rightarrow {}^7F_0$) differs in the single crystals; the doped $BaCl_2$ shows lifetimes that are a factor of 3 longer compared to the $BaBr_2$ crystals. This is evidence for less phonons or a smaller maximum phonon frequency in $BaCl_2$. Consequently, the Sm^{2+} emissions in $BaCl_2$ crystals show narrower emission linewidths. The lifetime measurements of Sm doping in the Sm^{2+} and Sm^{3+} doped glass shows a lifetime for the trivalent state that is a factor of 4.7 longer than the Sm^{2+} lifetime. The different annealed glass ceramics show an interesting phenomena that the Sm^{2+} lifetime increases, but the Sm^{3+} lifetime does not change within experimental error upon annealing; this indicates that some of the Sm^{2+} present in the glass matrix enters the $BaBr_2$ nanocrystals, which are formed during thermal processing. Sm^{2+} probably substitutes for barium on a regular lattice site, while the incorporation of Sm^{3+} requires charge compensation. The Sm^{2+} lifetime therefore has contributions from Sm^{2+} in the glass and Sm^{2+} in the nanocrystals. Since the fluorescence lifetimes increase upon annealing the phonon energies of the $BaBr_2$ nanocrystals are smaller than those of the FZ base glass, i.e. the non-radiative losses are reduced, the overall measured lifetime is longer and thus the fluorescence is more efficient.

It was shown that upon annealing the $BaBr_2$ nano-particles in the FBZ glass ceramic grow. The particle diameters, after thermal processing at 260, 270, and 280 °C, are between 15 and 60 nm; for annealing temperatures at 280 °C and above, the particles grow rapidly and their sizes become >100 nm (figure 3.12(b)). Due to the larger particle volume, more Sm^{2+}-ions are incorporated into the nanocrystalls, leading to a fluorescence emission enhancement (figure

3.9(a) and (b)).

Fluorescence intensity versus annealing temperature plot (see fig. 3.13(b)) does not follow the trend of the fluorescence lifetime vs. annealing temperature (figure 3.12(c)) or the particle size vs. annealing temperature (figure 3.12(b)): For annealing temperatures at 280°C and above the fluorescence is slightly reduced with respect to the value of the 270°C sample. It is assumed that for higher annealing temperatures light scattering effects play an increasingly important role. The $BaBr_2$ particles now have a size of greater than 50 nm, which may cause more light scattering and thus slightly reduced fluorescence intensities. Additionally, due to the growing particles, higher phonon frequencies can exist within the particles, which leads to higher losses through non-radiative decays.

It is expected that the fluorescence efficiency, as well as the lifetime, depends significantly on the quantity of Sm^{2+} ions incorporated into the nanocrystals and how large the $BaBr_2$ nanocrystals are. The nominal Sm-doping level for the glass is 1 mol% but the number of Sm^{2+} ions present in the nanocrystals is probably much smaller than that. Future work will be focused on optimizing the Sm^{2+} concentration in the nanocrystals.

However, it was not possible to produce another glass containing only Sm^{2+} after the FBZ 104. Also it was not possible to reduce the trivalent samarium to divalent samarium in the glass ceramics. An attempt was made to increase the intensity of the Sm^{2+} by a subsequent annealing step, as shwon in figure3.9. No evidence was found for a Sm^{2+} in any of the glasses (see figures 3.10, 3.11, and A.2).

4 Up-Conversion based on Nd and Er

The efficiency of a solar cell can be increased significantly with a process, in which infrared photons are converted to visible photons. Second harmonic generation or two-photon absorption up-conversion fulfils this condition. In the up-conversion process two or more IR photons are converted to a visible photon that can be absorbed by a solar cell. Trupke *et al.* [5] calculated the theoretical limit of a single junction solar cell which uses additional up-conversion processes to an over-all external quantum efficiency of 47.6 % which lies above the Shockley-Queisser limit of 30.9 % [56]. The up-conversion process an optically active center. From chapter 2 it is known that intermediate excited states with long lifetimes are needed. Rare earth ions are known for discrete energy levels and relatively long excited state lifetimes. When embedded in a low phonon glass matrix non-radiative losses can be reduced. A good choice due to their low phonon frequencies of ~ 500 cm^{-1} are glasses based on the well known ZBLAN composition [21]. From prior investigations it is known that glass ceramics with nanocrystals embedded in rare earth ions show an enhanced fluorescence efficiency [27, 28].

4.1 Simulations

Trupke *et al.* [5] made several theoretical assumptions in their calculations and vary the band gap to reach the the theoretical maximum external quantum efficiency. To determine more realistic limits, further calculations were performed; the details appear in appendix B. Figure 4.1 shows the results of the calculations as a contour plot as a function of the absorption of the up-converting layer and the internal quantum efficiency, both given in %. All points were normalized to the initial system without an up-converting layer. The maximum, for 100 % absorption and internal quantum efficiency, is at 1.264, which means an enhancement of 26.4 % in comparison to the system without an up-converting layer. The diagram does not show any blue areas, i.e. the calculated overall efficiency never drops below 1. An upconverter-solar cell system provides always better EQE values than a silicon solar cell alone. The minor enhancement compared to the calculations of Trupke is affected by the difference of the AM1.5 and the blackbody spectrum (figure 1.1); atmospheric absorption bands are centered at 1130, 1400, and 1875 nm.

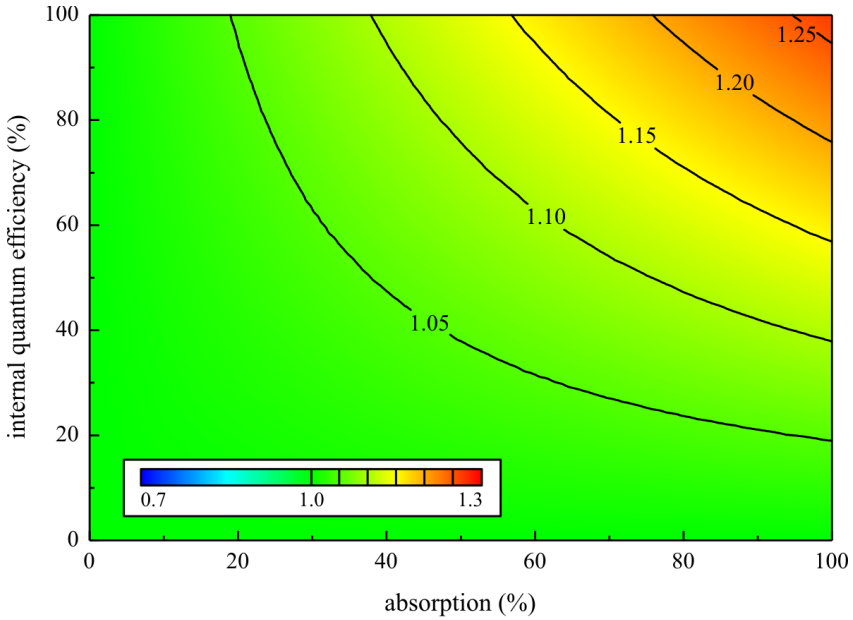

Figure 4.1: Calculated ratio between solar cell with and without an up-converting layer in dependency on absorption of the layer and internal quantum efficiency. For 100 % absorption and internal quantum efficiency a maximum of 1.264 was calculated; 1.0 for the minimum. The color stands for the calculated ratio (see color scale in the lower left corner).

4.2 Dopant: Neodymium

4.2.1 Motivation

For the first system neodymium was chosen as a dopant. Nd^{3+} is already well known for its up-conversion application in up-conversion lasers. It offers a large amount of energy levels that can be used for the up-conversion process and it possess lifetimes of several hundreds μ-seconds.

The aim is to produce a model system with Nd-doped nanocrystals embedded in low phonon glass ceramics that show intense up-conversion when excited with infrared photons. For a better understanding of the optical behavior of the embedded nanoparticles it is essential to investigate the rare earth doping in the corresponding bulk material. Due to the fact that $BaCl_2$ nanoparticles are formed upon subsequent annealing of the glass matrix, investigations on Nd-doped $BaCl_2$ single crystals are performed. After a basic set of measurements on the Nd-doped $BaCl_2$, the optical and structural properties of Nd-doped glass ceramics with different annealing temperatures as a function of their Nd doping level are investigated.

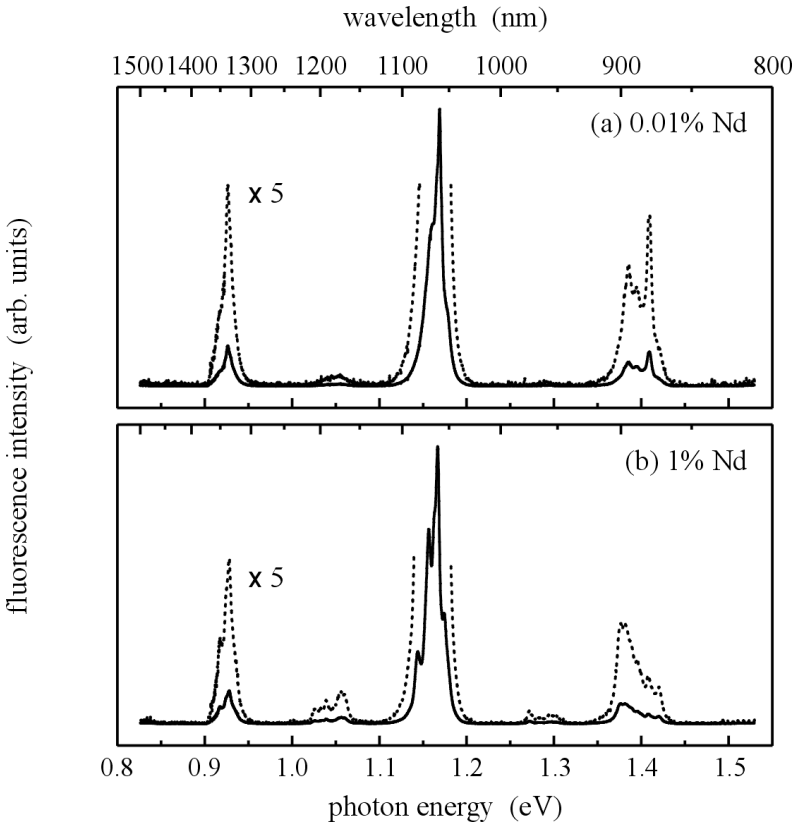

Figure 4.2: Normalized fluorescence spectra of (a) 0.01 mol% and (b) 1 mol% Nd^{3+}-doped $BaCl_2$. The fluorescence was recorded under CW infrared laser excitation at 796 nm. Parts of the fluorescence spectra (dotted curves) are expended as indicated.

4.2.2 Barium Chloride

Fluorescence and Excitation

Fig. 4.2 shows the fluorescence spectra of 0.01 (top) and 1 mol% (bottom) Nd^{3+}-doped $BaCl_2$ single crystals in the infrared spectral range between 800 and 1500 nm. The samples were excited with a 796 nm LD. The most intense emissions observed at 890, 1065, and 1340 nm are typical for Nd^{3+} and can be assigned to $^4F_{3/2} \rightarrow {}^4I_{9/2}$, $^4I_{11/2}$, and $^4I_{13/2}$ transitions, respectively. Blowing up the spectrum by a factor of 5 the 1 mol% sample clearly shows additional emission bands at approximately 960 and 1190 nm; these line groups are barely observable in the 0.01 mol% doped sample. Comparing these emissions with the energy level diagram of Nd^{3+} it can be seen that they are probably caused by $^4F_{5/2}$ to $^4I_{11/2}$ and $^4F_{5/2}$ to $^4I_{13/2}$ transitions, respectively. All infrared Nd^{3+} emissions are more or less split by the crystal field [57]. The splitting effect is stronger in the 1 mol% Nd^{3+} doped crystal.

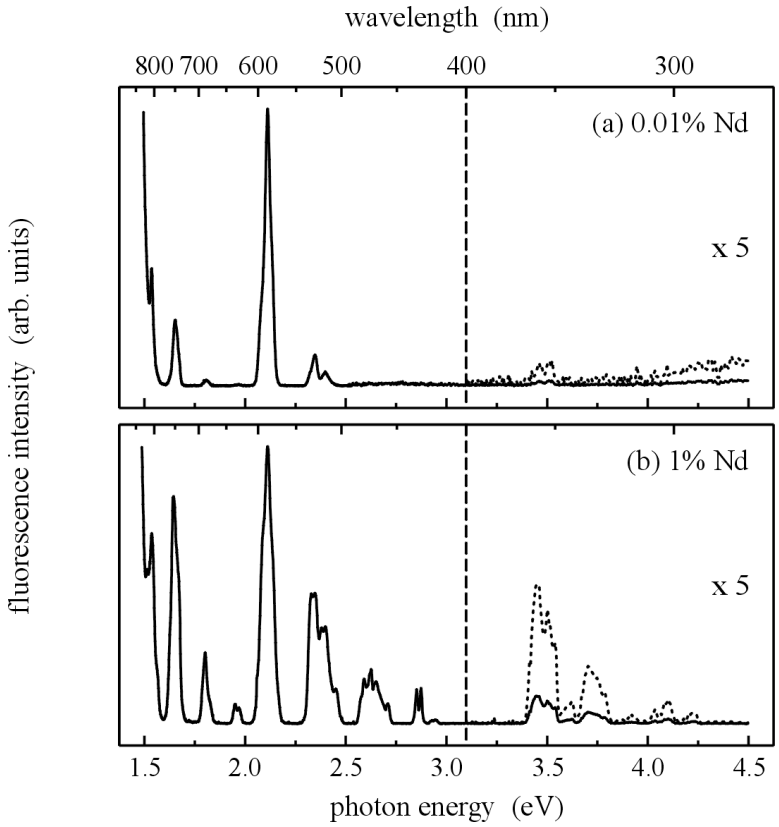

Figure 4.3: Normalized excitation spectra of (a) 0.01 mol% and (b) 1 mol% Nd^{3+}-doped $BaCl_2$. The emission was detected at 880 nm. All transitions start from the $^4I_{9/2}$ ground state. Parts of the excitation spectra (dotted curves) are expanded as indicated.

The corresponding excitation spectra for both samples are shown in figure 4.3. The spectra were recorded at 880 nm for the $^4F_{3/2} \rightarrow {}^4I_{9/2}$ transitions. They depend clearly on the Nd^{3+} concentration. The relative intensity ratio of the excitation bands of the 1 mol% sample differs significantly from that of the 0.01 mol% sample: The spectrum of the 1 mol% doped sample shows numerous excitation bands over the whole visible and ultraviolet spectral range. The excitation spectrum of the 0.01 mol% sample is in comparison relatively simple with one dominant band at 590 nm which can be assigned to $^4I_{9/2} \rightarrow (^4G_{5/2}, {}^2G_{7/2})$ transitions. Even in the expended spectrum none of the UV excitation bands seen for the 1 mol% doping level appear. The splitting effect is much stronger in the 1 mol% doped single crystal. Looking at the peaks around 515 nm, a more detailed structure can be seen in the 1 mol% Nd^{3+}-doped sample. Different sublevels of the $(^4G_{9/2}, {}^2K_{13/2}) \rightarrow {}^4I_{9/2}$ can be ascribed to these. Note, that for wavelengths longer than approximately 750 nm, scattered excitation light enters the spectra, whereas the 806 nm excitation ($^4I_{9/2} \rightarrow {}^4F_{5/2}$) is superimposed on this.

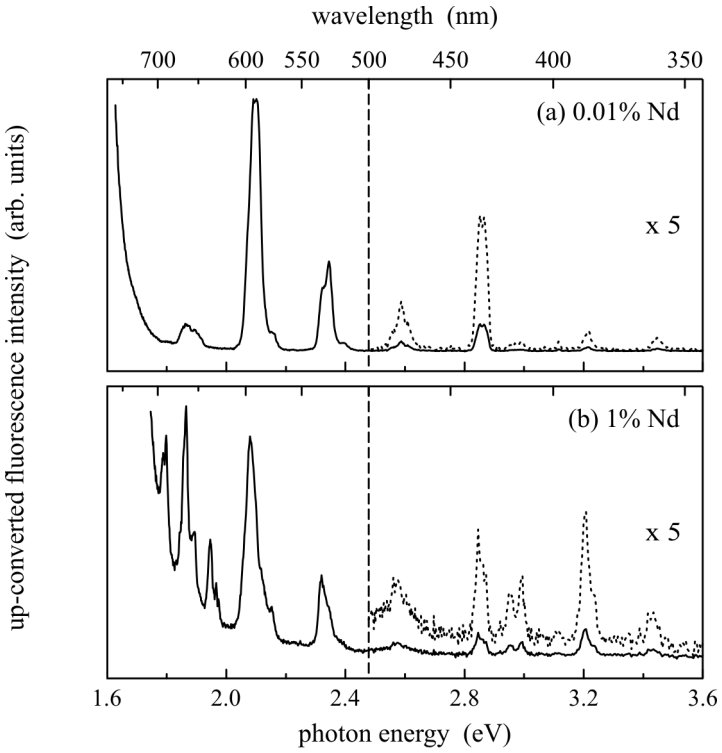

Figure 4.4: Normalized up-converted fluorescence spectra of (a) 0.01 mol% and (b) 1 mol% Nd^{3+}-doped $BaCl_2$ under CW infrared laser excitation at 796 nm. Parts of the up-converted fluorescence spectra (dotted curves) are expanded as indicated.

Converted Fluorescence

Up-conversion in the visible range can be observed at room temperature under excitation from a CW infrared laser diode emitting at 796 nm. The excitation is in resonance with the $^4I_{9/2} \rightarrow {}^4F_{5/2}$ transition of the Nd^{3+} ion. Figure 4.4 shows the up-converted fluorescence spectra for 0.01 and 1 mol% Nd-doped $BaCl_2$ in the $340 - 750$ nm spectral range. Scattered excitation light enters the spectrum at about 750 nm. After the $^4F_{5/2}$ level is populated through the excitation by a 796 nm photon, the ion relaxes to the $^4F_{3/2}$ level. This level has a relatively long life time due to its large energetic gap of more than 0.7 eV to the next lowest level $^4I_{15/2}$. The longer lifetime induces a higher probability for the ion to absorb another 796 nm photon before relaxing (through an emitted photon) to the ground state. Beside this ESA process an ETU process is also a possibility to reach levels with higher energies than the $^4F_{5/2}$ level. From these higher excited states many levels can be populated by non-radiative processes.

Figure 4.5 shows the Nd^{3+} energy levels and possible population routes to the higher states. The most intense emission bands are located in the green (530 nm), yellow (590 nm), and red (660 nm) region. They arise from the ^4G multiplets [58]. The ^4G multiplets, comprised of the $^4G_{9/2}$, $^4G_{7/2}$, and $^4G_{5/2}$

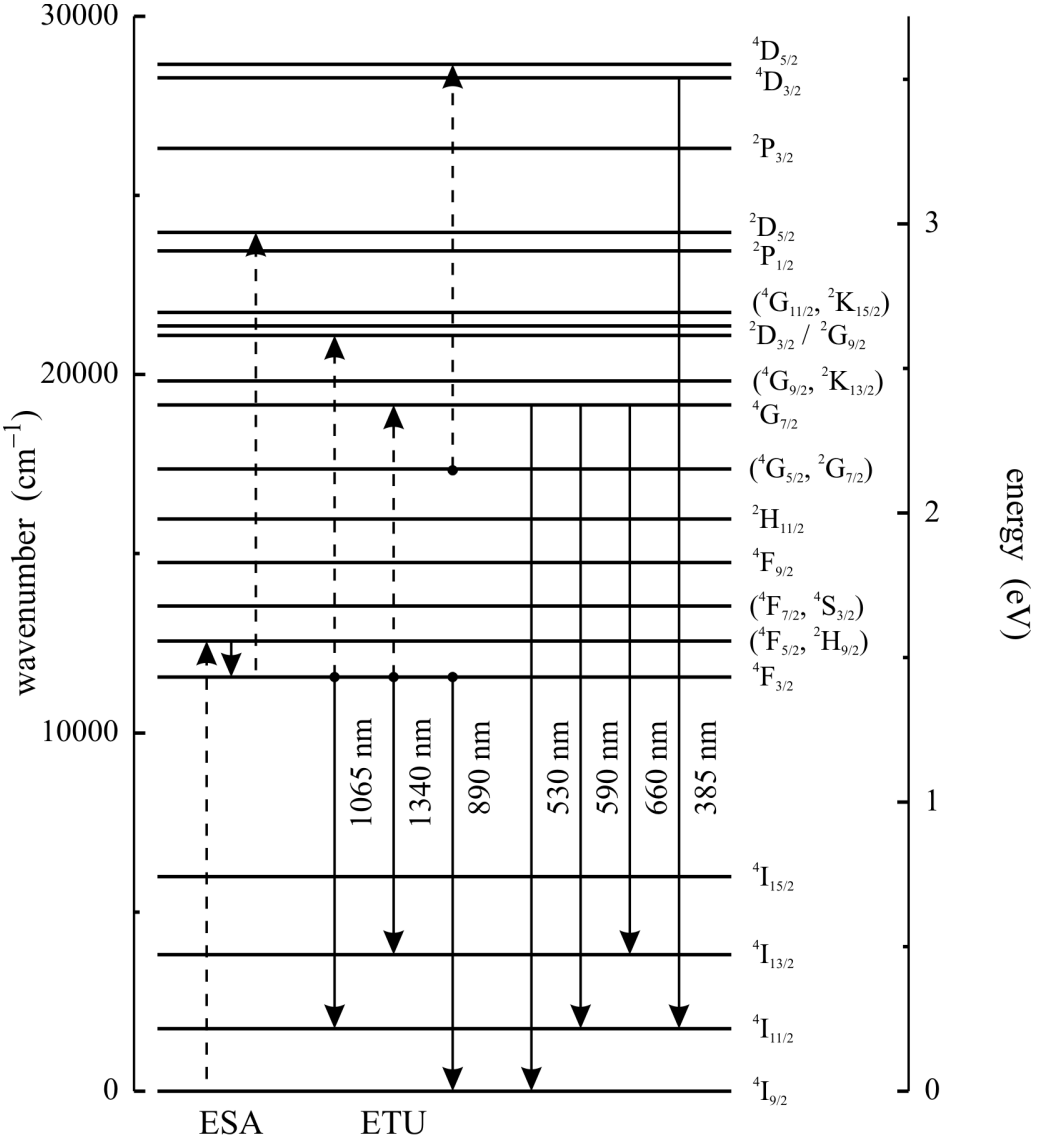

Figure 4.5: Energy level diagram of Nd^{3+} in FZ glasses [30, 58, 59]: The infrared and up-conversion emissions (solid arrows) and possible up-conversion routes (dashed arrows) are indicated.

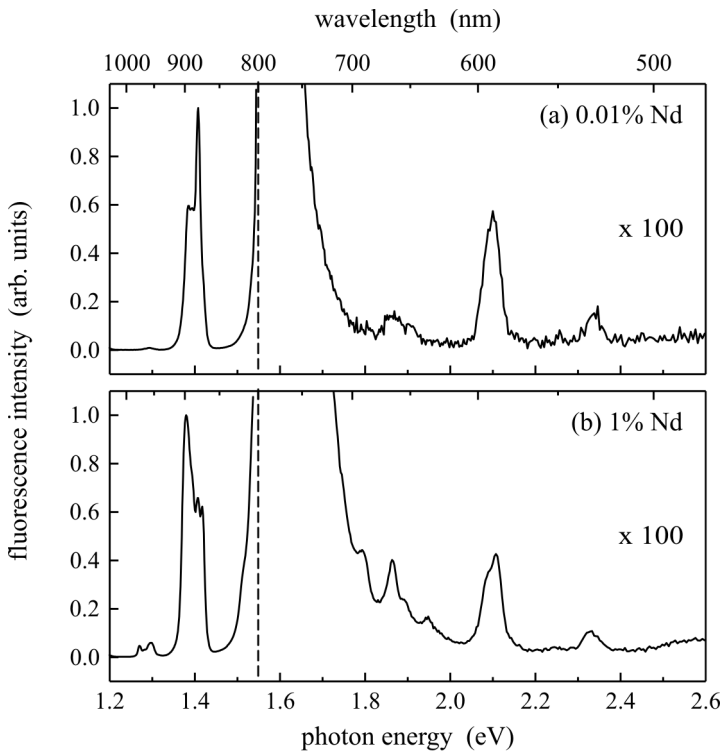

Figure 4.6: Fluorescence spectra of (a) 0.01 mol% and (b) 1 mol% Nd^{3+}-doped $BaCl_2$ under CW infrared laser excitation at 796 nm (dashed line). The spectra are normalized to the $^4F_{3/2} \rightarrow {}^4I_{9/2}$ transition at 890 nm, the up-converted fluorescence parts ($\lambda < 800$ nm) are expended by factor of 100. The spectra are corrected for the spectral sensitivity of the detector.

states, produce overlapping emission bands in the visible spectral range, and are therefore the strongest in the spectrum. The ^4G multiplets are energetically accessible with two 796 nm photons. The weak bands in the blue spectral range originate from the higher $^2P_{1/2}$ excited state. The two bands at 635 and 690 nm found in the 1 mol% Nd-doped sample are tentatively assigned to transitions from the excited states $^2H_{11/2}$ and $^4F_{9/2}$, respectively, to the $^4I_{9/2}$ ground state. The up-converted fluorescence bands in the UV spectral range at approximately 360, 385, and 415 nm are only accessible with three photons (Fig. 4.5). The highest observed energy band at 360 nm arises from a $^4D_{3/2}$ to $^4I_{9/2}$ transition; the 385 nm emission is from the same excited state, but depopulates to the $^4I_{11/2}$ ground state. The 415 nm emission can be attributed to a transition from the $^4D_{3/2}$ excited state to the $^4I_{13/2}$ ground state.

In figure 4.6 a direct comparison between the normal fluorescence and the up-converted fluorescence of the Nd-doped crystals is given. The one photon fluorescence efficiency at 890 nm arising from the $^4F_{3/2}$ level is by a factor of around 200 better than the efficiency of the strongest up-converted fluores-

cence at 590 nm in both samples. A direct comparison of the efficiencies of the emission and up-converted emission to the excitation intensity was not possible. The surfaces and sizes of the different $BaCl_2$ samples are not comparable; they are fragments of the grown single crystals. In addition to the high hygroscopic nature of the crystals an identical preparation of the samples was not possible. Scattering effects at the surface, different absorption volumes, and varying radiation patterns do not allow a normalization of the excitation. For PL and up-conversion spectra in a direct comparison they were recorded with the less sensitive silicon photo diode, rather than a photomultiplier. Therefore the signal-to-noise-ratio and the resolution of the spectra are not as good as the photomultiplier detected up-conversion spectra. Nevertheless, the main 2-photon up-converted emissions in the visible spectral range are clearly identifiable.

Lifetime Measurements

For up-conversion processes, the lifetime of the intermediate energy levels is of particular importance. Thus, lifetime measurements of the $^4F_{3/2}$ level have been performed at a wavelength of 880 nm (Fig. 4.7 a) which corresponds to the $^4F_{3/2} \rightarrow {}^4I_{9/2}$ transition. These measurements yielded different lifetimes for different Nd^{3+}-doping level: The measured lifetime of the 0.01 mol% sample is (280 ± 1) μs, the lifetime for the 1 mol% doping level is (49 ± 1) μs. This result was expected since energy transfer processes between neighboring Nd^{3+} ions lead to a shorter lifetime for the sample with the higher Nd^{3+} concentration.

To complete the picture on energy level lifetime also lifetime measurements on the two-photon up-converted fluorescence were performed. The Nd^{3+}-doped $BaCl_2$ single crystals were excited with a CW laser diode operating at 796 nm and the up-converted fluorescence decay was detected at 590 nm (4.7b) corresponding to transitions starting at the ^{4}G-multiplet and depopulated to the ground state. As expected and already observed for the infrared fluorescence lifetime, the measurements yielded different lifetimes for different Nd^{3+}-doping level: The lifetime of the two-photon up-converted fluorescence at 590 nm is (19 ± 0.5) μs and (9.5 ± 0.5) μs for the 0.01 and 1 mol% doped sample, respectively. Additionally, comparing the fluorescence with the up-converted fluorescence lifetimes it can be seen, that the higher energy levels (up-conversion) radiate with a shorter lifetime as the energy levels where the normal photoluminescence starts.

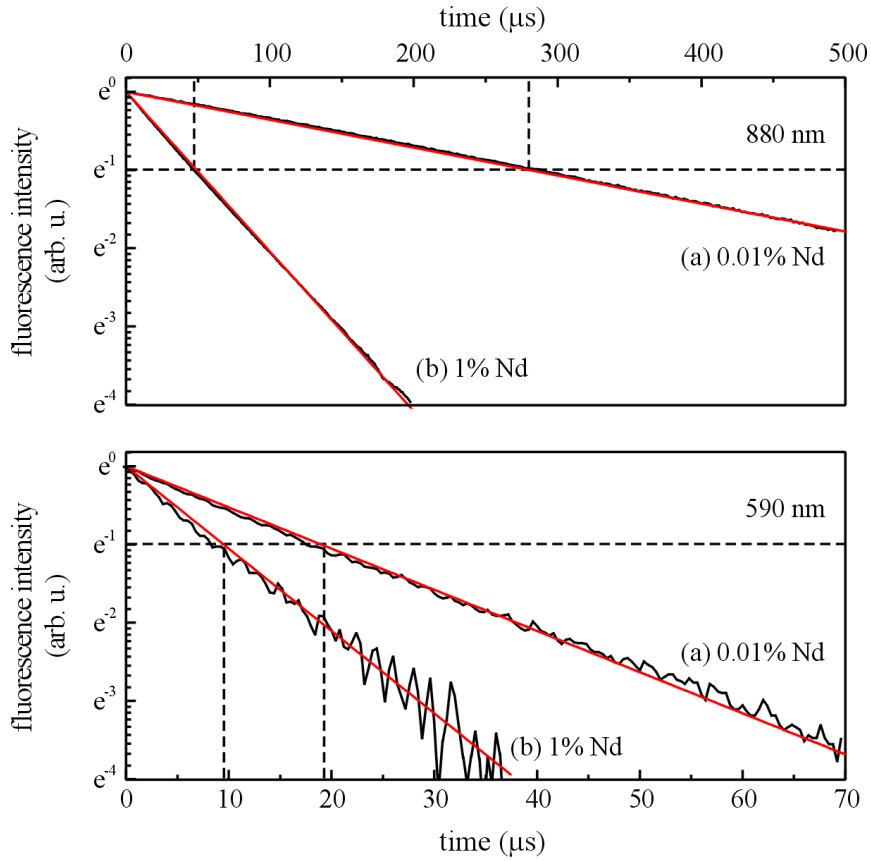

Figure 4.7: The upper measurements show the fluorescence decay of Nd^{3+} in $BaCl_2$ doped with (a) 0.01 mol% and (b) 1 mol% $NdCl_3$ at 880 nm. The lower diagram shows the up-converted fluorescence decay of $BaCl_2$ doped with (a) 0.01 mol% and (b) 1 mol% $NdCl_3$. The excitation was carried out with a pulsed infrared laser diode at 796 nm.

Power Dependence

Figure 4.8 shows the dependence of the emission intensity on the 796 nm excitation power for the infrared fluorescence band at 880 nm corresponding to the $^4F_{3/2} \rightarrow {}^4I_{9/2}$) transition and the most intense up-converted fluorescence band at 590 nm, which arises from transitions of the ^4G multiplets to the ground states. The power dependence was measured by inserting different optical filters (e.g. neutral density filters) in the pump beam. Fluorescence spectra were recorded over several orders of magnitude of excitation power, e.g. from approximately 130 mW (maximal laser diode output power) down to a few μW. For the emission at 880 nm, the slope is 0.996 and 0.992 for a Nd^{3+}-doping level of 0.01 and 1 mol%, respectively, e.g. an almost perfect linear dependence on the excitation power. Saturation effects or a decreasing slope for higher excitation powers are not observed. Up-conversion spectra of the 590 nm emission

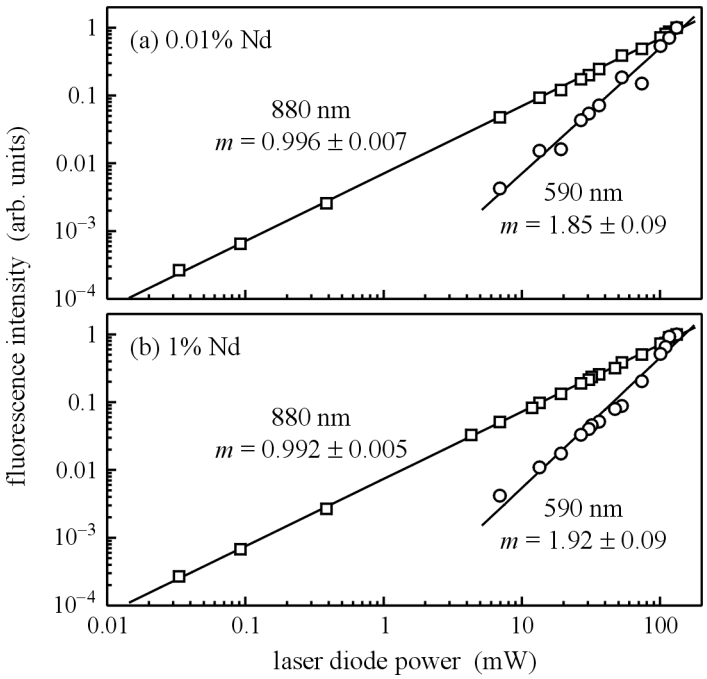

Figure 4.8: Power dependence (on double-logarithmic scale) of the fluorescence and up-converted fluorescence intensity in (a) 0.01 mol% and (b) 1 mol% Nd^{3+}-doped $BaCl_2$, recorded at the wavelengths indicated under CW laser diode excitation at 796 nm.

were recorded for excitation powers in the range from 130 mW down to 7 mW. For lower excitation powers the signal to noise ratio was too low for an exact analysis. For the up-converted fluorescence band, the slope is 1.85 and 1.92 for 0.01 and 1 mol%, respectively. Neither up-conversion power dependencies show saturation effects or a decrease of the fitted slope.

4.2.3 Fluorozirconate Glasses and Glass Ceramics

In the last section 4.2.2 the up-converted luminescence of $BaCl_2$ single crystals doped with $NdCl_3$ was discussed. A problem during these measurements was the hydroscopicty of $BaCl_2$. Crystals left for a day or longer in normal air, tarnish and become white, lose their physical stability, and crumble on contact. The easiest way to solve this problem is to embed $BaCl_2$ in a protective glass matrix. The fluorozirconate glasses, especially the ZBLAN glasses, are an ideal host material for barium chloride crystallites. In addition to the low phonon frequencies the ZBLAN glasses offer optimal transparency over a wide spectral range. Emission and excitation bands of embedded Nd^{3+} ions are neither influenced nor absorbed by the glass. Another advantage of these glasses lies in their production process conditions. They are not limited in their size, volume, and form, like single crystals, where the production price grows rapidly with the diameter of the crystal. In table 4.1 the compositions of the three glasses synthesized with chlorine doping are listed.

Differential Scanning Calorimetry

In further investigations glasses with different doping levels were made. All glasses are based on the well known ZBLAN composition [21]. One glass was doped with 1 mol% of $NdCl_3$ doping. It is comprised of $52{\cdot}ZrF_4$-$20{\cdot}BaF_2$-$20{\cdot}NaF$-$3.5{\cdot}LaF_3$-$3{\cdot}AlF_3$-$0.5{\cdot}InF_3$-$1{\cdot}NdF_3$ (values in mol %) and has no additional chlorine doping. The other three glasses have additional chlorine doping and are comprised of $(53-x){\cdot}ZrF_4$-$10{\cdot}BaF_2$-$10{\cdot}BaCl_2$-$(20-x){\cdot}NaCl$-$x{\cdot}KCl$-$3.5{\cdot}LaF_3$-$3{\cdot}AlF_3$-$0.5{\cdot}InF_3$-$x{\cdot}NdF_3$, where $x = 0.5,\ 1,\ 5$ (values in mol%). The differential scanning calorimetry (DSC) measurements of three fluorozirconate based glasses are shown in figure 4.9. Here a Nd-doped FZ (a), an undoped FCZ (b), and a Nd-doped FCZ (c) glass are investigated. The DSC data for the 1 mol% Nd-doped FZ glass (figure 4.9 (a)) shows a glass transition at $\sim$262 °C in good agreement with that observed in a pure FZ glass [21, 60] for a heating rate of 10 K/min. No crystallization peaks can be found upon doping the fluorozirconate glass with Nd only; however, crystallization is initiated if the glass is additionally doped with chlorine ions. Doping the FZ base glass

	ZrF_4	BaF_2	$BaCl_2$	LaF_3	AlF_3	$NaCl_3$	InF_3	KCl	$NdCl_3$
ZBLAN 112	52.5	10.0	10.0	3.5	3.0	19.5	0.5	0.5	0.5
ZBLAN 111	52.0	10.0	10.0	3.5	3.0	19.0	0.5	1.0	1.0
ZBLAN 113	48.0	10.0	10.0	3.5	3.0	15.0	0.5	5.0	5.0

Table 4.1: Composition of the Nd- and K-co-doped FCZ glasses in mole percent. The name of the samples is a composition of the abbreviation ZBLAN given by the compounds of the FZ glasses ([21]) and an inventory number. The glasses are sorted by their Nd doping concentration.

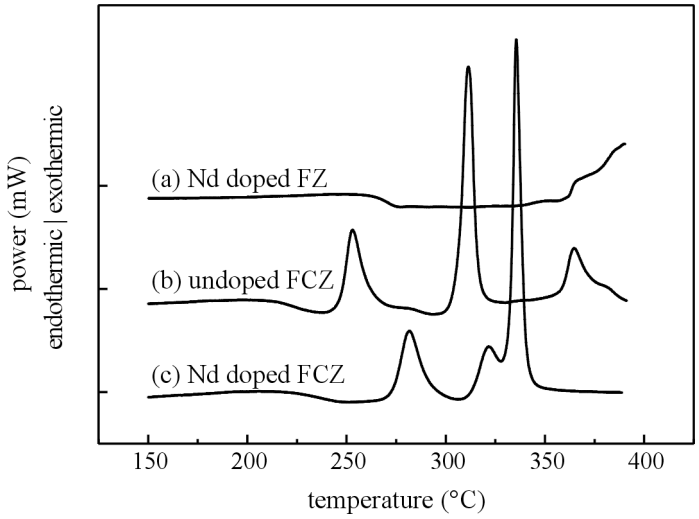

Figure 4.9: DSC measurements for FZ and FCZ glasses. From top to bottom are the measured curves of (a) Nd-doped FZ, (b) undoped FCZ and (c) Nd-doped FCZ glass.

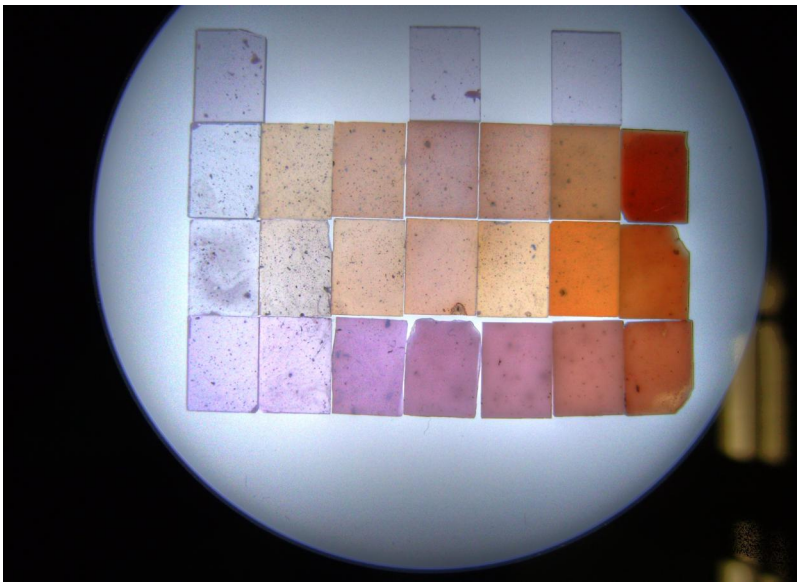

Figure 4.10: Picture of the sample illuminated from the back. The rows are from top to bottom: 1 mol% Nd-doped FZ, follwing the three Nd-doped FCZ glasses with 0.5, 1, and 5 mol% neodymium doping. The columns are the annealing temperatures; from left to right: as-made, 240, 250, 260, 270, 280, and 290 °C for 20 minutes.

additionally with chlorine (figure 4.9 (b)) shifts the glass transition temperature to ∼211 °C which is significantly less than that for the undoped FZ base glass. The exothermic peak at about 250 °C is assigned to the crystallization of hexagonal $BaCl_2$. The two peaks at ∼310 °C and ∼365 °C are also crystallization peaks; the latter one is also observed in pure FZ glass where the main glass crystallization starts at ∼350 °C [21]. For the as-made 5 mol% Nd-doped FCZ glass (4.9 (c)) the glass transition temperature is around 216 °C. Interestingly, the peak for the hexagonal phase $BaCl_2$ crystallization is now at ∼280 °C. The crystallization peak at 310 °C is shifted by 10 °C to 320 °C whereas the glass crystallization peak is now at ∼ 335 °C. Further DSC measurements were performed on the 5 mol% doped sample. They are added in appendix C.

Figure 4.10 shows the four synthesized glasses. The samples were illuminated from the back when the picture was taken. The glasses from top to bottom are: 1 mol% Nd-doped FZ, followed by the three Nd-doped FCZ glasses with 0.5, 1, and 5 mol% neodymium. Due to subsequent annealing of the sample at temperatures in the range of the crystallization temperature of the samples in three of the four glasses nano-crystals were formed in the glass matrix. Light scattering effects can be observed and became stronger with higher annealing temperatures. The columns are 20 minutes annealing temperatures for 20 minutes of as-made, 240, 250, 260, 270, 280, and 290 °C, from left to right. The first glass without additional chlorine doping, did not form any nano-particles. The characteristic $BaCl_2$ crystallization temperature shifted to lower temperatures due to additional chlorine doping or to higher temperatures with increasing Nd-doping; this can be observed in the picture.

X-Ray Diffraction

Figure 4.11 shows the x-ray diffraction (XRD) data for the as-made and annealed (for 20 minutes) 5 mol% Nd-doped FCZ glasses; temperatures are as indicated. The XRD data of the as-made sample consists of very broad peaks at about 26° and 47°, typical for glasses close to the ZBLAN formulation [55] for copper K_α radiation. For an annealing temperature of 240 °C (data not shown) no significant change in the XRD pattern can be observed. However, sharper peaks arise upon increasing the annealing temperature from 250 °C to 290 °C. These peaks can be identified as reflections from hexagonal $BaCl_2$ (space group $P\bar{6}2m$ (189), $a = 0.8066$ nm, $c = 0.4623$ nm, bar graph (PDF #45-1313) in figure 4.11) [54]. There is no phase transition from hexagonal to orthorhombic phase $BaCl_2$ as was found in other RE-doped FCZ glass ceramics [61, 62]. For the 290° C annealed sample, however, there are peaks from phases which have not yet been identified; they are marked with asterisks in figure 4.11.

The XRD peaks are wider than the instrumental broadening of 0.085°. The FWHM is becoming narrower with higher annealing temperatures, suggesting

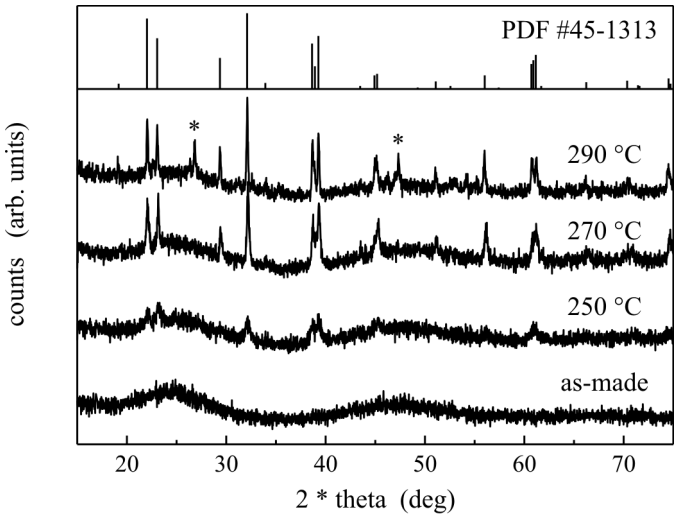

Figure 4.11: XRD data for the 5 mol% Nd-doped FCZ glass ceramic, as-made and annealed, for 20 min at 250 °C, 270 °C, and 290 °C. The curves are vertically displaced for clarity. The line pattern of hexagonal phase $BaCl_2$ (PDF #45-1313) is shown for comparison. The asterisks mark additional peaks from unidentified phases.

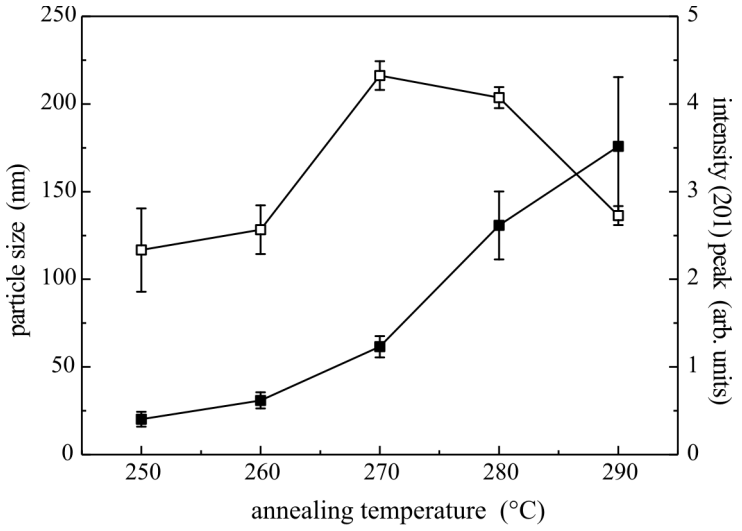

Figure 4.12: Particle size (full squares) and integrated intensity (open squares) of the (201) reflection vs. annealing temperature for hexagonal $BaCl_2$. The lines are a guide to the eye.

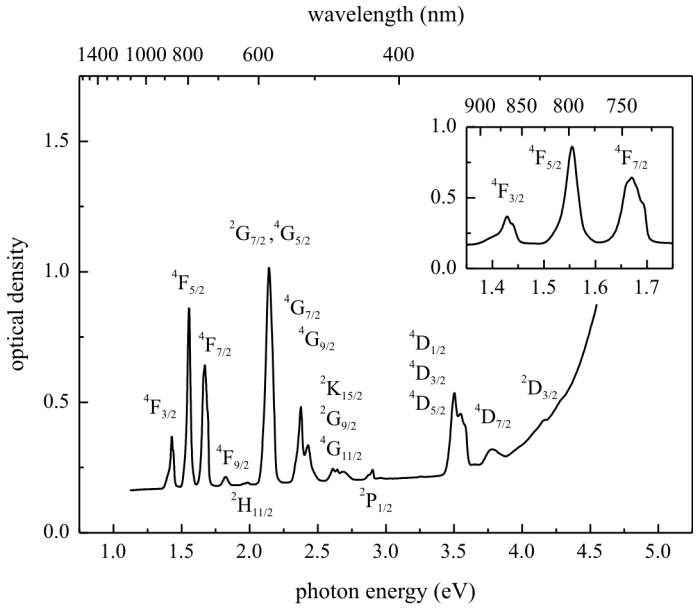

Figure 4.13: Optical density of a Nd^{3+}-doped FCZ glass sample. The labeled transitions start from the $^4I_{9/2}$ ground state and end on the levels indicated. The sample thickness was 1 mm. The inset shows an expanded version of the absorption band in the IR spectral range that will be used for excite the up-conversion.

size-broadening effects. The particle sizes can be estimated by using the Scherrer formula (see equation 2.11 in chapter 2) [42]. Any stress or strain effects, which may also lead to additional line broadening are not considered. The Scherrer formula is applied to the (201) reflection of hexagonal phase $BaCl_2$ at about 32°. For fitting the line profile a Lorentzian function was used. The particle diameters, after thermal processing at 250, 260, and 270 °C, are between 20 and 60 nm. The particles grow rapidly and their sizes become > 100 nm (figure 4.12, full squares) for annealing temperatures at 280 °C and above. The XRD linewidth of the (201) reflection for 280 °C and 290 °C annealing is too close to the instrumental resolution to allow a precise estimate of the particle size (see error bars in figure 4.12, full squares). In addition, figure 4.12, open squares, shows that for annealing above 270 °C the hexagonal phase $BaCl_2$ nano-crystals start to dissolve, i.e. the hexagonal phase $BaCl_2$ volume fraction in the glass decreases.

Excitation and Fluorescence

Figure 4.13 shows the optical density of the 5 mol% Nd^{3+}-doped FZ sample. The material has strong Nd^{3+} absorption at 578, 742, and 797 nm and very weak absorption at 427, 625, and 679 nm. Additional small absorption bands can be found at 469 and 427 nm. At other wavelengths the absorption strengths are intermediate and can observed at 867 nm and two bands are observable at

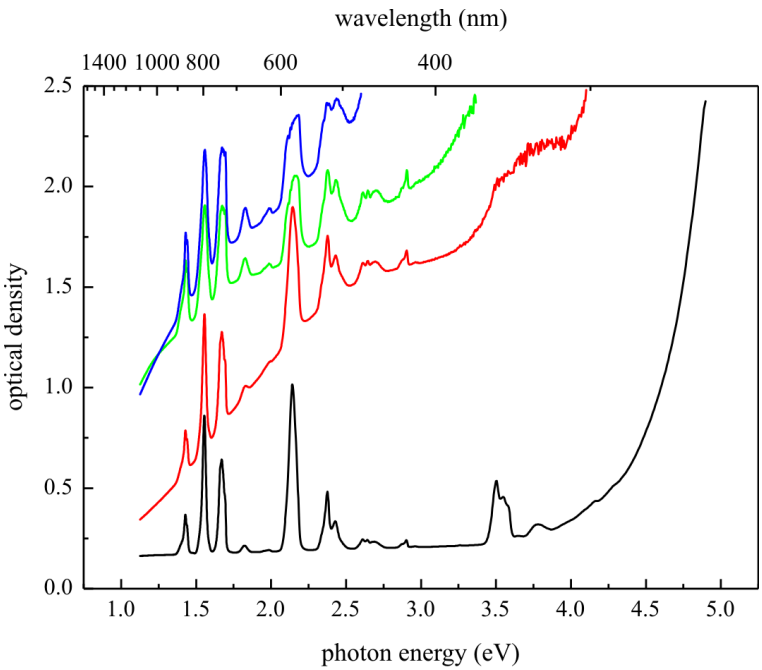

Figure 4.14: Optical density of four Nd^{3+}-doped FCZ glass samples. The sample thicknesses were 1 mm each. The measurements for the as-made glass (black) and these annealed at 250 °C (red), 270 °C (green), and 290 °C (blue) are shown.

$\sim$ 521 and 353 nm. The absorption bands are in good agreement with literature [30, 58, 59] and the energy level diagram of trivalent neodymium (see figure 4.5). The energy levels to which the trivalent Nd is excited due to the absorptions [30] are indicated in the diagram. In addition to the observed Nd^{3+} absorption bands, the material shows some background absorption in the UV spectral range below 300 nm. The inset in the upper right area shows the absorption bands in the NIR spectral range in more detail. The up-conversion experiments were carried using the absorption bands at $\sim$ 797 nm. The CW laser diode used has an excitation wavelength of 796 nm and is in resonance with the transition from the $^4F_{5/2}$ ground state to the $^4F_{3/2}$ excited state. The relatively high optical density is caused by the sample thickness being $\sim$ 1 mm and cords in the glass. Figure 4.14 shows the optical density of the as-made and three annealed glasses. The black curve is from the as-made glass already shown in figure 4.13. The colored curves are the measurements of the annealed glass ceramics: the red one is annealed at 250 °C, the green one at 270 °C, and the blue one at 290 °C, respectively; the higher annealing temperature corresponds to higher optical density. The increase in the optical density is stronger for higher photon energies, e.g. for the UV and blue spectral range. This is affected by scattering effects of the nanoparticles; growing with the annealing temperature.

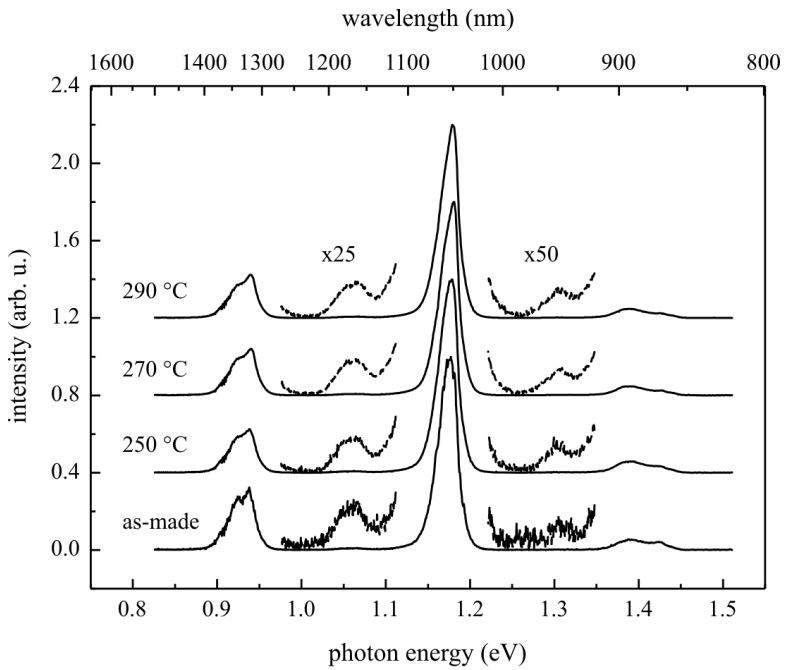

Figure 4.15: Fluorescence spectra for 5 mol% Nd-doped FCZ glass ceramics. From bottom to top: as-made and annealed at 250, 270, and 290 °C for 20 minutes. The spectra were blown up by 25 and 50 (dashed curves) for the low intensity emissions at 950 and 1165 nm, respectively.

Figure 4.15 shows the infrared fluorescence spectrum of different 5 mol% Nd-doped FCZ glass samples: as-made, annealed at 250, 270, and 290 °C for 20 minutes. The excitation was carried out in resonance with the $^4I_{9/2} \rightarrow {}^4F_{5/2}$ transition of Nd^{3+}. All samples show three main emission bands peaking at 885, 1060, and 1340 nm which can be assigned to transitions from the $^4F_{3/2}$ excited state to the $^4I_{9/2}$, $^4I_{11/2}$, and $^4I_{13/2}$ ground state of Nd^{3+}, respectively. The expanded IR emission spectra of the samples (see figure 4.15 dashed curves, expanded by a factor of 25 and 50) clearly show additional emission bands between the three main emissions at approximately 950 and 1165 nm. These are probably caused by $^4F_{5/2}$ to $^4I_{11/2}$ and $^4F_{5/2}$ to $^4I_{13/2}$ transitions, respectively. The experimental resolution for the fluorescence measurements was 0.2 nm.

The corresponding excitation spectra (see figure 4.16), were recorded (a) at 1060 nm for the $^4F_{3/2} \rightarrow {}^4I_{11/2}$ transition, and (b) for the $^4F_{3/2} \rightarrow {}^4I_{9/2}$ transition at 880 nm. The relative intensity ratio as well as the shape of the excitation bands are nearly identic for the spectra detected at 1060 and at 880 nm with one exception; an additional excitation peak at 703 nm in the spectrum detected at 1060 nm. The energy of this emission is equal to the energy difference of the $^4I_{11/2} \rightarrow {}^2H_{11/2}$ transition. Both spectra of the Nd^{3+}-doped samples show numerous excitation bands over the whole visible and in the ultraviolet spectral range. Note, that for wavelengths longer than approximately 820 nm, scattered excitation light starts to enter the spectra detected at 880 nm.

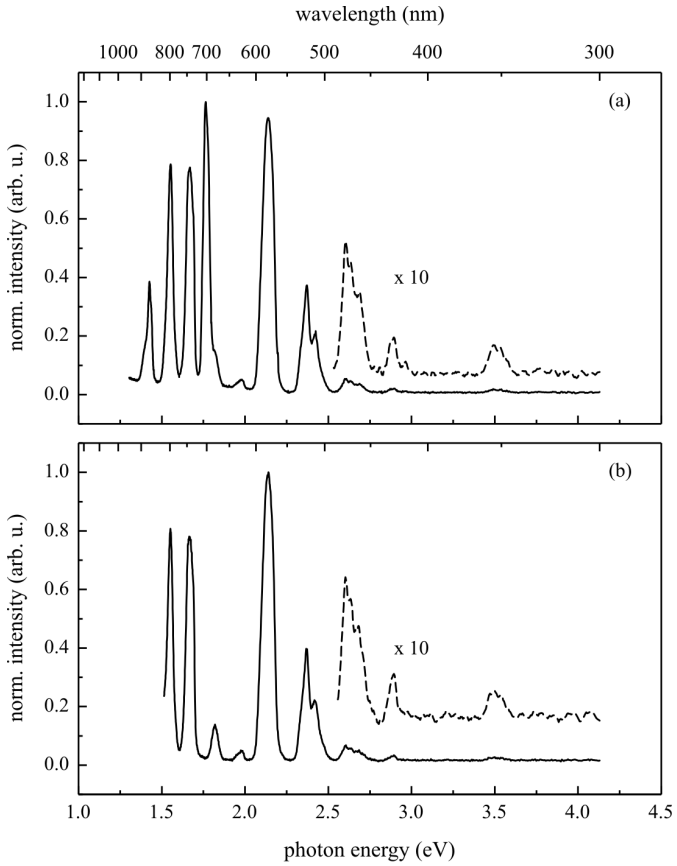

Figure 4.16: Excitation spectra of the Nd^{3+}-doped FCZ glass. The emission was detected at (a) 880 nm and (b) at 1060 nm, respectively. The dashed curves show the measurements in the range below 500 nm and are expanded a factor of ten. Both spectra were normalized to their most intense emission.

In figure 4.17 the measurements of the excitation spectra of the as-made glass and the annealed glass ceramics in the spectral range from around 400 to 820 nm are shown. For the sake of clarity the measurements of the annealed samples are not shown as excitation spectra, but the difference between the measurements of the as-made glass and the annealed samples are displayed. The dashed lines mark the most intense emission lines. At these position the difference curves show a double peak structure. This means that the excitation peaks have a broadening effect and a larger FWHM due to the thermal treatment whereas the maximum intensity of the excitation peak only grows slightly. Whereas annealed samples with annealing temperatures of 250 °C and above show about the same in intensity, shape and spectral position the glass ceramic annealed at 240 °C shows no significant difference compared to the as-made sample. The enhancement of the FWHM of the 579 nm excitation peak compared between the as-made and annealed samples versus the annealing temperature is shown in table 4.2. The values are are given to an accuracy of 0.1 and the enhancement factor has a calculated error of $\sim \pm 0.5$ %.

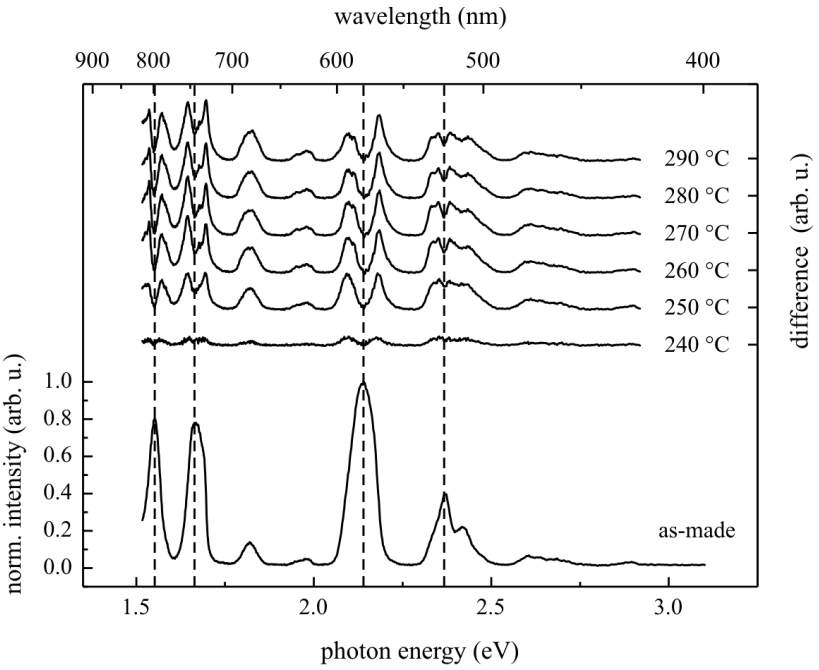

Figure 4.17: Excitation spectra of the 5 mol% Nd^{3+}-doped FCZ glass and annealed glass ceramics. The emission was detected at 880 nm. The spectrum of the as-made and the differences between this and that of the annealed samples are shown. The dashed lines mark the intense emission peaks.

annealing temperature (°C)	FWHM (nm)	enhancement (%)
as-made	22.1	-
240	22.9	3.6
250	26.5	19.9
260	26.6	20.5
270	26.5	20.1
280	26.4	19.2
290	26.4	19.3

Table 4.2: Enhancement factor of the FWHM of the 579 nm excitation listed after annealing temperature. The FWHM was approximated to one position after decimal point for this table. The enhancement factor has an error of ± 0.5 %.

Converted Fluorescence

Up-converted fluorescence in the visible and in the ultraviolet range was observed under excitation at 796 nm in resonance with the $^4I_{9/2} \rightarrow {}^4F_{5/2}$ transition of Nd^{3+}. The recorded spectra for the as-made and annealed samples at 250, 270, and 290 °C are shown in figure 4.18. The spectra are shown in the range of 340 - 750 nm and were normalized to their most intense emission at 590 nm. The spectral behavior at $\sim$ 750 nm is not shown, because scattered excitation light enters the spectrum. The most intense emission bands in the visible region are located in the green (530 nm), yellow (590 nm), and red (660 nm). They arise from the ^4G multiplets which, comprised of the $^4G_{9/2}$, $^4G_{7/2}$, and $^4G_{5/2}$ states, produce overlapping emission bands, and are therefore the strongest in the spectrum [58]. The ^4G multiplets are energetically accessible with two 796 nm photons. The two up-converted bands in the ultraviolet region at about 360 and 385 nm correspond to transitions from the $^4D_{3/2}$ excited state to the $^4I_{9/2}$ and $^4I_{11/2}$ ground state, respectively [58]. The $^4D_{3/2}$ level is only accessible with three 796 nm photons. The up-converted fluorescence spectra change their shape and relative intensities upon annealing. For annealing temperatures of 250 °C and above the UV emissions become stronger; they reach a maximum for the 270 °C annealed sample and then decrease slightly. All up-converted emissions show a splitting after annealing.

Crystal Field Splitting

For a more detailed examination of this effect, a comparison for the three emissions in the green and blue spectral range between the as-made sample and the sample annealed at 270 °C is given in figure 4.19. The intensities and offsets of the curves are plotted as in figure 4.18. The spectra were recorded with the same spectral resolution. The left curves shows the emission band at 530 nm in the green belonging to the $^4G_{7/2} \rightarrow {}^4I_{9/2}$ transition. The two emissions in the blue range are the $^2P_{1/2} \rightarrow {}^4I_{9/2}$ (435 nm) and $^2P_{3/2} \rightarrow {}^4I_{11/2}$ (413 nm) transition. The as-made sample shows emission bands without an explicit substructure. Upon annealing the up-converted emission bands splits. With higher annealing temperatures the splitting of the emission becomes stronger. The strongest observable splitting shows the 270 °C annealed sample. For the 2 samples annealed at higher temperatures, 280 and 290 °C, the splitting decreases instead of becoming stronger. Additionally, a change in the intensities of the up-converted emission can be observed for the emissions in the blue and ultraviolet spectral range. These transition can only be reached by subsequently absorbing three 796 nm photons.

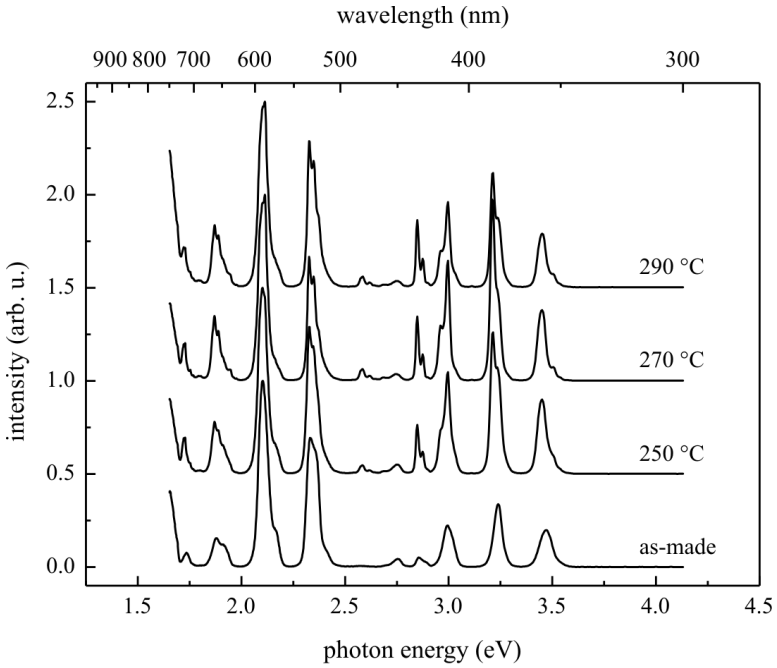

Figure 4.18: Normalized up-converted fluorescence spectra of 5 mol% Nd^{3+}-doped ZBLAN glass ceramics under CW infrared laser excitation at 796 nm. The spectra for the as-made and three annealed glasses are shown. For clarity the curves were plotted with an offset.

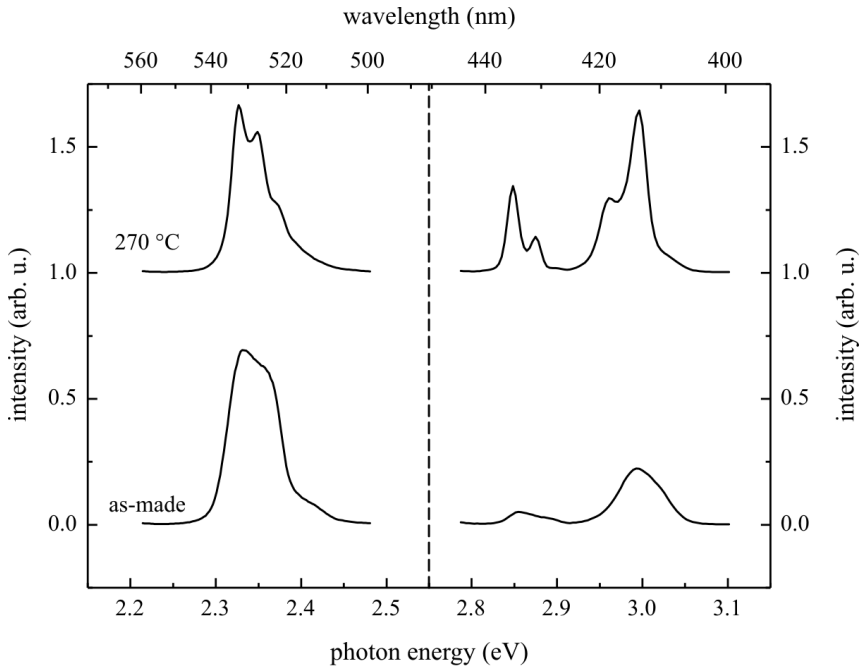

Figure 4.19: Up-converted emission spectra of the 530 nm ($^4G_{7/2} \rightarrow {}^4I_{9/2}$) emission, 435 nm ($^2P_{1/2} \rightarrow {}^4I_{9/2}$), and the 413 nm emission ($^2P_{3/2} \rightarrow {}^4I_{11/2}$) are shown for the as-made and the 270 °C annealed sample.

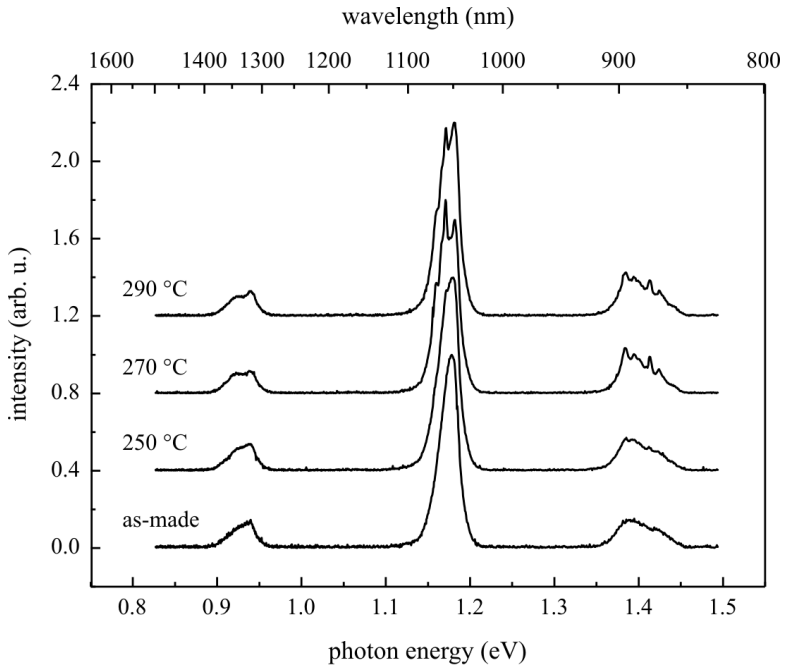

Figure 4.20: Fluorescence spectra for 5 mol% Nd-doped FCZ glass ceramics. From bottom to top: as-made and annealed at 250, 270, and 290 °C for 20 minutes. The excitation was carried out with a LD at 811 nm.

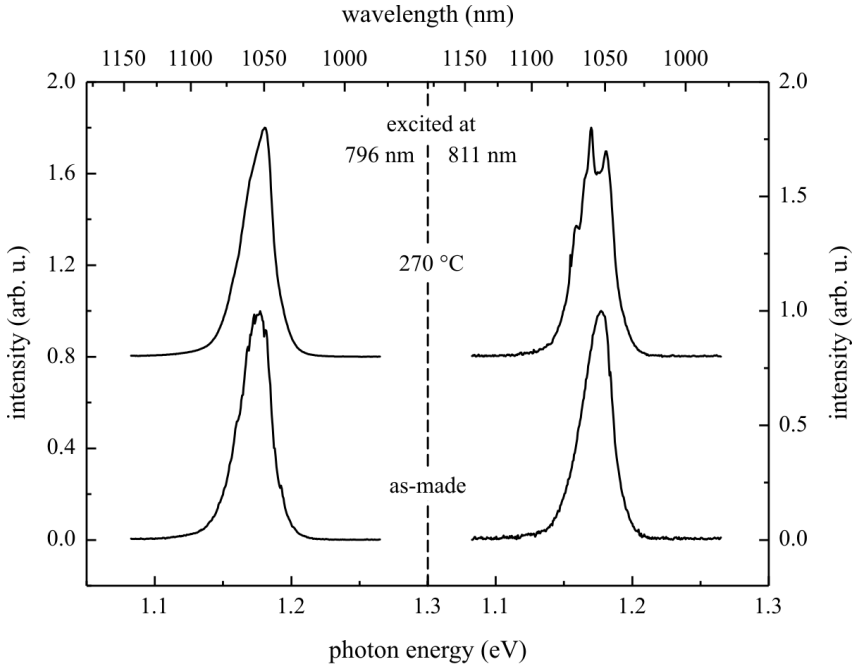

Figure 4.21: Comparison of the IR emission spectra of Nd-doped FCZ glass ceramics. The spectra for the as-made and 270 °C annealed sample are shown. The excitation for the left spectra was a LD emitting at 796 nm, on the right at 811 nm.

Additional measurements of the IR emission spectra were performed. Another CW laser diode with $\lambda = 811$ nm was used to excite the 5 mol% Nd-doped samples this time. In figure 4.20 the IR emission spectra in the range between 830 and 1500 nm are shown for the as-made and three annealed samples. The observed emissions can be attributed to the transitions between the energy levels of the trivalent Nd. For the annealed sample a splitting of the emission bands is observed. The intense emission at 1050 nm shows a splitting into a substructure of three noticeable peaks superimposed on the main emission from the as-made glass. For an annealing temperatures of 270 °C the splitting is a maximum; for temperatures above 270 °C the splitting reduces again. The relatively broad emission band between 850 and 900 nm ($^4F_{3/2} \rightarrow {}^4I_{9/2}$) shows a similar behavior; it splits into 5 smaller peaks. The lowest emission band at $\sim$ 1350 nm does not shows such a splitting effect.

Figure 4.21 shows the most intense IR emission of trivalent Nd for the as-made glass (bottom) and the 270 °C annealed glass ceramics (top) excited at 796 nm (left) and 811 nm (right). The spectrum of the as-made sample excited at 796 nm is identical in shape and spectral position within the experimental error to the spectrum excited at 811 nm. The 270 °C annealed sample shows different spectra upon the two excitations. The spectrum excited at 796 nm is the same as the spectra of the as-made sample. However, the spectrum of the 270 °C annealed sample excited at 811 nm shows a strong splitting in the emission band. The emission splitting is similar to those seen in the Nd-doped $BaCl_2$ single crystals. From this it can be assumed that the 270 °C annealed sample contains Nd ions both in the glass matrix and in the particles.

For deeper understanding of the crystal field splitting further temperature depended measurements were made. The IR emission spectra of an annealed sample of the 5 mol% Nd-doped FCZ glass ceramics were measured at temperatures between 20 and 290 K. Figure 4.22 (a) shows four of the measured emission spectra in the range between 860 and 920 nm. These measurements had to be performed with a PMT instead of a germanium detector due to the experimental setup for low temperature measurements. The shape of the observed emission changes due to the different spectral responses of the detectors. In (b) the emission spectra were plotted versus the temperature in the range between 20 and 290 K and 855 to 920 nm. All spectra were normalized to their most intense emission at 901 nm. It can be see, that the emission spectrum at 20 K is relatively simple and shows three strong peaks. A shoulder on the lower wavelength side can be observed. At higher temperatures the three clear emission peaks spectrum broaden with a few minor peaks superimposed.

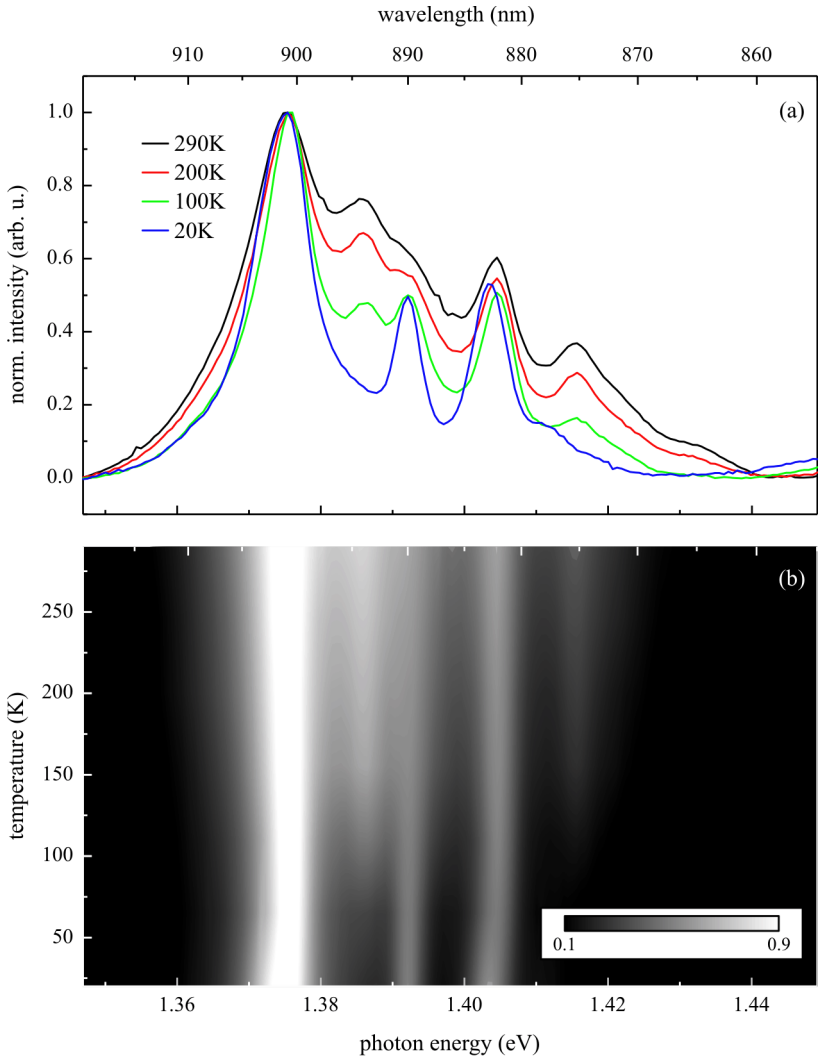

Figure 4.22: (a) shows four IR emissions at around 880 nm according to the $^4F_{3/2} \rightarrow {}^4I_{9/2}$ transition for temperatures from 20 to 290 K. The spectra were measured at the temperatures indicated. (b) is a contour plot containing all temperature depending IR emission measurements.

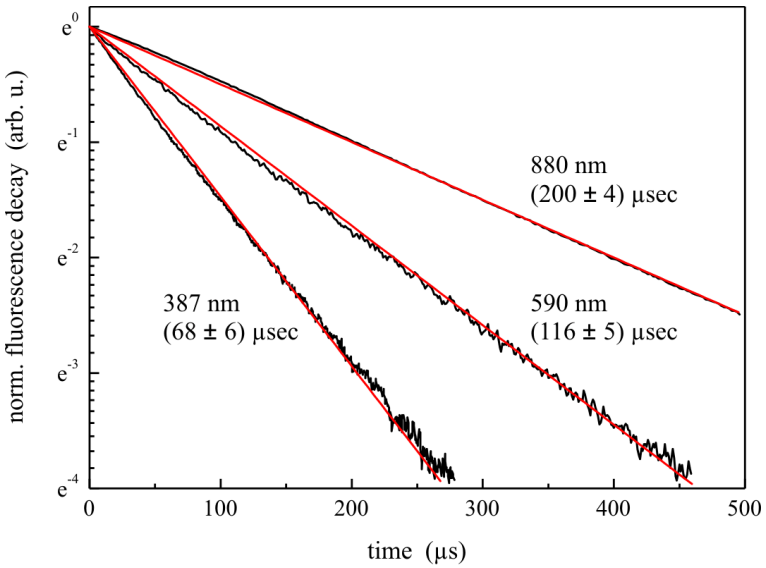

Figure 4.23: Normalized fluorescence decay of Nd^{3+} in the 270 °C annealed FCZ glass ceramic in a logarithmic plot. The fluorescence was detected for normal fluorescence (880 nm) and up-converted fluorescence (590 and 387 nm) as indicated and was excited at 796 nm with an infrared laser diode in resonance with the $^4I_{9/2} \rightarrow {}^4F_{5/2}$ transition of trivalent Nd. The measurements were fitted (red lines) with linear function.

Lifetime Measurements

Figure 4.23 shows the normalized fluorescence decay of Nd^{3+} in the 270 °C annealed FCZ sample. The Nd^{3+} decay was recorded for the infrared fluorescence at 880 nm, the yellow, 2-photon up-converted fluorescence at 590 nm, and the ultraviolet, 3-photon up-converted fluorescence at 387 nm. The lifetime of the 880 nm infrared fluorescence is (200 $\pm$4) μs, that of the 2-photon up-converted fluorescence (116 $\pm$5) μs, and that of the 3-photon up-converted fluorescence (68 $\pm$6) μs. As was already stated in section 2.1.2, of particular importance to the up-conversion efficiency is the intermediate energy level lifetime, specifically for the 2-photon up-conversion processes the energy level lifetime of the $^4F_{3/2}$ level is important. Figure 4.24 shows that the lifetime of the $^4F_{3/2}$ to $^4I_{9/2}$ (880 nm) and that of the $^4G_{7/2} \rightarrow {}^4I_{9/2}$ (593 nm) transition depends significantly on the annealing temperature. The longest lifetime of the intermediate energy level $^4F_{3/2}$ was found to be for the 260 °C sample with (204 $\pm$4) μs. By annealing the samples at higher temperatures the lifetimes of the intermediate level decrease again. The up-converted fluorescence lifetime of the $^4G_{7/2}$ energy level is dependent on the annealing temperature and obtains the longest lifetime of (123 $\pm$5) μs for the sample which was annealed at 280 °C for 20 minutes. It seems that the energy levels are all slightly different effected by the changing crystal field upon the annealing process. This could led to the different annealing temperatures for the maximum fluorescence and up-converted fluorescence lifetimes.

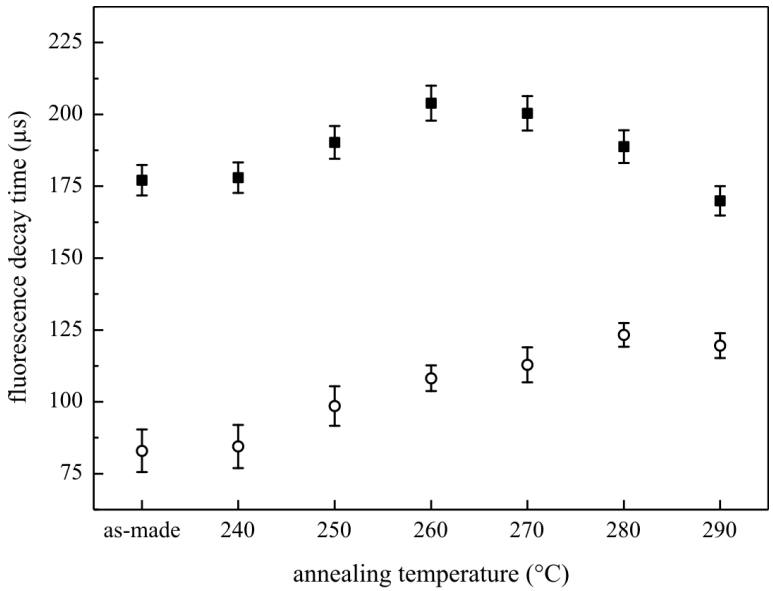

Figure 4.24: Fluorescence (880 nm, black squares) and up-converted fluorescence (590 nm, open circles) decay time of Nd^{3+} doped samples is shown vs. annealing temperature.

Power Dependence

Figure 4.25 shows the dependence of the emission intensity on the 796 nm excitation power for the infrared fluorescence band at 880 nm corresponding to the $^4F_{3/2} \rightarrow {}^4I_{9/2}$ transition and the most intense up-converted fluorescence band at 590 nm, which arises from transitions of the ^4G multiplets to the ground states. The three-photon-up-conversion emission at 385 nm ($^4D_{3/2} \rightarrow {}^4I_{11/2}$) is also plotted. The power dependence was measured by inserting different optical filters (e.g. neutral density filters) in the pump beam. Fluorescence spectra were recorded over several orders of magnitude of excitation power, e.g. from approximately 130 mW (maximal laser diode output power) down to a few μW. For the emission at 880 nm, the slope is 1.00 with a confidence level of almost one, e.g. an almost perfect linear dependence on the excitation power. Up-conversion spectra of the 590 nm emission were recorded for excitation powers in the range from 130 mW down to less than 2 mW. For lower excitation powers the signal to noise ratio was too low for an exact analysis. For the two photon up-converted fluorescence emission, the slope is 1.87. The three photon up-conversion was measured in an excitation range between 130 mW and 17 mW. At this level the signal to noise ratio becomes too low for further measurements. The slope can be determined as 2.76. Both up-conversion power dependencies show nor saturation effects neither a decrease of the fitted slope.

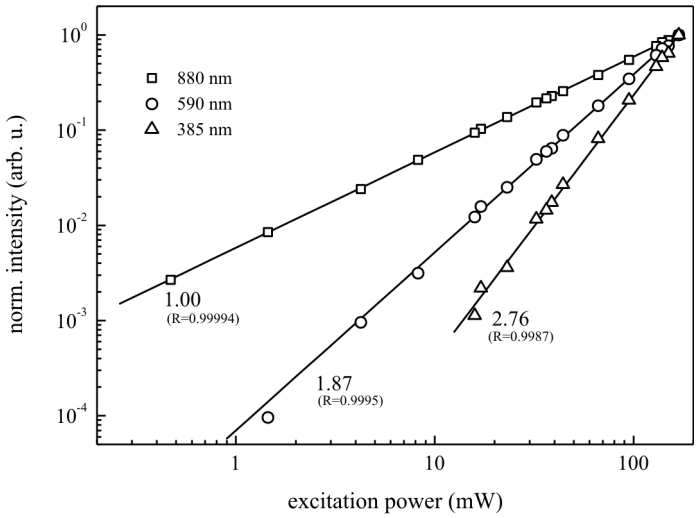

Figure 4.25: This figure shows the intensities of the PL, two- and three-photon-up-conversion versus excitation power. The intensities of the emissions are normalized to their intensity at 130 mW. The 880 nm PL are plotted as squares, the two photon-up-conversion at 590 nm as circles and the three-photon-up-conversion at 385 nm as triangles. The slope of the fits is indicated as well as the confidence level *R*.

Nd Doping Level Dependencies

After the optical and structural characterization of the 5 mol% Nd-doped FCZ glass ceramics the same measurements were performed on the 0.5 and 1 mol% doped glasses and glass ceramics. These sample were annealed after synthesis at the same temperatures as the 5 mol% doped sample. A picture of the samples is shown in figure 4.10, which depicts differences in the scattering effect when illuminated from the back. Due to the lower crystallization temperature of the $BaCl_2$ nanocrystalites for lower Nd doping concentrations (see figure 4.9) different crystallite sizes for the same annealing temperatures are expected. Prasad *et al.* [29] showed that the optical behavior and properties of optical active nanoparticles are critically effected by their size.

In figure 4.26 the emission intensity of the different annealed samples is plotted for the three Nd-doped FCZ glass ceramics. The intensity is given by the color; going from blue to red for higher intensities. The spectra were normalized to the integrated up-converted emission intensities to obtain better comparison. The spectral fraction of the normalized spectra are shown in figure 4.27. Here the percentage for the different spectral ranges to the whole up-converted emission spectrum are shown as a function of the annealing temperatures of the glass ceramic samples. The ranges are chosen with respect to the main emissions and are shown in table 4.3. From the three diagrams of figure 4.26 the same up-converted emissions of trivalent Nd can be observed.

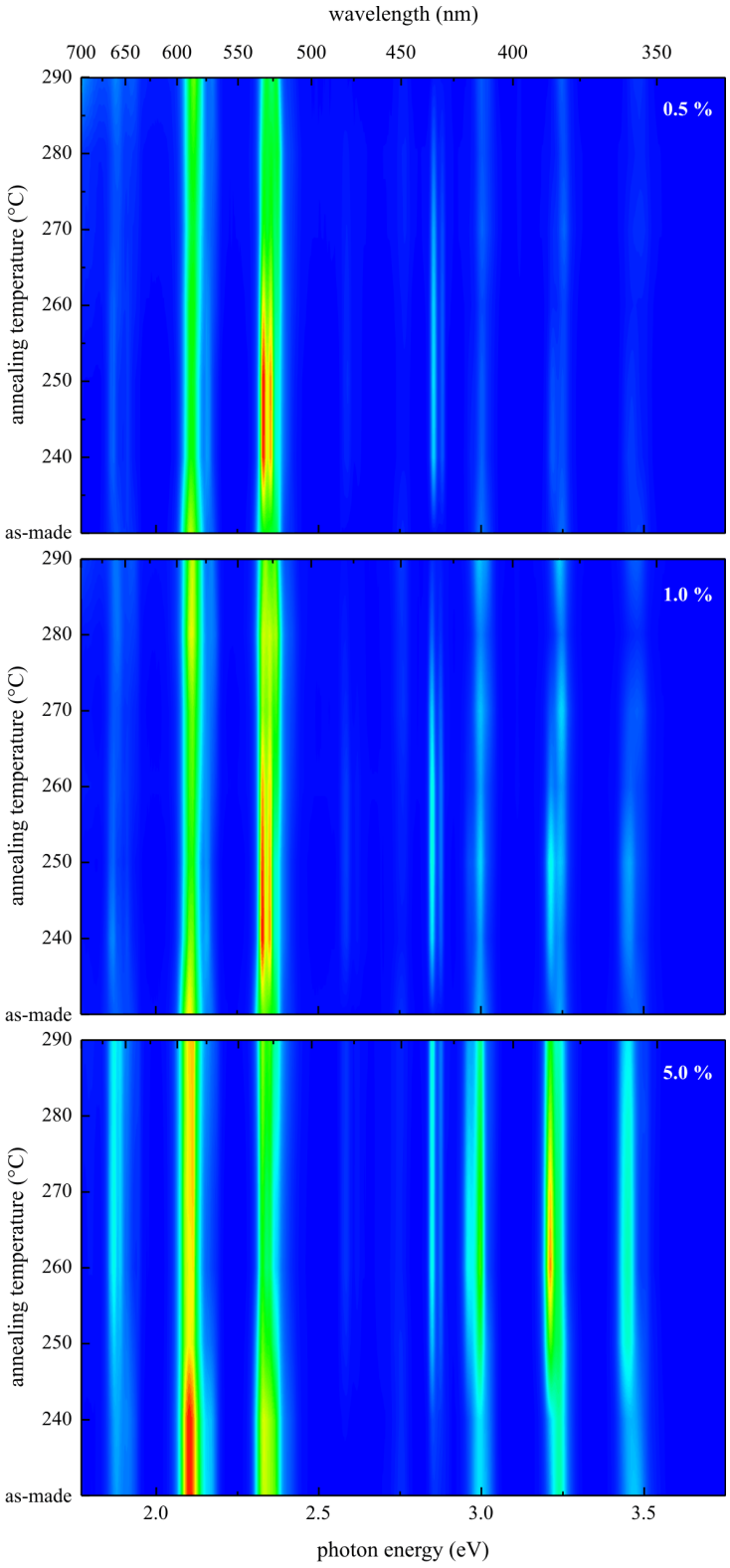

Figure 4.26: The spectral behavior of the normalized up-conversion intensity is plotted versus the annealing temperature. The three figures are from top to bottom: 0.5, 1.0, and 5.0 mol% Nd-doped FCZ glasses and glass ceramics. The intensities are given by the color; from blue to red for higher intensities.

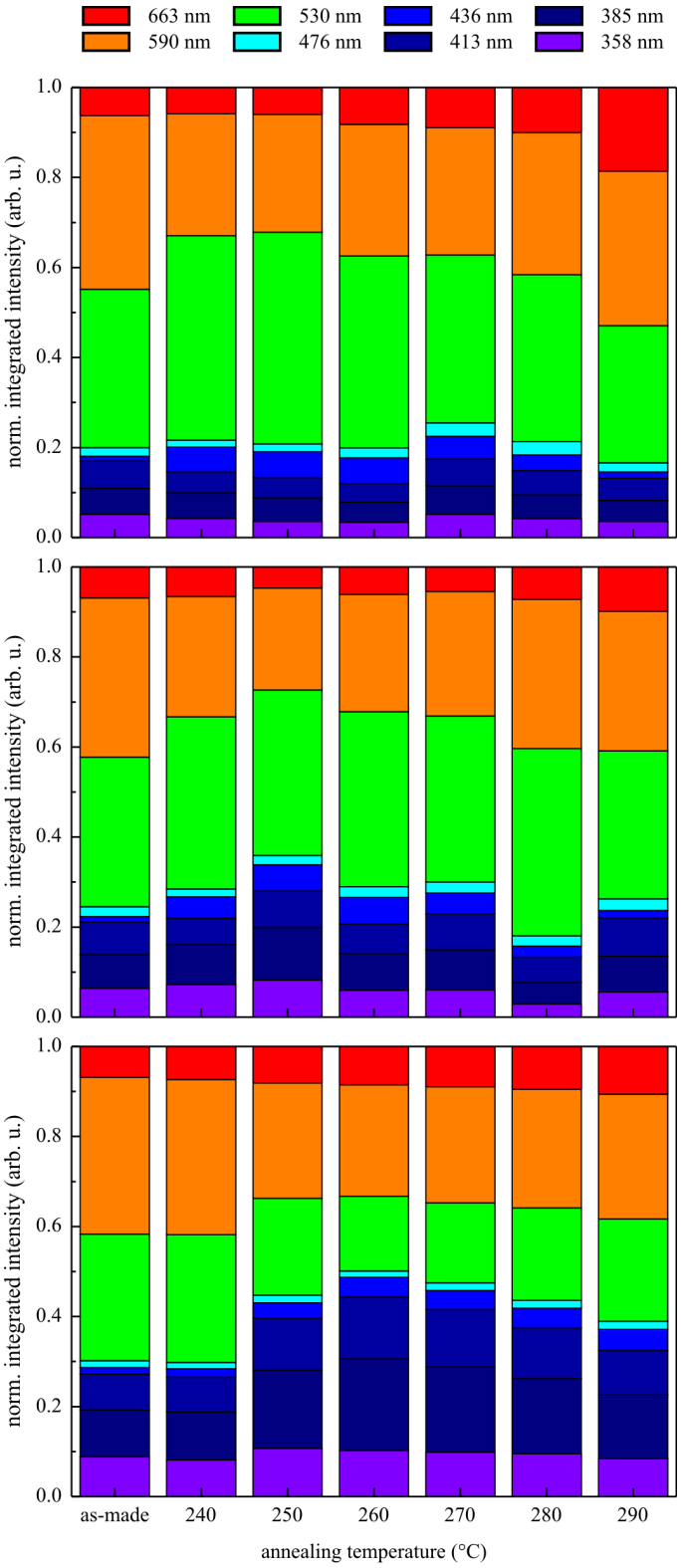

Figure 4.27: These figures show the percentage for the different spectral emission ranges to the whole integrated normalized up-converted emission spectra. The three diagrams are from top to bottom: 0.5, 1.0, and 5.0 mol% Nd-doped samples. The color indicates the chosen spectral range (see legend above and table 4.3).

number	range		emission(s)
	start (nm)	end (nm)	(nm)
1	339	370	359
2	370	400	385
3	400	425	413
4	425	443	436
5	436	477	450, 461
6	477	551	530
7	551	620	590
8	620	700	663

Table 4.3: List of chosen spectral ranges for up-converted emissions of Nd-doped FCZ glasses ceramics.

The blue and UV spectral emissions are relatively more intense the higher the neodymium doping. The two upper plots of the 0.5 and 1 mol% doped samples show conspicuous features when annealed at temperatures in the range of 240 to 260 °C. The intensities of the 530 nm emission rise up to nearly 50 % and 40 % of the integrated intensity for the 0.5 and the 1.0 mol% doped sample, respectively. In both samples is the orange-red spectral range the least intense. The emissions in the blue and UV spectral range contribute only a small part to the integrated intensity. The sum is almost constant at $\sim$ 20 % for the lowest doped samples and did not change significantly for higher annealing temperatures. The 1 mol% doped sample shows a slightly intensity which goes up when annealing up to 250 °C. After this maximum point the intensity decreases and ends up at $\sim$ 25 %. The spectra of the 5 mol% doped sample have already been shown in figure 4.18 where the spectrum was normalized to the strongest emission for that figure. Here it can be seen that the up-converted emissions in the blue and ultraviolet get stronger in comparison to the emissions in the green and red spectral range as annealing temperature increases. They reach a maximum of $\sim$ 50 % for annealing temperatures of $\sim$ 260 and 270 °C, and decrease slightly for temperatures up to 290 °C. Even the sample annealed at 290 °C shows a blue-UV emission of $\sim$ 40 %.

In figure 4.28 the infrared emission spectra of the different doped glasses is shown. The spectra of the as-made glasses were plotted with an offset to clarify the figure. All glasses show the typical trivalent Nd emissions. The three most intense emissions, all starting from the $^4F_{3/2}$ energy level, can be observed in all glasses with nearly the same intensities. Although the spectral positions of the emissions are identical within the experimental error. All emissions of the three spectra have the same shape. Only the emission corresponding to the $^4F_{3/2} \rightarrow {}^4I_{13/2}$ transition of the 1 mol% doped samples differs

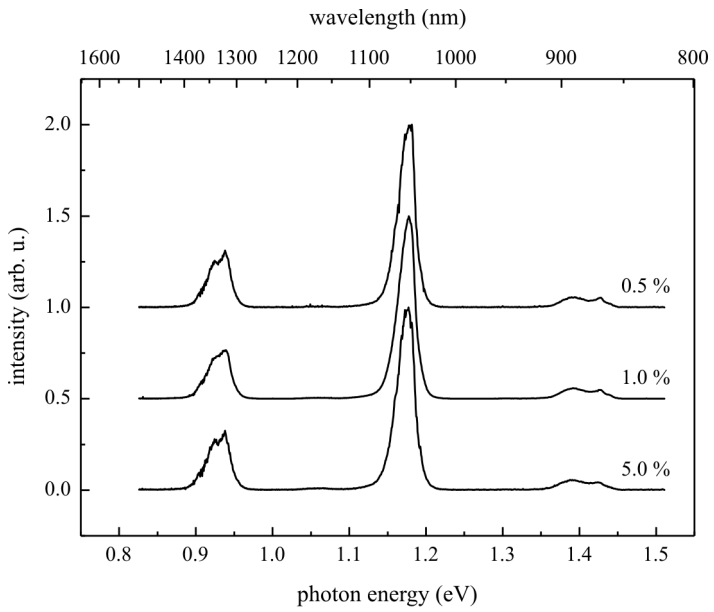

Figure 4.28: This figure shows the measured IR emission spectra of the three as-made glasses. From top to bottom the spectra of 0.5, 1, and 5 mol% Nd-doped FCZ glass ceramics are shown.

slightly in its shape from the others. The IR emission spectra of different temperature annealed glass ceramics are shown for the 5 mol% doped sample in figure 4.2. There is no significant change in their intensities, shapes, or emitting wavelengths. The same result is found for the emission spectra of the annealed samples of the 0.5 and 1 mol% doped glass ceramics. Therefore the spectra are not shown in this chapter but were added to the appendix. They are shown in figure A.3 on page 93.

The excitation spectra of the three (0.5, 1.0, and 5.0 mol%) Nd-doped glasses are shown in figure 4.29. Only the measured spectra from the as-made glasses are depicted here for comparison. The excitation spectra of the annealed sample can be found in the appendix (figure A.4, 0.5 and 1.0 mol% doped Nd^{3+}) and in figure 4.17 (5.0 mol% doped FCZ). The spectra are normalized to the most intense line at 579 nm corresponding to the $^4I_{9/2} \rightarrow {}^4G_{5/2}$ transition. No significant difference between the three as-made glasses can be observed. The excitation intensities as well as their spectral position and shape are nearly identical. Only the FWHM of some excitation peaks variy with the doping level; the higher the doping level the broader the FWHM of the peaks. In addition the excitation at around 741 nm increases from 0.67 up to 0.78 (normalized intensity) when raising the doping level from 0.5 up to 5.0 mol% Nd^{3+}.

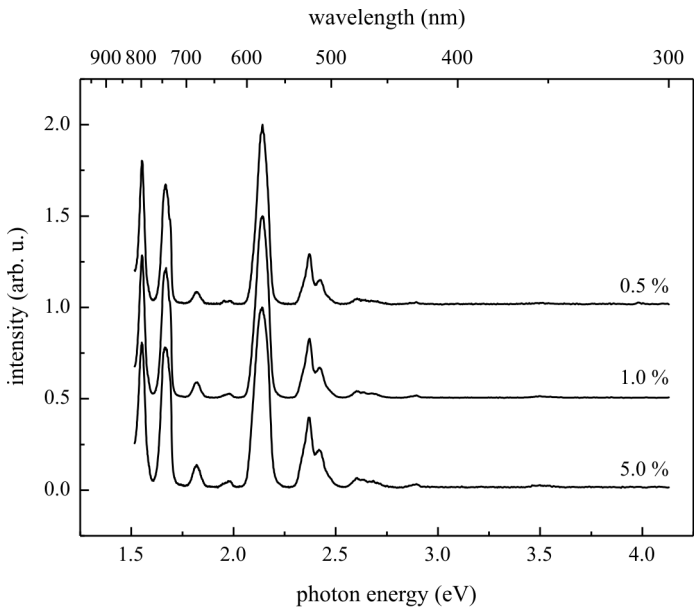

Figure 4.29: Measured excitation spectra of the three as-made glasses. From top to bottom the spectra of the following FCZ glasses are shown: 0.5, 1, and 5 mol% Nd-doped.

4.2.4 Discussion

Infrared fluorescence and up-converted fluorescence spectroscopy (figure 4.2 and 4.4) show that Nd^{3+}-ions can be incorporated into $BaCl_2$ single crystals and elucidates therein its characteristic optical properties, in particular, an up-conversion effect upon excitation with a laser diode operating at 796 nm. It is also possible to form hexagonal $BaCl_2$ nanoparticles (figure 4.11) in a Nd-doped ZBLAN glass matrix. Additionally, it was shown that Nd^{3+} ions enter these particles and leads to enhanced two and three photon up-conversion emissions in the visible and UV spectral range (see figure 4.30).

It was found that the glasses without additional chlorine doping show no crystallization peak (figure 4.9). Therefore the chlorine doping is essential to initiate crystallization of the particles in the glass. Additionally, the glass transition temperature as well as the crystallization peak shifts to higher temperatures for higher doping levels. Both effects are confirmed by a back illuminated picture of samples, shown in figure 4.10. Samples without chlorine show no scattering effects. The scattering effect gets stronger for less doped samples compared to samples with the same annealing temperature. Upon thermal processing, nanoparticles are formed in the glass; these can be identified as hexagonal phase $BaCl_2$. There is no phase transition observable as was found in Eu-doped [61, 62] or Ce-doped [63] FCZ glass ceramics. From analysis of measurements the particle size grows from a few tens up to about 150 nm and

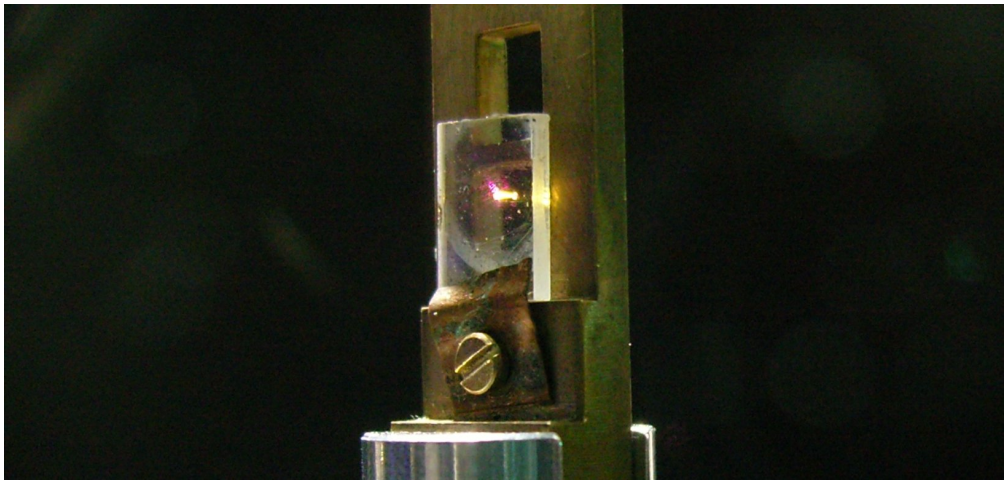

Figure 4.30: FCZ glass ceramic sample with its intense yellow-white up-converted fluorescence. The excitation is carried out with an IR laser diode operating at 796 nm.

their volume fraction (maximum at an annealing temperature of 270 °C) can be determined. The particle size determination by XRD has large errors for sizes of 100 nm and more. Transmission electron microscopy measurements should be a possibility to get more information on the particle size and size distribution. The appearance of a crystalline phase in the XRD patterns (see figure 4.11) after thermal processing can be correlated to crystallization peaks in the DSC data (plotted in figure 4.9).

The optical density increases (figure 4.14) due to the scattering effects from the larger particles precipitate for higher annealing temperatures. The infrared emission spectra show the characteristic Nd^{3+} emissions for all samples. The emissions show no significant change in their shape or intensity upon the annealing. The IR spectra of the glasses and glass ceramics are comparable with the spectra from the $BaCl_2$ single crystals (figure 4.2), whereas the single crystals show a crystal field splitting. In the excitation spectra (figure 4.17) the samples annealed at temperatures of 250 °C and above show a relative increase in the excitation bands in the UV and visible spectral range. The FWHM of some excitation bands becomes wider (table 4.2); an increase of 20.5 % was observed for the at 260 °C annealed and with 5 mol% Nd-doped sample. This effect could be useful for an up-conversion excitation with normal sunlight due to the possibility for absorbing a higher number of photons. The excitation spectra of the lower doped glasses (figure A.4) also show these spectral broadening effect.

The up-conversion spectra (figure 4.4 and 4.18) suggest that the most important excited states for up-conversion fluorescence are $^4D_{3/2}$, $^2P_{1/2}$, and the ^4G multiplets. The 796 nm photons are strongly absorbed and excite ions into the

$^4F_{5/2}$ level from which they relax non-radiatively to the relatively long lived $^4F_{3/2}$ level. The ^4G multiplets can be populated by excited state absorption (ESA) and/or energy transfer up-conversion (ETU). In the ESA process a second 796 nm photon excites the ion from the $^4F_{3/2}$ to $^2D_{5/2}$, for which there is a good energy match with 796 nm photons; this is followed by non-radiative relaxation into the $^2P_{1/2}$ level and into the various ^4G states. In the ETU process, each ion is separately excited into the $^4F_{3/2}$ state. From that level de-excitation of one ion can result in excitation of the other. The Nd level scheme provides a number of such possibilities (figure 4.5). Close energy matching is obtained with excitation from $^4F_{3/2}$ to $^4G_{9/2}$ accompanied by de-excitation to $^4I_{11/2}$ and also with excitation to $^4G_{7/2}$ and de-excitation to $^4I_{13/2}$. Excitation to the $^4D_{3/2}$ state clearly requires the energy of three 796 nm photons. However, it is difficult to identify the excitation mechanism without more detailed information on the energy levels beyond those depicted in the energy level diagram. An ESA process could occur in these higher levels from one of the ^4G levels, which are known to be significantly populated by 2-photon excitation followed by non-radiative relaxation. Alternatively an energy transfer mechanism could operate with an ion in a $^4G_{5/2}$ state interacting with a neighbor in a $^4F_{3/2}$ state, resulting in excitation of one ion to $^4D_{5/2}$ accompanied by de-excitation to $^4I_{9/2}$. The $^4D_{5/2}$ state would rapidly relax to populate $^4D_{3/2}$, giving rise to the observed emissions. The spectra of the up-converted emissions (see figure 4.18) suggest likewise that Nd^{3+} is incorporated in the nanoparticles during the annealing process. The emission intensities in the UV and blue spectral range increase upon annealing compared to the other up-converted emissions. The 5 mol% doped glass ceramics reaches a maximum at around 260 °C, whereas it is reached at lower temperatures for the lower doped glass series. Another effect of the annealing process is a splitting of the up-converted emission (figure 4.19) which is affected by the local crystal field [57]. The maximum splitting was found for the sample annealed at 270 °C. This sample had shown the highest volume fraction. The largest of the splitting effect is again at lower temperatures for lower doped glass ceramics; at 240 and 250 °C for the 0.5 and 1.0 mol% doped samples, respectively. Measurements with another laser diode operating at $\lambda_{em} = 811$ nm for excitation lead to Nd^{3+} infrared emission spectra (see figure 4.20) that show also such a crystal field splitting effect depending on the annealing temperature. These spectra show various similarities with the measured infrared emission spectra of the Nd-doped $BaCl_2$ single crystals; compare figure 4.20 with figure 4.2. From this it can also be assumed that upon annealing some of the Nd^{3+} ions enter the nanocrystals leading to a splitting of the infrared and up-converted fluorescence spectra.

As already stated in the section 2.1.2, of particular importance to the up-conversion efficiency is the intermediate energy level lifetime, specifically for two-photon up-conversion processes the energy level lifetime of the $^4F_{3/2}$ level is important. Lifetime measurements have been performed (see figure 4.7 and figure 4.24) for fluorescence (880 nm) and up-converted fluorescence (593 nm). For both cases the lower doped single crystal has a longer lifetime. It is assumed that quenching effects decrease the fluorescence lifetime due to non-radiative energy transfer between neighboring Nd^{3+} ions. The measurements on the glass ceramics show a significant dependency on the annealing temperature. The longest lifetime of around 204 μs for this level was found for the sample annealed at 260 °C; leading to an enhancement of 15.1 % when compared to the lifetime (177 μs) of the as-made glass sample. The energy levels are affected slightly differently by the changing crystal field upon annealing. Due to this effect the maximum fluorescence and up-converted fluorescence lifetime were not measured for the same sample, but for glass ceramics annealed at 260 and 280 °C, respectively.

In principle, for low excitation powers a quadratic dependence of the two-photon up-converted fluorescence at 590 nm and a cubic dependence of the three-photon up-converted fluorescence on the excitation power is expected [15]. The power dependence of the Nd-doped single crystals shown in figure 4.8 yields, however, for the two-photon up-conversion exponents of 1.85 and 1.92 for 0.01 and 1 mol%, respectively. The power dependence of the two and three photon up-conversion in the glass ceramics shown in figure 4.25 yields exponents of 1.87 and 2.76, respectively whereas the normal PL shows a nearly perfect linear decay. This experimentally observed decrease is determined by the competition between linear decay and up-conversion processes for the depletion of the intermediate excited states. The shorter fluorescence lifetime for the higher doped $BaCl_2$ single crystal (figure 4.7), i.e. the faster depletion of the $^4F_{3/2}$ state leads to a larger slope in the up-converted intensity vs. excitation power dependence. The intensity of up-converted fluorescence that is excited by the sequential absorption of m photons has a dependence on absorbed excitation power P_{in}, which may range from P_{in}^m in the limit of infinitely small up-conversion rates down to P_{in}^1 for the upper state and less than P_{in}^1 for the intermediate states in the limit of infinitely large up-conversion rates (see table 2.2 and [15]). The fact that the deviation from $m = 2$ is small in the case of 0.01 and 1 mol% Nd^{3+}-doped $BaCl_2$ indicates that these systems are far away from the point where saturation effects will play a role. It is the same for the glass ceramics, with the fitted slopes of 1.85 (two photon up-conversion $m = 2$) and 2.76 (three photon up-conversion $m = 3$).

4.3 Dopant: Erbium

4.3.1 Motivation

In the last section Nd-doped glasses and glass ceramics were investigated for up-converting processes. These up-converting glass ceramics were produced as a model system for an up-converting back layer for bifacial solar cells. However, the Nd-doped glasses are not applicable as up-converters for silicon solar cells due to their excitation wavelength being around 800 nm. Since this light can be absorbed by the solar cell itself, the dopant was changed from neodymium to erbium as the energy levels of Er^{3+} have an absorption band at $\sim$ 1540 nm. Therefore erbium as dopant is much more suitable for up-converting backlayers for silicon solar cells. Additionally, excitation with 800 nm photons is also possible.

4.3.2 Fluorozirconate Glasses

As mentioned in the last section the ZBLAN glass system is an ideal host for optically active rare earth ions. In addition to the low phonon frequencies the ZBLAN glasses offer optimal transparency over a wide spectral range. Emission and excitation bands of embedded Er^{3+} ions are neither influenced nor absorbed by the glass. The composition of the erbium doped glasses are given in table 4.4.

Differential Scanning Calorimetry

All glasses are based on the well known ZBLAN composition [21]. For the 2 and 5 mol% doped samples, the ErF_3-doping was done at the expense of ZrF_4. These glasses are comprised of $(53-x)$·ZrF_4-20·BaF_2-20·NaCl-3.5·LaF_3-3·AlF_3-0.5·InF_3-x·ErF_3, where $x = 2$ or 5 (values in mol%). For 9.1 and 13 mol% doping, the adding of ErF_3 is compensated by reducing all other components proportionally. The DSC data of these fluorozirconate based glasses are shown in figure 4.31. The DSC data for the 2% Er-doped FZ glass has a glass transition

sample	ZrF_4	BaF_2	LaF_3	AlF_3	NaF	InF_3	ErF_3
ZBLAN JJ33	51.0	20.0	3.5	3.0	20.0	0.5	2.0
ZBLAN JJ34	48.0	20.0	3.5	3.0	20.0	0.5	5.0
ZBLAN JJ54	48.2	18.2	3.2	2.7	18.2	0.5	9.1
ZBLAN JJ57	46.1	17.4	3.0	2.6	17.4	0.4	13.0

Table 4.4: Composition of ErF_3 FZ glasses in mole percent. The name of the samples is a composition of the abbreviation ZBLAN given by the compounds of the FZ glasses ([21]) and an inventory number.

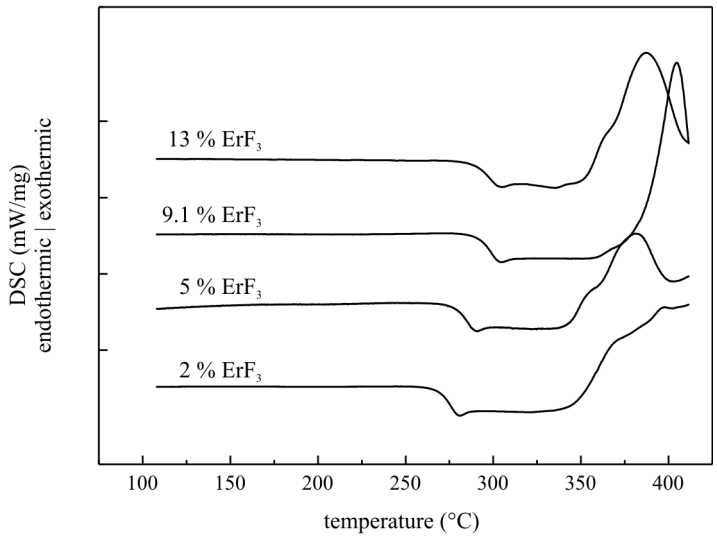

Figure 4.31: DSC data of Er-doped FZ glasses. From bottom to top: The samples contain 2, 5, 9.1, and 13 mol% ErF_3.

temperature (T_g) of (267.5 $\pm$0.3) °C which is slightly higher than that observed for pure FZ glass [21, 60]. No crystallization peaks can be found upon doping the fluorozirconate glass with Er. However, crystallization is only initiated if the glass is additionally doped with chlorine ions. Increasing the ErF_3 in the FZ base glass the glass transition temperature shifts up to $\sim$290 °C for the 13% doped glass which is significantly higher than that for the lower Er-doped FZ glass. An exothermic peak can be observed at temperatures of 380 to 400 °C. This also appears in the from pure FZ glass spectrum where the main glass crystallization starts at $\sim$350 °C [21]. In table 4.5 the glass transition temperature is given for the ErF_3-doped glasses. The T_g from literature was added to the table for the undoped FZ glass. The measurements show higher glass transition temperatures for higher ErF_3 doping levels. For doping concentrations of 9 mol% ErF_3 and more the glass transition temperature saturates at $\sim$ 290 °C.

sample	doping level (%)	T_g (°C)
ZBLAN [21, 60]	0	262.0
ZBLAN JJ33	2.0	267.5
ZBLAN JJ34	5.0	274.8
ZBLAN JJ54	9.1	289.6
ZBLAN JJ57	13.0	289.5

Table 4.5: The table shows the glass transition temperatures of the different ErF_3-doped FZ glasses. The data for the undoped FZ glass was taken from literature [21, 60].

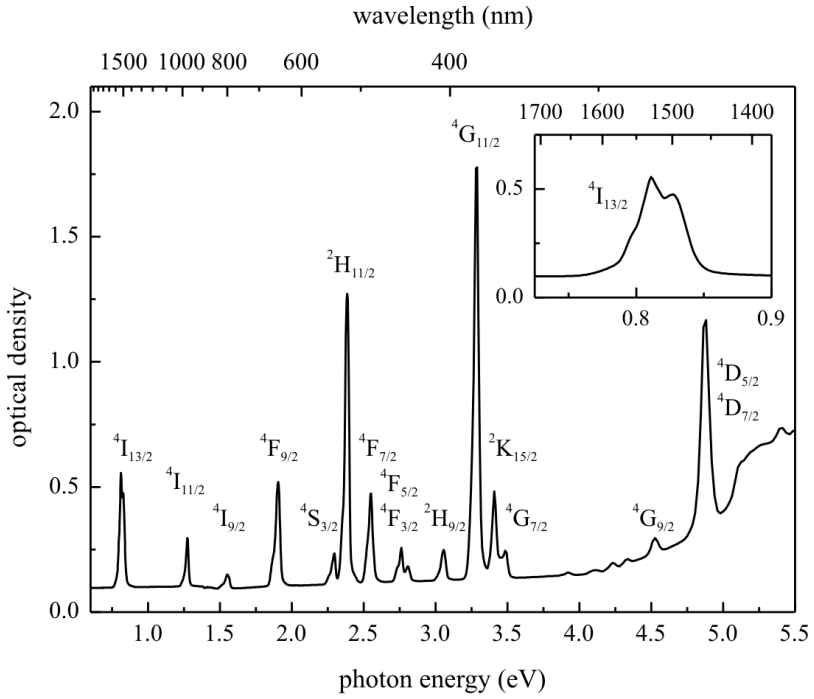

Figure 4.32: Optical density of the 5 mol% Er^{3+}-doped FZ glass sample. The labeled transitions start from the $^4I_{15/2}$ ground state level and end on the levels indicated. The sample thickness was 2.2 mm. The inset shows a closer look on the lowest absorption band in the IR spectral range.

Excitation

Figure 4.32 shows the optical density of the 5 mol% Er^{3+}-doped FZ sample. The material has strong Er^{3+} absorption at 254, 377, and 520 nm and very weak absorption at 229, 274, and 800 nm. At other wavelengths the absorption strengths are intermediate. The absorption bands are in good agreement with the literature [64] and the energy level diagram of trivalent erbium (see figure 4.33). The energy levels of the trivalent Er affecting the absorption ([30]) are indicated in the graph. In addition to the observed Er^{3+} absorption bands, the material shows some background absorption in the UV spectral range below 300 nm. The inset in the upper right shows the lowest absorption band in more detail. The up-conversion experiments were carried out by an excitation into this. The CW laser diode is operating at a wavelength of 1540 nm and thus is in good resonance with the transition from the $^4I_{15/2}$ ground state to the $^4I_{13/2}$ excited state. The relatively high optical density is due to the sample thickness of about 2.2 mm.

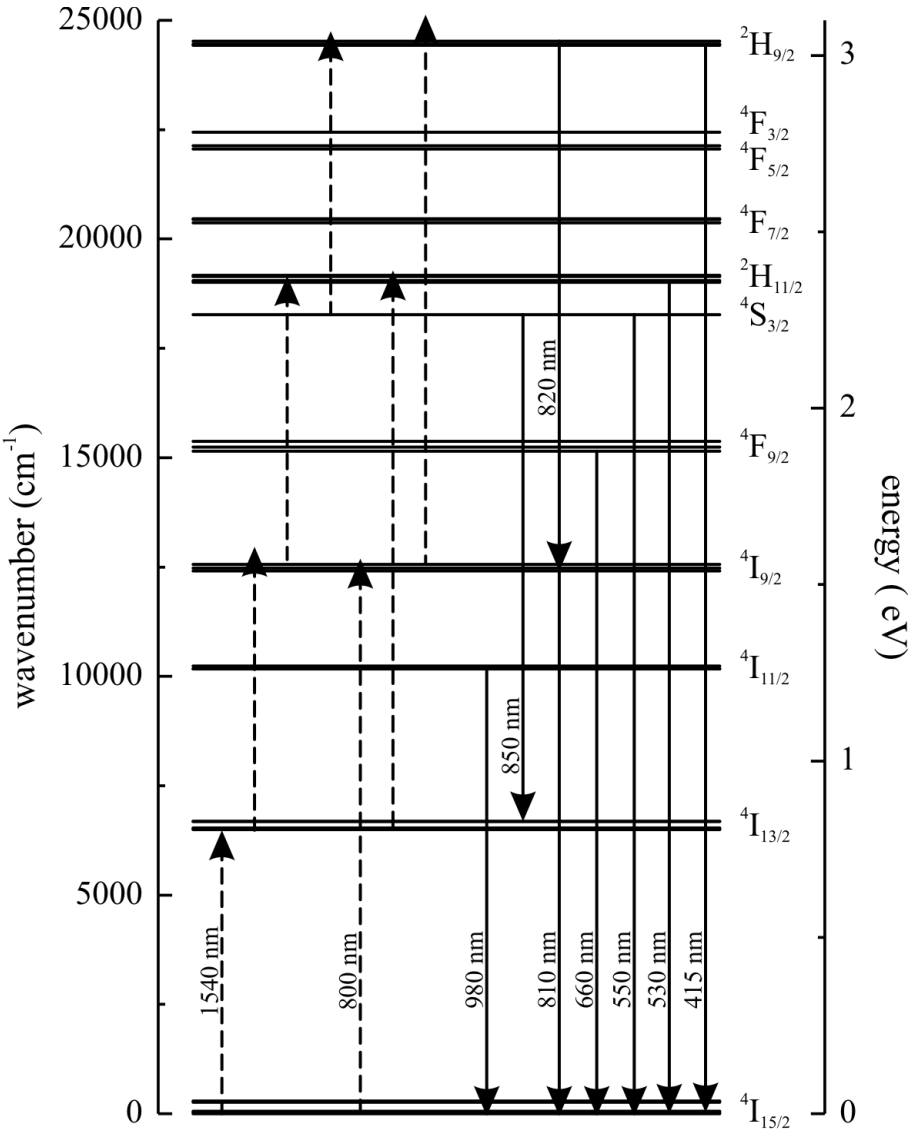

Figure 4.33: Energy level diagram of trivalent Er in FZ glasses: Up-conversion emissions (solid arrows) and possible up-conversion routes (dashed arrows) for excitation at 1540 (left) and at about 800 nm (right) are indicated.

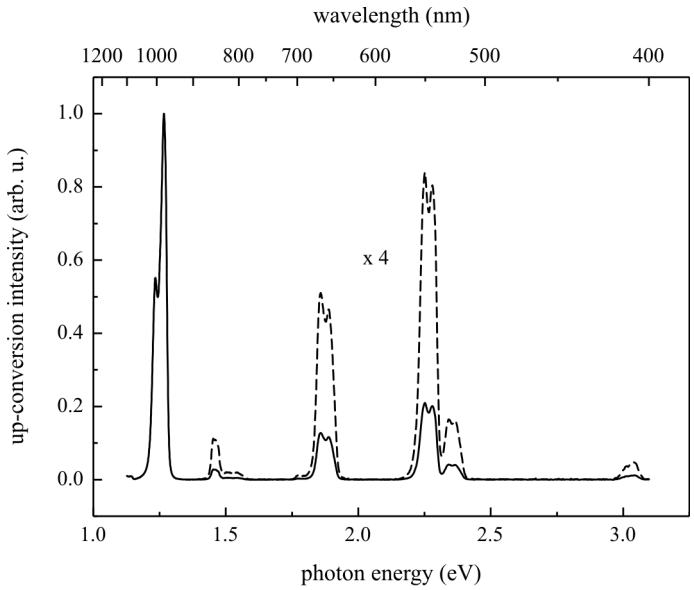

Figure 4.34: Up-converted fluorescence spectrum of the 5 mol% Er^{3+}-doped FZ glass sample. Excitation is carried out with a CW laser diode operating at 1540 nm. The range from 900 down to 400 nm is blown up by a factor of 4 (dashed curve).

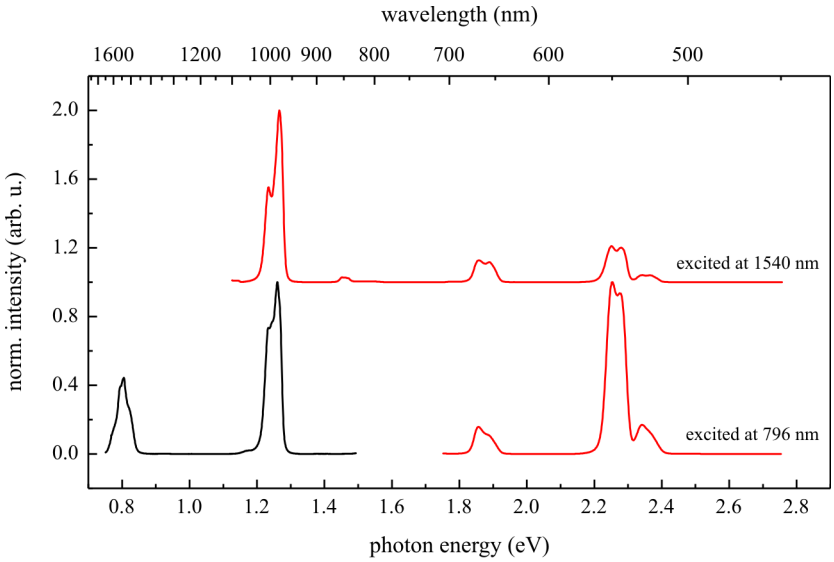

Figure 4.35: The up-converted emission (red) and photoluminescence (black) of Er^{3+}-doped FCZ glass ceramics are shown. The upper curve was excited at 1540 nm, the lower one at 796 nm. All spectra were normalized to their most intense emission. Note: This is no comparison between the up-conversion efficiencies in dependency of the excitation.

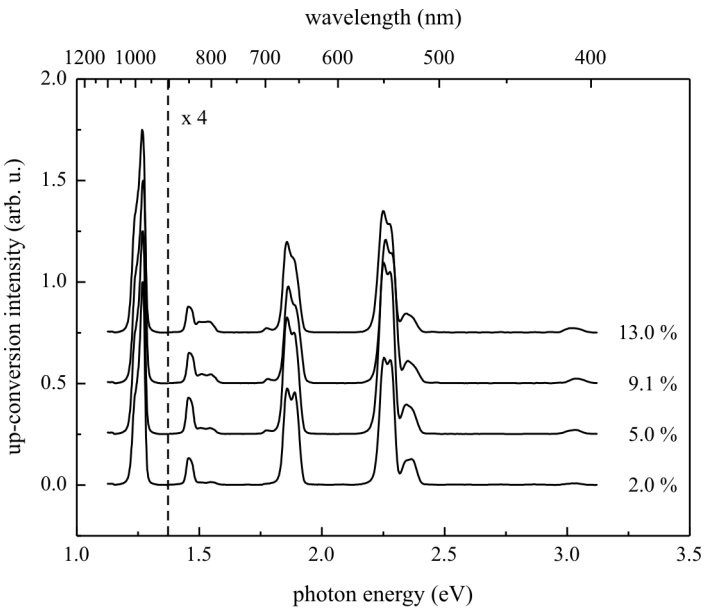

Figure 4.36: Up-converted fluorescence spectra of Er^{3+}-doped FZ glass samples. Excitation is carried out with a CW laser diode operating at 1540 nm (17.2 mW). The range from 900 down to 400 nm is blown up by a factor of 4, the dashed line marks this border at 900 nm.

Converted Fluorescence

Upon 1540 nm excitation with the light of a CW laser diode the Er^{3+}-doped FZ glasses show intense up-conversion. The corresponding spectrum for the 5 mol% doped sample in the spectral range between 400 to 1100 nm can be seen in figure 4.34. Besides the 980 nm emission in the near infrared spectral range, the most intense bands in the visible are located in the green at about 530 and 550 nm. Another emission is located in the red spectral range at 660 nm. The NIR emission at 980 nm can be attributed to a transition from the $^4I_{11/2}$ excited state to the $^4I_{15/2}$ ground state. The weaker emission band between 800 and 830 nm is a combination of two emissions at 820 and 810 nm corresponding to the $^2H_{9/2} \rightarrow {}^4I_{9/2}$ and $^4I_{9/2} \rightarrow {}^4I_{15/2}$ transition, respectively. The $^4I_{9/2}$ and $^4I_{11/2}$ levels are accessible with two and four 1540 nm photons, respectively. The emission at 850 nm is caused by a transition from $^4S_{3/2}$ to the $^4I_{13/2}$ energy level [65]. As shown in [64] the electric dipole transition rate of the 850 nm band is almost three times higher than the one of the 810 nm emission resulting in a higher fluorescence intensity of the 850 nm band. The visible emissions can be attributed to transitions from the $^2H_{11/2}$ (530 nm), $^4S_{3/2}$ (550 nm), and $^4F_{9/2}$ (660 nm) excited states to the $^4I_{15/2}$ ground state. These levels are energetically accessible with three 1540 nm photons. Four-photon up-converted fluorescence can be observed at 415 nm, which arises from a transition of the $^2H_{9/2}$ state to the ground state. In figure 4.33 possible excitation and emission

routes are shown. All transitions to the $^4I_{15/2}$ ground state are split by about 0.03 eV which is caused by the crystal field splitting of the ground state.

Figure 4.35 shows the emission spectra of Er^{3+} doped FCZ glass ceramics. The upper spectrum shows up-conversion when excited with 1540 nm photons. The lower curves were excited at around 796 nm with a different laser diode. All spectra were normalized to their most intense emission. No shift in the position of the emissions can be observed but the intensity ratio changes depending on the excitation wavelength. The weak emission at 850 nm in the up-conversion spectra of the sample excited at 1540 nm cannot be observed in the emission spectra excited at 800 nm.

The up-converted emission spectra of the whole series of different doping concentrations is shown in figure 4.36. All measured curves are normalized to the highest up-conversion intensity at 980 nm. The range from 400 to 900 nm is blown up by a factor of 4, the border at 900 nm is marked with a dashed line. In Nd-doped FCZ samples the main up-conversion emissions were observed in the visible and in the ultraviolet range. Upon increasing the Nd doping level the intensity ratio between the VIS and the UV lines changes in favor of the UV emissions. Fig. 4.36 shows that this trend cannot be observed for the Er-doped FCZ samples: Here, an increased Er doping level did not lead to changes in the intensity ratio between the NIR emission at 980nm and the visible emissions (550 and 660 nm). In contrast, the emission band in the UV (415 nm) and the less intense emission shoulder (around 820 nm) increase with higher doping levels. A closer look at the energy level diagram (figure 4.33) gives the explanation for this similar behavior. Both emission correspond to transitions starting from the energetically high lying $^2H_{9/2}$ energy level (3.05 eV). The 820 nm up-conversion is also a four-photon up-converted emission.

Lifetime Measurements

Lifetime measurements for the two- and three-photon up-converted fluorescence have also been performed. Er^{3+}-doped FZ glasses were excited with a CW laser diode operating at 1540 nm and the up-converted fluorescence decay was detected at 980 nm, 850 nm, 660 nm, and 550 nm. These emissions correspond to transitions starting from the $^4I_{11/2}$ (980 nm), $^4F_{9/2}$ (660 nm), and $^4S_{3/2}$ (550 nm), depopulating to the ground state $^4I_{15/2}$. The 850 nm emission belongs to the $^4S_{3/2} \rightarrow {}^4I_{13/2}$ transition and therefore relaxes from an excited state to another excited state. The up-converted fluorescence decay curves are shown in figure 4.37. For the two-photon up-converted emission at 980 nm a fluorescence decay lifetime of (7.9 $\pm$0.1) ms is determined for the 5 mol% doped sample. All emission starting from an energy level that can only be reached by three 1548 nm photons, $^4F_{9/2}$ (660 nm), $^4S_{3/2}$ (550 nm), and $^2H_{11/2}$ (530 nm), seems to have nearly the same lifetime. Due to the lower signal to noise ratio an exact analysis is not possible. The best fit for these

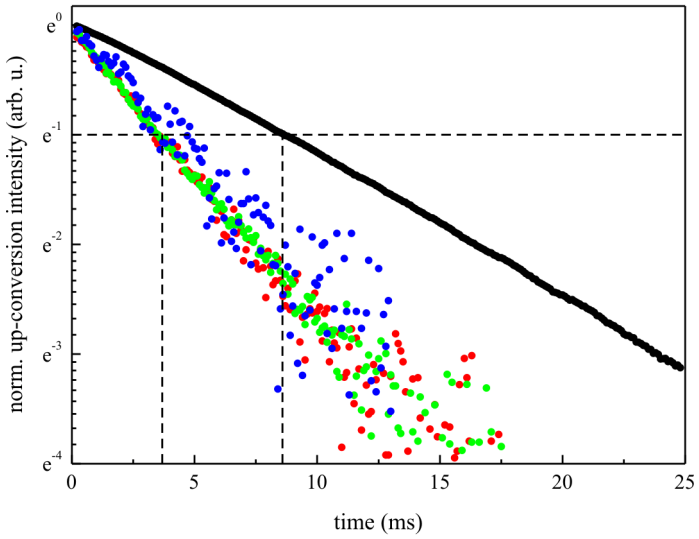

Figure 4.37: Fluorescence decay of Er^{3+} doped ZBLAN glasses. The fluorescence lifetime of the 980 nm emission (black dots), 850 (blue), 660 (red) and 550 nm (green) have been measured. The excitation was carried out with a infrared laser diode at 1540 nm. The signal was modulated with a chopper.

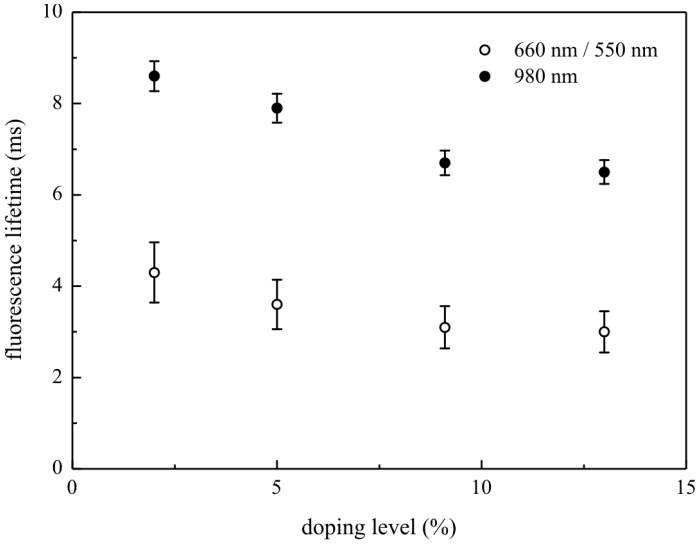

Figure 4.38: Fluorescence lifetimes of the Er^{3+}-doped FZ glasses. The data was extracted from lifetime measurements as shown in figure 4.37.

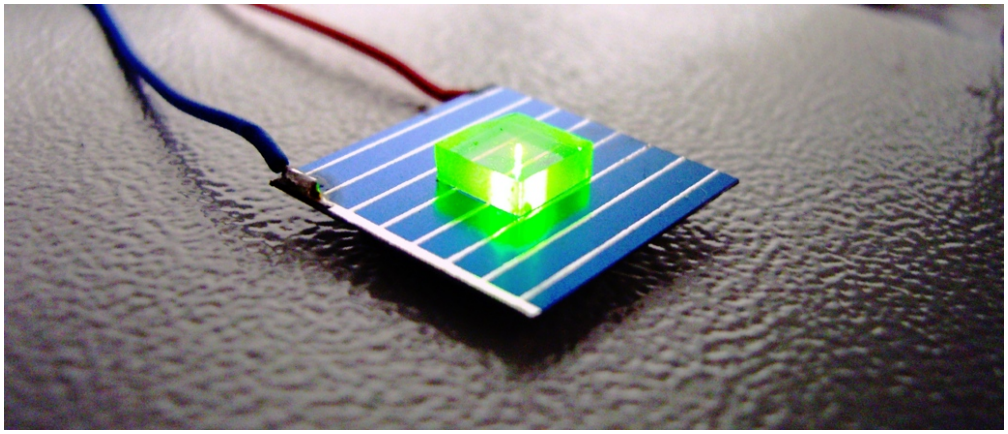

Figure 4.39: Digital photo of the experimental setup. Excitation is carried out from the top with a CW laser diode operating at 1540 nm (not shown). The light is incident perpendicular to the solar cell and the glass sample.

measurements is a lifetime of 3.6 ms with a relatively high error of $\pm$0.5 ms for the measurement of the emission with the lowest intensities (850 nm). The errors for the 660 and 550 nm emission lifetimes are $\pm$0.4 ms and $\pm$0.3 ms, respectively. The fluorescence decay measurements of the other glasses are not shown. The fitted lifetimes are plotted as a function of the doping level in figure 4.38. The lifetimes of the 660 and 550 nm emission are identical within the experimental error. All emissions show the same trend, the higher the doping concentration the shorter the lifetime of the emission. The ratio of the decay times ($\tau_{980\ \mathrm{nm}}/\tau_{660\ \mathrm{nm},550\ \mathrm{nm}}$) is 2.1 $\pm$0.2 for all measurements.

Power Dependence

To measure the power dependence of the Er^{3+}-doped FZ glass the samples were placed on top of a commercial mono-crystalline 2 cm x 2 cm solar cell without any additional optical coupling (see figure 4.39). The power dependence shown in figure 4.40 was measured by recording the short circuit current for different laser diode output power. A short circuit current was observed from 17.2 mW (maximum laser diode output power) down to a few hundred μW. Below this limit the solar cell shows only the dark current induced short circuit current. A direct illumination of the solar cell with a 1540 nm laser diode yields a negligible dark current induced signal. On a double logarithmic scale a saturation of the up-conversion intensity, i.e. the short circuit current can be observed in contrast to the power dependent measurements of the Nd-doped glasses. The point of saturation depends critically on the ratio between excitation power, intermediate energy level lifetime, and the relative contribution of excited state absorption (ESA) and energy transfer up-conversion (ETU) processes to the overall up-converted fluorescence. For the 5 mol% Er-

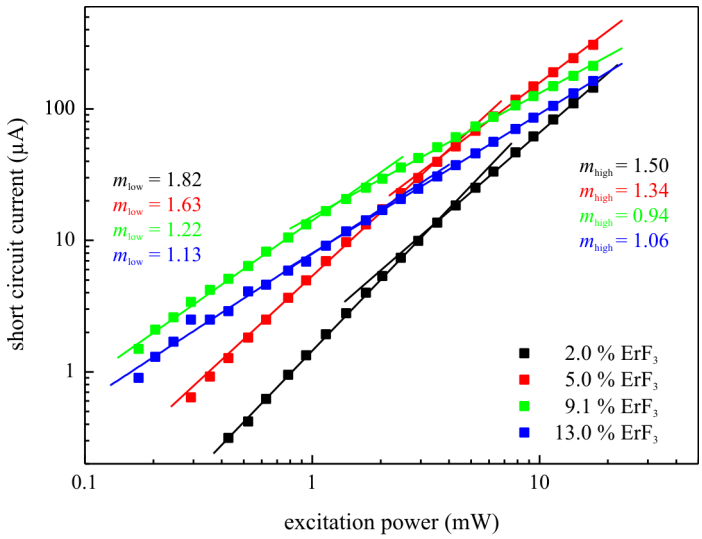

Figure 4.40: Power dependence of the short circuit current (on a double-logarithmic scale) of the up-converted fluorescence intensities in the Er^{3+}-doped FZ glasses, recorded under CW laser diode excitation at 1540 nm. The slopes are fitted for the lower and higher excitation power range.

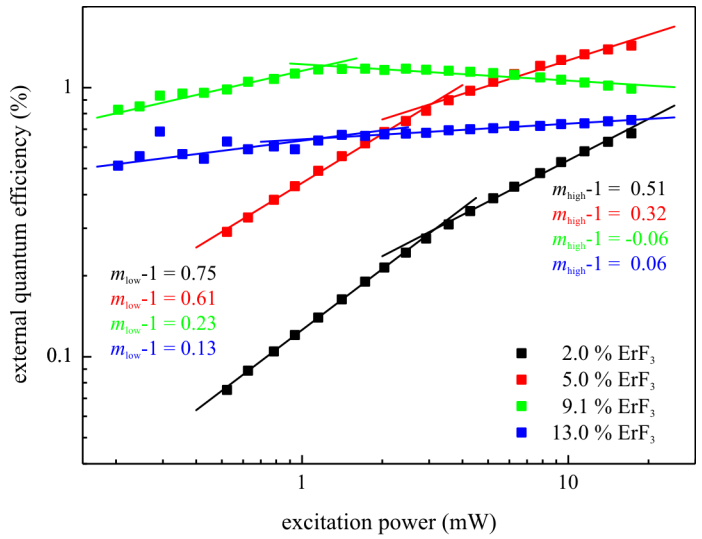

Figure 4.41: Power dependence of the external quantum efficiency (on a double-logarithmic scale) of the Er^{3+}-doped FZ glasses. The samples were excited with a CW laser diode lasing at 1540 nm. The slopes are fitted to two excitation power ranges.

ErF_3	lower excitation power			higher excitation power		
(mol %)	m	$(m-1)_{cal}$	$(m-1)_{meas}$	m	$(m-1)_{cal}$	$(m-1)_{meas}$
2.0	1.82	0.82	0.75	1.50	0.50	0.51
5.0	1.63	0.63	0.61	1.34	0.34	0.32
9.1	1.22	0.22	0.23	0.94	-0.06	-0.06
13.0	1.13	0.13	0.13	1.06	0.06	0.06

Table 4.6: The fitted slopes m of the short circuit current vs. excitation power curves are shown for two excitation power ranges. The calculated $(m-1)_{cal}$ and the fitted data from EQE vs excitation power measurements $(m-1)_{meas}$ are also listed.

doped sample, the slope of the short circuit current versus excitation power curve is $m = 1.6$ and 1.3 in the range from 0.5 to 3 mW and from 3 to 17.2 mW, respectively. This experimentally observed decrease is determined by the competition between linear decay and up-conversion processes for the depletion of the intermediate excited states as shown in section 2.1.2. The intensity of up-converted fluorescence that is excited by the sequential absorption of m photons has a dependence on absorbed excitation power P_{in}, which may range from P_{in}^m in the limit of infinitely small up-conversion rates down to P_{in}^1 for the upper state of infinitely large up-conversion rates [15] (see table 2.2).

From the short circuit current I_{sc} we can also calculate the EQE of this simple and unoptimized system shown in figure 4.39.The EQE is given by equation 2.7:

$$\mathrm{EQE} \quad \propto \quad \frac{\mathrm{I_{sc}}}{P_{in}} \quad \propto \quad \frac{P_{in}^m}{P_{in}} \quad = \quad P_{in}^{m-1}.$$

From this equation the slope of the EQE versus excitation power curve in the double logarithmic plot can be calculated with $m-1$. For the 5 mol% ErF_3 doped sample the slope can be determined as $m-1 = 1.6-1 = 0.6$ in the range from 0.5 to 3 mW and $m-1 = 1.3-1 = 0.3$ for the second range from 3 to 17.2 mW, respectively. This is in good agreement with the experimental data (see figures 4.40 and 4.41) in which the EQE vs. excitation power curves can be fitted with $(m-1)_{meas}$ of 0.61 and 0.32, respectively. For the setup shown in figure 4.39 a maximum short circuit current of more than 300 μA for the 5 mol% doped sample was measured. With an excitation power of 17.2 mW for the laser diode operating at λ = 1540 nm we can obtain a maximum quantum efficiency of almost 1.5 %. All short circuit current and EQE versus excitation power curves of the Er-doped glasses with different doping concentrations were fitted and the results can be seen in table 4.6.

The Er^{3+} absorption band used for this experiment is in the spectral range from 1480 to 1580 nm. In this range the sun has an energy current density of 2.35 mW/cm^2; taken from the AM1.5 spectrum [66]. The exciting laser beam is focused in the experiment with a lens down to a spot of only a few tens of

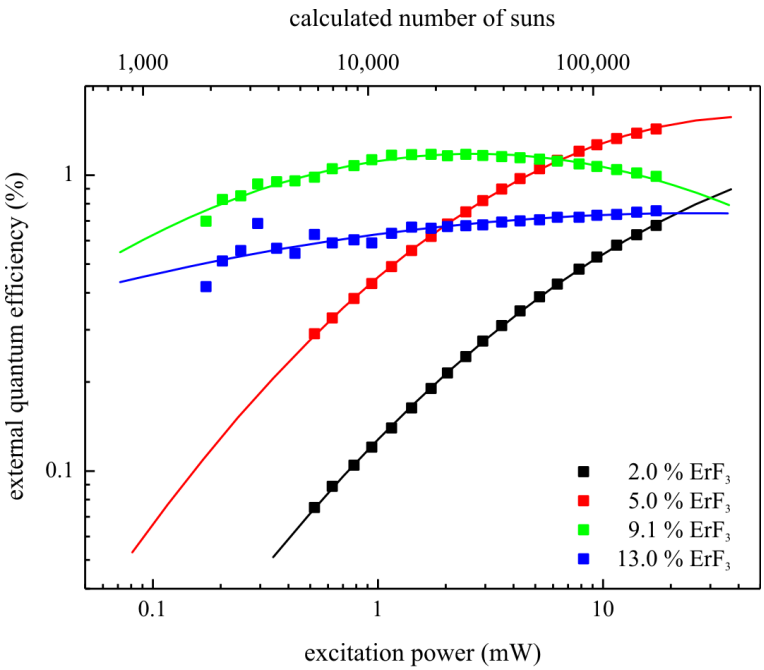

Figure 4.42: Power dependence of the external quantum efficiency (on a double-logarithmic scale) of the Er^{3+}-doped FZ glasses. The lines are second order polynomial fits.

micrometers in diameter; measurements of the spot size with a CCD camera determine 70 μm as the smallest possible spot diameter. Therefore the excitation power of 17.2 mW corresponds to an energy current density of 450 W/cm^2 in this case. Therefore the excitation power of 17.2 mW leads to an energy current density of 190,000 suns or less; depending on the real spot size used in the experiment. For slightly larger spot sizes e.g. a diameter of 100 μm, the energy current density decreases to less than the half, leading to a decrease of the number of the suns. Figure 4.42 shows again the EQE versus excitation power. This time the measured curves are fitted with polynomial to obtain better predictability of their behavior in the range of low excitation power. Additionally, the calculated number of required suns are displayed as a second axis. The real size of the excitation spot is not known for these measurements, therefore the number of suns was calculated with the smallest possible spot size.

The spectral behavior of the Er^{3+} emission, figure 4.43, shows that relative intensity of the up-converted fluorescence bands depends significantly on the excitation power. Upon increasing the excitation power from 0.7 mW to 17.2 mW the relative intensity ratio between the two-photon up-conversion band at 980 nm and the three-photon up-conversion bands at 530, 550, and 660 nm changes in favor of the three-photon up-conversion bands. All spectra were normalized to the 980 nm emission intensity.

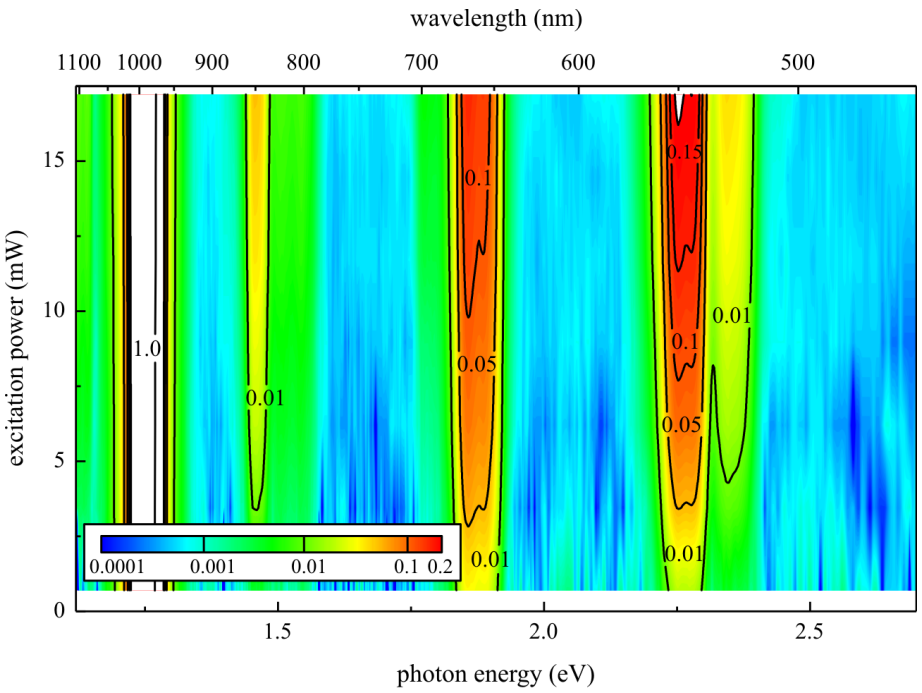

Figure 4.43: Spectral behavior of the Er^{3+} up-converted emission intensity with respect to the excitation power. All spectra of the 5 mol% doped sample were normalized to the 980 nm emission intensity.

4.3.3 Discussion

Optical measurements (figure 4.32 and 4.34) show that trivalent Er can be incorporated into FZ-based glasses. For higher doping concentrations a shift of the glass transition temperature to higher temperatures is observed (figure 4.5) which indicates an influence of the Er doping in the glass on the glass transition temperature. Upon excitation with infrared laser diodes, for both 1540 nm and 796 nm excitation, the doped glasses show an intense up-converted emission (figure 4.36). Due to two-, three-, and four-photon up-conversion processes the Er^{3+} ions are excited to different energy levels leading to emissions over a broad spectral range from the NIR to the UV. Upon increasing the Er doping concentration the up-converted emission, when normalizing to the two-photon up-conversion emission (980 nm), does not change shape or spectral position. The intensities of the emissions in the visible region vary slightly but do not follow a clear trend, whereas the small UV emission becomes more intense.

An important parameter for the up-conversion efficiency is the intermediate energy level lifetime. For the two energy levels, from which the 980 nm two-photon up-conversion and the 660 and 550 nm three-photon up-conversion initiate, a decrease of the lifetime upon higher erbium doping concentrations is observed. It is assumed that this is influenced by quenching effects.

Up-conversion spectra (figure 4.43) show that the relative intensity ratio between the 2-photon up-conversion band and the 3-photon up-conversion bands change in in favor of the 3-photon up-conversion upon increasing the excitation power (from 0.7 to 17.2 mW). This is a clear indicator for saturation of the energy levels involved in the two photon up-conversion. This means that for lower excitation powers higher up-conversion rates are achievable in comparison to the normal fluorescence.

First results of a simple experimental setup (see figure 4.39) with a 5 mol% Er-doped up-converter on a silicon solar cell show that an EQE of 1.5 % can be achieved. Estimations show that for a worst case scenario the excitation power of the laser diode was almost 290,000 suns. For lower excitation power the EQE of the sample decreases rapidly. In contrast to this the higher doped (9.1 and 13 mol%) samples show a maximum EQE of only 1.18 and 0.75 %, respectively, but their great advantage is a more "stable" behavior upon a decrease of the excitation power (figure 4.42). Therefore, they have a calculated EQE of 0.6 and 0.45 %, respectively, for an excitation of 90 μW which equates to incident light of 1,000 suns. This value can be achieved by concentrator cells. State-of-the-art concentrator systems have already reached factors of 1,000. Measurements of these up-converting samples with a concentrator system in combination with a solar light simulator could prove this predictions.

5 Conclusion

Sm-doped $BaCl_2$ and $BaBr_2$ single crystals have been grown for the application of down-conversion. Typical emission and excitation bands of Sm^{2+} are observable. The corresponding fluorescence lifetimes are relatively long about 1.65 ms in $BaCl_2$ and shorter by a factor of three for the $BaBr_2$ single crystals.

Both the fluorescence efficiency and lifetime of Sm^{2+} in FBZ glass ceramics can be significantly increased upon appropriate annealing. The investigation of samples which contain Sm^{2+} and Sm^{3+} ions show that annealing affects the fluorescence properties of Sm^{2+} while leaving those of Sm^{3+} unchanged. The fact that the Sm^{2+} lifetime is increased, but that the Sm^{3+} lifetime does not change within experimental error indicates that a part of the Sm^{2+} present in the glass matrix enters the $BaBr_2$ nanocrystals which are formed during thermal processing. Since the fluorescence lifetimes are increased upon annealing the phonon energies of the $BaBr_2$ nanocrystals are likely to be smaller than those of the FZ base glass, i.e. the non-radiative losses are reduced, the overall measured lifetime is longer and thus the fluorescence is more efficient. However, most of the glasses produced contain Sm^{3+} instead of Sm^{2+} or a combination of both. It was not possible to control the Sm charge state in the FZ glasses.

For up-conversion applications Nd doped materials were investigated. It has been shown that Nd can be incorporated into $BaCl_2$ single crystals. Therein it shows the typical Nd^{3+} emissions and excitations as described in the literature or calculated from the energy level diagram. An additional substructure is observable in the infrared emission which is caused by crystal field splitting. The doped single crystals show up-converted fluorescence in the UV and VIS spectral range under 800 nm laser diode excitation.

The hygroscopicity of $BaCl_2$ is a problem; crystals left for a day or longer in normal air tarnish and become white, lose their physical stability, and crumble on contact. The easiest way to solve this problem is to embed $BaCl_2$ in a protective glass matrix. Therefore, fluorozirconate based glasses containing neodymium and chlorine ions were produced. On subsequent annealing, nano-crystallites were formed in the glasses. The particles can be identified as hexagonal phase $BaCl_2$, which grow in size with increasing annealing temperature. Optical measurements show typical Nd^{3+} transitions and emissions as well as an intense up-conversion in the visible spectral range upon excitation at $\sim$ 800 nm. The spectral positions of these emissions are nearly identical in the glass ceramics but slightly shifted to shorter wavelengths with respect to

the single crystals. Due to the slightly different excitations of Nd-doped single crystals (806 nm) and FZ-glasses (798 nm), it is possible with two different excitation sources (811 and 796 nm) to observe both specific Nd IR emission spectra - with and without crystal field splitting - for the annealed glass ceramics. This is a direct evidence of the incorporation of the Nd^{3+} ions into the nanocrystals during the annealing process. From the split up-conversion emissions (under 796 nm excitation) it is assumed that the up-conversion is mainly effected by the Nd^{3+} ions in the nanocrystals. Additionally, the up-conversion emission intensities in the UV and blue spectral range increase upon annealing. Fluorescence lifetime measurements of the $^4F_{3/2}$ energy level, which is important for the efficiency for the two-photon up-conversion process, show that the lifetime has a significant dependent of the annealing temperature. A lifetime 22 % longer than that in the as-made glass was achieved for an annealed glass ceramic. The power dependency of the the up-converted emissions shows no saturation effects.

Nd-doped glass ceramics are useful as a model system, but are not applicable for silicon solar cells due to the excitation of the up-conversion at $\sim$ 800 nm. However, erbium-doped FZ glasses are more appropriate systems for up-conversion-based silicon solar cells due to their excitation at 1540 nm. The investigated erbium doped fluorozirconate glasses show absorption and up-conversion spectra which can be attributed to the erbium dopant. The strong up-converted fluorescence is emitted in the NIR and in the visible spectral range upon excitation in the IR at around 1540 nm. All up-converted emissions lie energetically above the band gap of Si and can be absorbed by a silicon solar cell, whereas the excitation is below. In a simple experimental setup, an EQE of almost 1.5 % can be achieved for one of the doped FZ glasses. From power-dependent measurements, an EQE of 0.4 % or more is assumed for an excitation from 1,000 times concentrated sunlight.
The next step will be to increase the erbium doping level and to find the optimal sample thickness. Analogous to the results obtained for Nd^{3+}-doped FZ glasses, additional chlorine doping should initiate the crystallization of $BaCl_2$ nanocrystals therein upon thermal processing. This will hopefully lead to a significant increase in the Er^{3+} up-conversion efficiency. Therefore the Er^{3+} doped FZ glasses or FZ glass ceramics have huge potential as an up-converting layer for photovoltaic applications.

A Additional Measurements and Graphs

In these section additional graphs are shown. They contain in contrast to the in the chapters 3 and 4 shown figures more measured data. They are shown to complete the comparison of the different glasses and glass ceramics.

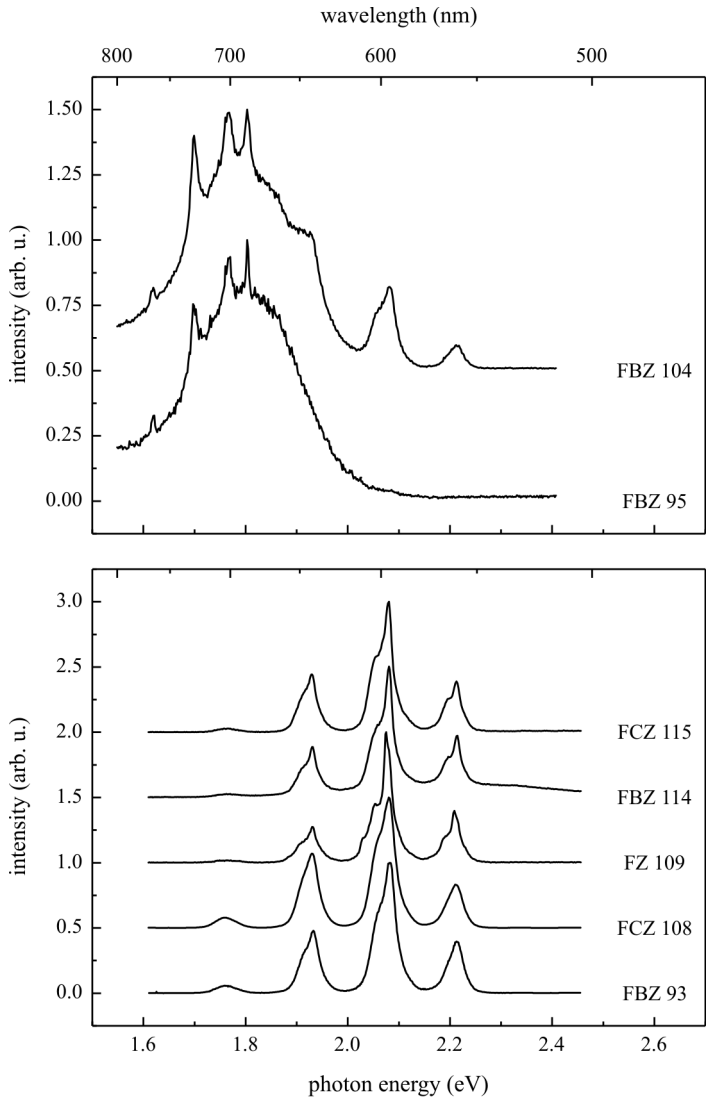

Figure A.1: Emission spectra of all ZBLAN glasses doped with Sm. The measured spectra of the as-made glasses are shown. The upper graph shows the glasses containing Sm^{2+} or $Sm^{2+,3+}$. The lower graph shows the samples with Sm^{3+}.

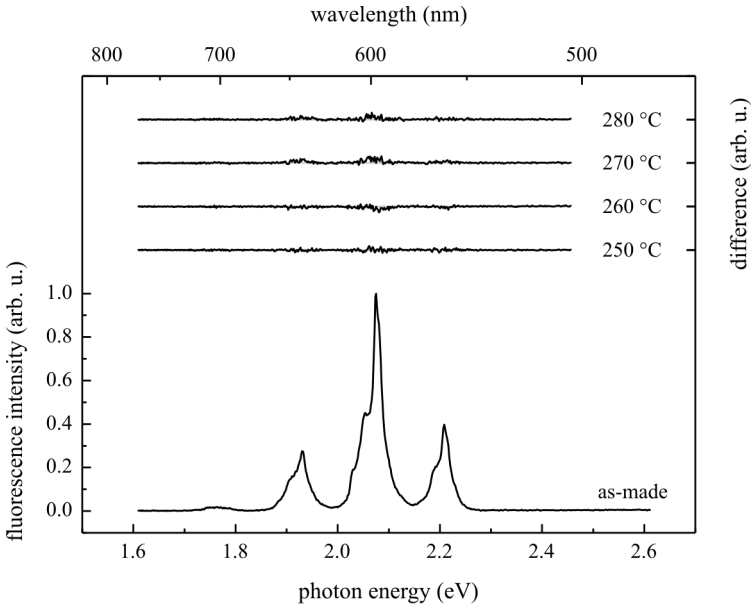

Figure A.2: Emission spectra of FZ 109 glass samples containing Sm^{3+}. The measured spectrum of the as-made glass is shown. For the samples annealed for 20 min at 250 °C, 260 °C, 270 °C, and 280 °C the differences in the signal compared to the as-made glass are plotted.

The first two graphs contain measurements of Sm-doped glasses of the down-conversion chapter. Figure A.1 shows the different produced glasses doped with Sm. Sm^{2+} and/or Sm^{3+} emission spectra were measured. In figure A.2 the differences of the annealed samples of FZ109 are shown in dependency of the annealing temperature.

The both figures A.3 and A.4 shows the measured infrared emission and excitation spectra of the lower (0.5 and 1.0 mol%) Nd-doped glass and glass ceramics.

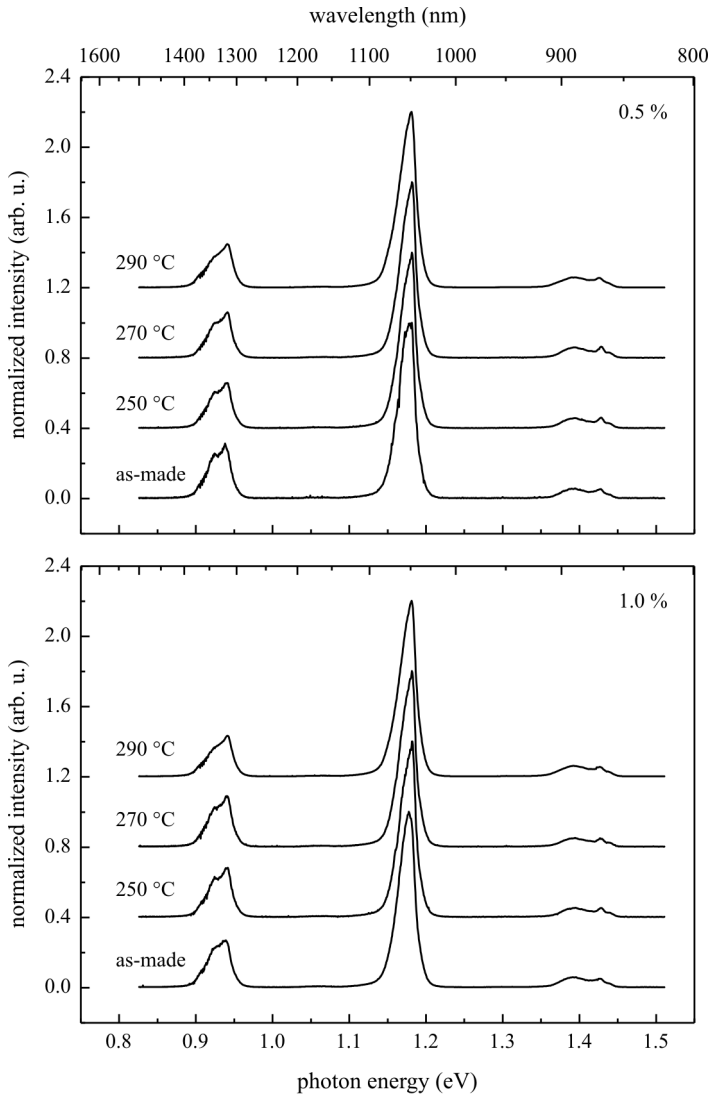

Figure A.3: This figure shows the measured IR emission spectra of annealed glass ceramics doped with 0.5 mol% (upper graph) and 1 mol% (lower graph) Nd^{3+}. From bottom to top the spectra of as-made glass and these annealed for 20 minutes at 250 °C, 270 °C, and 290 °C are shown.

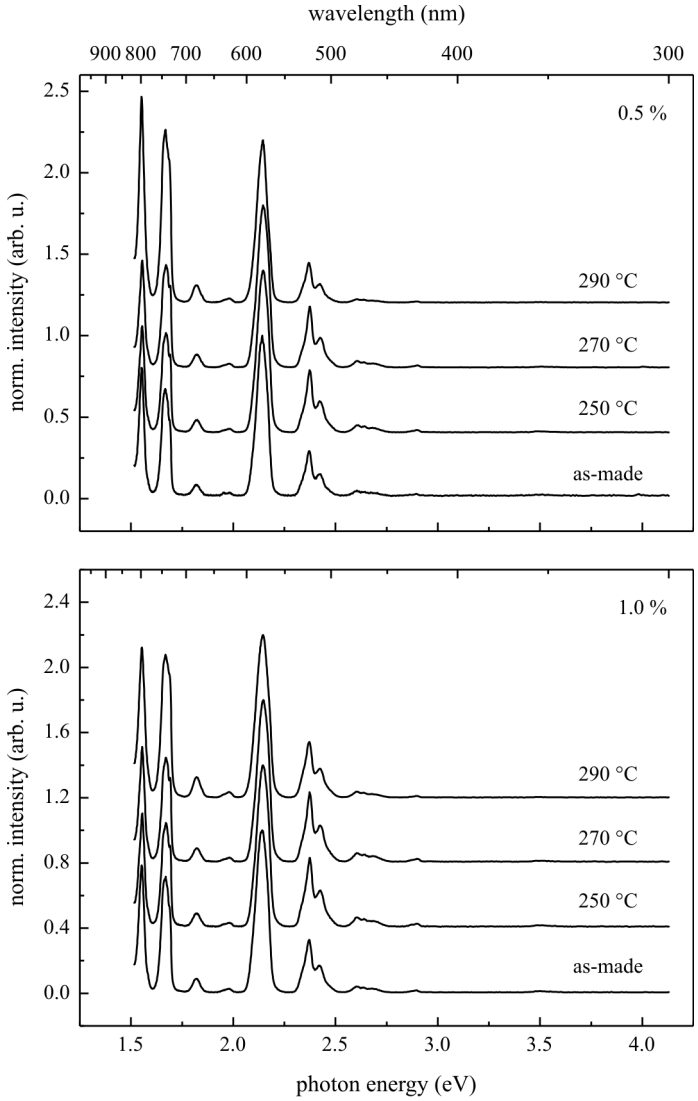

Figure A.4: This figure shows the measured excitation emission spectra of annealed glass ceramics doped with 0.5 mol% (upper graph) and 1 mol% (lower) trivalent Nd. From bottom to top the spectra of as-made glass and these annealed for 20 minutes at 250 °C, 270 °C, and 290 °C are shown.

B Conversion Calculations

Equations

In the calculation model the current of the solar cell (I_{sc}) is given by a convolution:

$$I_{sc} = [S \otimes D_{tr} \oplus D_{abs} \otimes D_{eff} \otimes D_{em}] \otimes \mathrm{EQE} \quad \text{(B.1)}$$

$$I_{sc} = [S \otimes U_{tr} \oplus U_{abs} \otimes U_{eff} \otimes U_{em}] \otimes \mathrm{EQE} \quad \text{(B.2)}$$

where S is the solar spectrum, D_{eff} is the internal quantum efficiency of the down-converter. D_{tr} is the transmission through the down-converter calculated from the given absorption D_{abs}, and D_{em} is the emission of the down-converter. The same coefficients for the up-converter are labeled with U and the corresponding indexes. Note that every part of equations B.1 and B.2 is dependent on the wavelength λ.

To normalize the results of these 2-dimensional parameter spaces, the generated electrons of the normal solar cell system without any additional down- or up-converting layer had to be calculated first. This can be done by setting the absorption of the converting layer to zero.

Assumptions

Trupke *et al.* [5, 6] have performed calculations on the theoretically reachable EQE limit of an undefined single junction solar cell. To get a better overview of the potential of down- and up-converters, more realistic calculations were performed. Instead of an undefined material with a band gap energy varying parameter ([5, 6]), a measured EQE of a silicon detector/solar cell (see figure B.1) was used. In contrast to a 6,000 K blackbody spectrum, an AM1.5 spectrum [66] was taken. Both spectra are shown in figure B.2. Comparing the two regions of interest for conversion processes, it can be seen that the 6000 K blackbody spectrum has in the range from 1000 to 2000 nm $748 \cdot 10^{18}$ more photons than the AM1.5 spectrum, which corresponds to an artificial enhancement of convertible photons of 51.5 %. However, the greatest mismatch can be observed in UV range between 100 and 350 nm. Here the AM1.5 spectrum shows no significant photon flux due to the atmospheric absorbtion. In this region, the blackbody spectrum offers more than 800 % of the real photon flux. Figure B.3 schematically shows the calculation process for down- and up-converter.

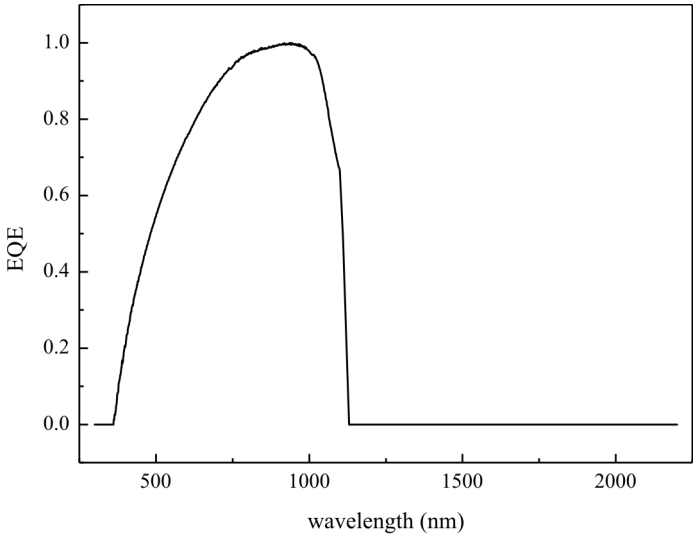

Figure B.1: External quantum efficiency used for the calculations.

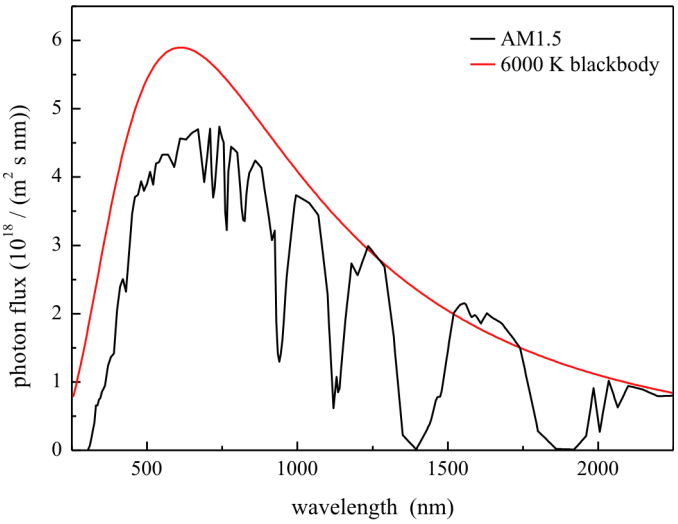

Figure B.2: The AM1.5 spectrum used for the calculations and a 6000 K blackbody spectrum used by Trupke [5, 6].

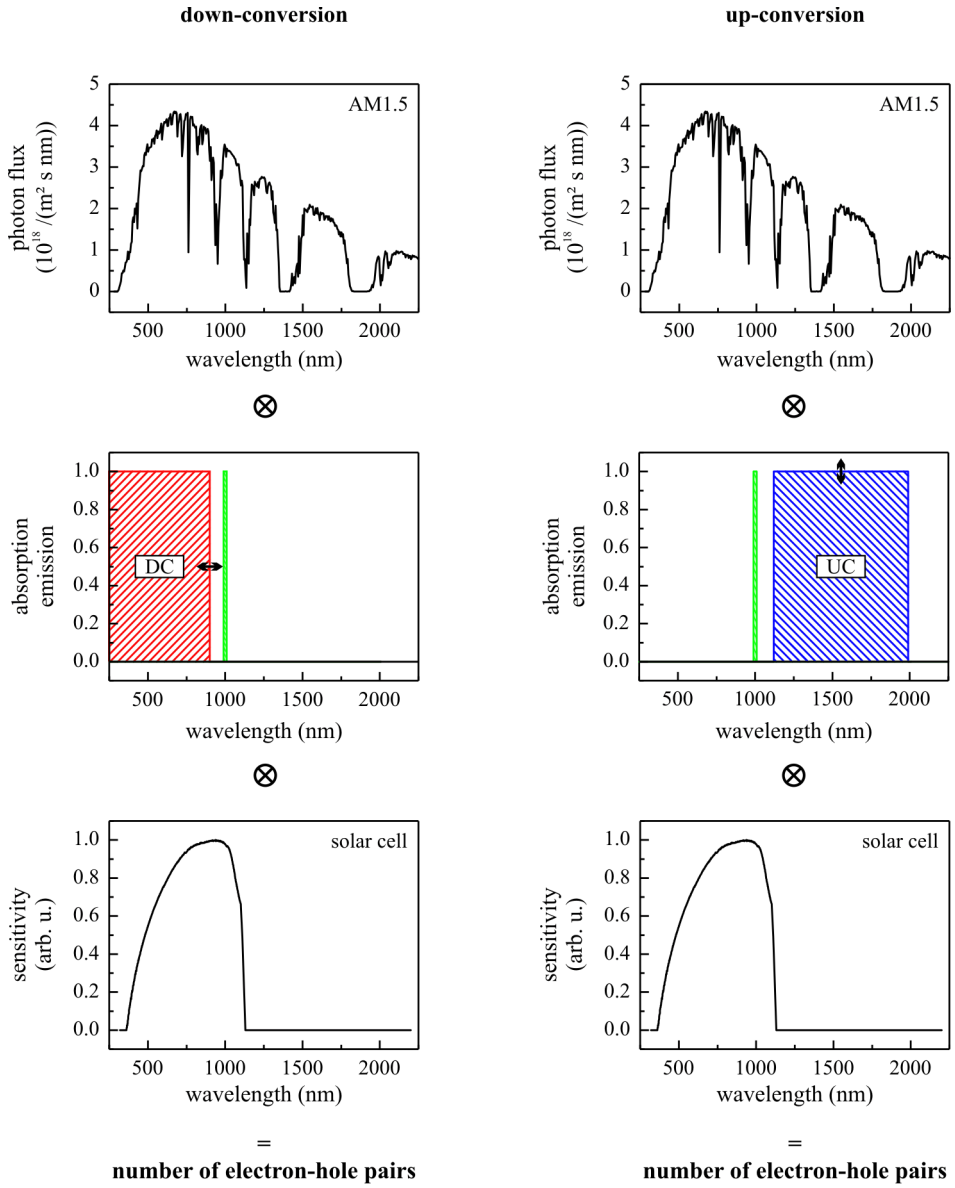

Figure B.3: Down- and up-conversion process simulated with AM1.5 spectrum and real EQE. The absorption range and hight of the converting layers are shown as red (down) and blue (up) colored areas. The converted emission is painted in green and emits at $\sim$ 1000 nm. The absorption band edge or the absorption high for the down- and up-converter calculations, respectively, was varied, as indicated by the arrows.

The optical parameters of the converting layers were chosen as follows:

Down-Conversion: The absorption of the down-converter is defined as:

$$\text{absorption}(\lambda) \quad = \quad \left\{ \begin{array}{cc} 1 & 280\ \text{nm} \leq \lambda \leq b \\ 0 & \text{otherwise} \end{array} \right\}$$

with the wavelength parameter $b = 280 \ldots 900$ nm. The down-converter emits the converted photons at 1000 nm (gauss profile) with an internal quantum efficiency (IQE) of $0 \ldots 100$ %, where an IQE of 100 % means that all incoming photons were converted and emitted.

Up-Conversion: The absorption of the up-converter is defined as:

$$\text{absorption}(\lambda) \quad = \quad \left\{ \begin{array}{cc} a & 1220\ \text{nm} \leq \lambda \leq 2000\ \text{nm} \\ 0 & \text{otherwise} \end{array} \right\}$$

with the absorption parameter $a = 0 \ldots 100$ %. The up-converter emits the converted photons with an IQE of $0 \ldots 100$ %, where an IQE of 100 % means that from 2 incoming photons all were converted and 1 up-converted photons were emitted (two-photon up-conversion). The up-converted photons were emitted at 1000 nm using a Gaussian. Figure B.3 schematically shows the process for down- and up-conversion.

In addition to the calculations shown in chapter 3 and chapter 4 a third system containing a down-converter and a quantum cutting layer was calculated. The result is shown in figure B.4.

Quantum-Cutting: The absorption of the quantum-cutting (QC) and down-converting (DC) layer is defined as:

$$\text{absorption}(\lambda) \quad = \quad \left\{ \begin{array}{ccc} a & 280\ \text{nm} \leq \lambda \leq 500\ \text{nm} & \text{for DC} \\ a & 500\ \text{nm} < \lambda \leq 980\ \text{nm} & \text{for QC} \\ 0 & \text{otherwise} & \end{array} \right\}$$

with the absorption parameter $a = 0 \ldots 100$ %. The quantum-cutter and down-converter emit the converted photons with an IQE of $0 \ldots 100$ %, whereas an IQE of 100 % means that all incoming photons were converted; therefore the quantum-cutter emits two converted photons for one absorbed. The converted photons were emitted at 1000 nm using a Gaussian.

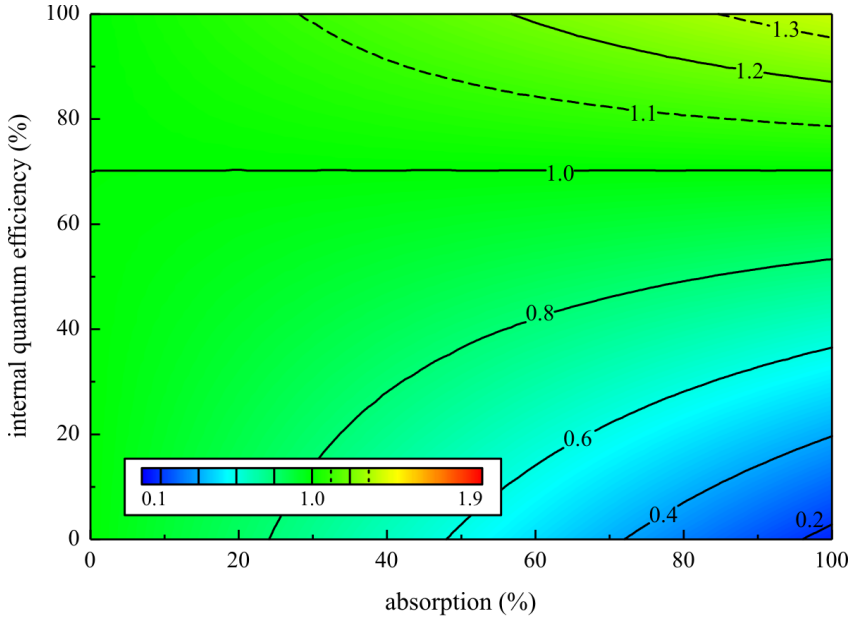

Figure B.4: Calculated ratio between solar cell with and without a down-converting and quantum-cutting layer dependent on the absorption of the layers and the internal quantum efficiencies. A maximum for 100 % absorption and internal quantum efficiency of 1.353 was calculated; 0.167 for the minimum. The color stands for the calculated ratio (see color scale in the lower left corner).

C DSC Measurements and Analysis

Measurements were performed with a NETZSCH DSC 204 F1 and analyzed in combination with the software package NETZSCH PROTEUS V4.8.5.

The glass transition temperature T_g is correlated with the melting temperature T_m by the "two-thirds rule" $T_g/T_m = 2/3$ [67]. The onset, the mathematical beginning of the first crystallization peak, is called T_x and belongs to $BaCl_2$ for the investigated glass. The temperature of the maximum of the crystallization peak is T_p.

$$\Delta T = T_x - T_g \tag{C.1}$$

$$H_r = \left(T_x - T_g\right) / \left(T_m - T_x\right) \tag{C.2}$$

$$S = \left(T_x - T_g\right)\left(T_p - T_x\right) / T_g \tag{C.3}$$

Equation C.2 describes the devitrification tendency of the glass. H_r defined by Hruby [68] informs about the nucleation rate of the crystals embedded in $\left(T_x - T_g\right)$ and the magnitude of growth-rate between T_m and T_x [60]. The parameter S introduced by Saad and Poulain also includes the width of the devitrification peak [69]. If the $\left(T_p - T_x\right)$ factor is high, the growth rate decreases. Moreover DSC measurements with different heating rates (α) make it possible to investigate the apparent activation energy E_a of crystallization and the crystallization kinetics. The activation energy can be determined by equation C.4 [70] or equation C.5 [71].

$$\frac{d\left[\ln\left(T_p^2/\alpha\right)\right]}{d\left(1/T_p\right)} = \frac{E_a}{R} \tag{C.4}$$

$$\frac{d\left(\ln\ \alpha\right)}{d\left(1/T_p\right)} = -\frac{E_a}{R} \tag{C.5}$$

According to the Avrami model ([72–74]), under isothermal conditions and assuming a constant crystallization temperature, the degree phase transition or crystallization x is given by C.6, where K_t is a temperature dependent rate constant depending on the nucleation and growth rate, and n_{Av} is the Avrami exponent reflecting the process dimensionalities. Using the Avrami equation in the double logarithmic form (equation C.7), the parameters n_{Av} and K_t can be determined as the slope and intersection respectively of straight line fits. Jeziorny [75] modified the Avrami equation to account for non-isothermal

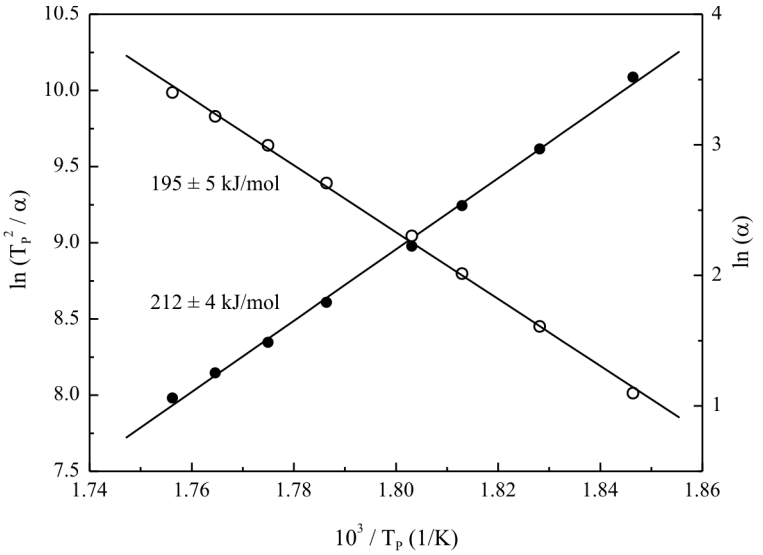

Figure C.1: Plot of $\ln\left(T_p^2/\alpha\right)$ (full circles) and $\ln\alpha$ (open circles) vs. $(1/Tp)$ for the 5 mol% Nd-doped glass. The calculated energies E_α are indicated.

crystallization. Therefore he takes into consideration the influence of heating or cooling rate on the parameter K. The corrected parameter K_c is given by equation C.8.

$$1 - x = \exp(-K_t \cdot t^{n_{Av}}) \tag{C.6}$$

$$\log\left[-\ln\left(1-x\right)\right] = n_{in} \cdot \log(t) + \log\left(K_t\right) \tag{C.7}$$

$$\log\left(K_c\right) = \frac{\log\left(K_t\right)}{\alpha} \tag{C.8}$$

Results

Table C.1 shows important peak values and thermal stability parameters for all heating rates. The activation energy E_a is obtained from the linear fits of the slopes by plotting $\ln\left(T_p^2/\alpha\right)$ or $\ln\ \alpha$ versus $(1/T_p)$ (figure C.1). The results are indicated in the graph and additionally listed in table C.2. The dependence of the relative crystallization x on temperature for different heating rates is shown in figure C.2. To determine the Avrami exponent (n_{Av}) and corrected constant (K_c) the measured data is plotted in a double logarithmic graph and determined by linear fits and equations C.7 and C.8. The mean values n_{Av} listed in table C.2 is $\overline{n}_{Av} \approx 3$ which corresponds for randomly dispersed nuclei in the system with an instantaneous nucleation process in which every nucleus develops into a spherulite [76].

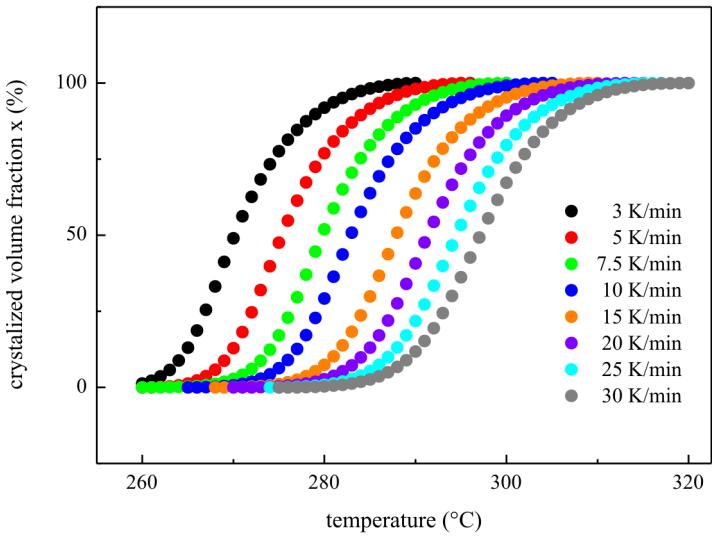

Figure C.2: The relative crystallization x of the glass sample at different heating rates: from 3 K/min to 30 K/min.

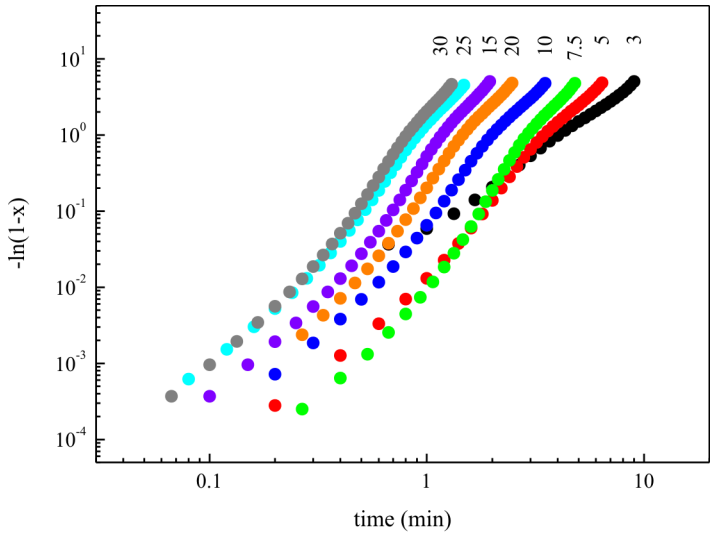

Figure C.3: Avrami plots of the FCZ glass sample for different heating rates.

heating rate	T_g		T_x		T_p		T_m		T_g/T_m	ΔT	H_r	S	$t_{0.5}$	n_{av}	$\log(K_t)$	K_c
(K / min)	(°C)	(K)	(°C)	(K)	(°C)	(K)	(°C)	(K)		(K)		(K)	(s)			
3.0	220.6	493.8	261.2	534.4	268.6	541.8	412.5	685.7	0.720	40.6	0.268	0.686	214.9	1.97	-1.219	0.392
5.0	218.7	491.9	266.1	539.3	274.0	547.2	412.2	685.4	0.718	47.4	0.324	0.762	133.8	3.03	-1.725	0.452
7.5	219.6	492.8	270.2	543.4	278.6	551.8	412.7	685.9	0.718	50.6	0.355	0.863	92.1	3.75	-1.842	0.568
10.0	220.4	493.6	272.9	546.1	281.6	554.8	412.5	685.7	0.720	52.5	0.376	0.926	71.3	3.31	-1.078	0.780
15.0	221.9	495.1	277.5	550.7	286.8	569.0	412.1	685.3	0.722	55.6	0.413	1.045	49.3	3.64	-0.682	0.900
20.0	222.6	495.8	280.6	553.8	290.4	563.6	411.7	684.9	0.724	58.0	0.442	1.147	38.2	3.50	-0.322	0.964
25.0	224.7	497.9	283.4	556.6	293.7	566.9	411.7	684.9	0.727	58.7	0.457	1.215	31.6	3.31	0.077	1.007
30.0	226.4	499.6	285.8	559.0	296.4	569.6	411.7	684.9	0.729	59.4	0.471	1.261	27.2	3.45	0.245	1.019

Table C.1: Thermal stability parameters of the 5 mol% Nd-doped FCZ glasses. Whereas T_g, T_x, T_p, and T_m are given in °C and K.

E_α (Chen)	E_α (Ozawa)	$\overline{n}_{av}$
212 $\pm$4 kJ/mol	195 $\pm$5 kJ/mol	3.25

Table C.2: Activation energy E_a and averaged Avrami exponent of the 5 mol% Nd-doped FCZ glass.

D Bibliography

[1] International Energy Agency (IEA). *Renewables in Global Energy Supply - an IEA Fact Sheer* (2007).

[2] Federal Ministry of Education and Research (BMBF). *The High-Tech Strategy on Climate Protection* (2008).

[3] E. Becquerel. *R. C. Acad. Sci.* **9**, 561 (1839).

[4] M. A. Green, K. Emery, Y. Hishikawa, and W. Warta. *Prog. Photovolt: Res. Appl.* **16**, 435–440 (2008).

[5] T. Trupke, M. A. Green, and P. Würfel. *J. Appl. Phys.* **92**(3), 1668 (2002).

[6] T. Trupke, M. A. Green, and P. Würfel. *J. Appl. Phys.* **92**(7), 4117 (2002).

[7] P. Gibart, F. Auzel, J.-C. Guillaume, and K. Zahraman. *Jpn. J. Appl. Phys.* **35**(8), 4401–4402 (1996).

[8] A. Shalav, B. S. Richards, T. Trupke, K. W. Krämer, and H. U. Güdel. *Appl. Phys. Lett.* **86**, 013505 (2005).

[9] R. T. Wegh, H. Donker, K. D. Oskam, and A. Meijerink. *Science* **283**, 663 (1999).

[10] R. T. Wegh, H. Donker, K. D. Oskam, and A. Meijerink. *J. Lumin.* **82**(2), 93 (1999).

[11] J. L. Sommerdijk, A. Bril, and A. W. de Jager. *J. Lumin.* **8**(4), 341–343 (1974).

[12] W. W. Piper, J. A. DeLuca, and F. S. Ham. *J. Lumin.* **8**(4), 334–348 (1974).

[13] S. Guy, M. F. Joubert, B. Jacquier, and M. Bouazaoui. *Phys. Rev. B* **47**(17), 11001 (1993).

[14] F. Auzel. *The Luminescence of Inorganic Solids*. Plenum Press, New York, (1979).

[15] M. Pollnau, D. R. Gamelin, S. R. Lüthi, H. U. Güdel, and M. P. Hehlen. *Phys. Rev. B* **61**(5), 3337–3346 (2000).

[16] H. G. Wagemann and H. Eschrich. *Photovoltaik*. Vieweg+Teubner Verlag, (2007).

[17] M. Shojiya, M. Takahashi, R. Kanno, Y. Kawamoto, and K. Kadono. *J. Appl. Phys.* **82**(12), 6259 (1997).

[18] M. J. Weber. *Phys. Rev. B* **8**(8), 54 (1973).

[19] C. B. Layne, W. H. Lowdermilk, and M. J. Weber. *Phys. Rev. B* **16**(1), 10 (1977).

[20] M. D. Shinn, W. A. Sibley, M. G. Drexhage, and R. N. Brown. *Phys. Rev. B* **27**(11), 6635 (1983).

[21] I. D. Aggarwal and G. Lu. *Fluoride Glass Fibre Optics*. Academic Press, INC., (1991).

[22] Mi. Poulain, Ma. Poulain, J. Lucas, and P. Brun. *Mater. Res. Bull.* **10**(4), 243 (1975).

[23] J. M. Parker. *Annu. Rev. Mater. Sci.* **19**, 21 (1989).

[24] B. Bendow, M. G. Drexhage, and G. Lipson. *J. Appl. Phys.* **52**(3), 1460 (1981).

[25] B. Bendow, R. N. Brown, M. G. Drexhage, T. J. Loretz, and R. L. Kirk. *Appl. Opt.* **20**(21), 3688 (1981).

[26] C. J. Simmons, H. Sutter, J. H. Simmons, and D. C. Tran. *Mater. Res. Bull.* **17**(9), 1203 (1982).

[27] J. A. Johnson, S. Schweizer, B. Henke, G. Chen, J. Woodford, P. J. Newman, and D. R. MacFarlane. *J. Appl. Phys.* **100**, 034701 (2006).

[28] J. A. Johnson, S. Schweizer, and A. R. Lubinsky. *J. Am. Ceram. Soc.* **90**(3), 693–698 (2007).

[29] P. N. Prasad. *Nanophotonics*. John Wiley & Son, Inc., New Jersey, (2004).

[30] G. H. Dieke and H. M. Crosswhite. *Appl. Opt.* **2**(7), 675–686 (1963).

[31] H. V. Lauer Jr. and F. K. Fong. *The Journal of Chemical Physics* **65**(8), 3108 October (1976).

[32] W. T. Carnall, H. Crosswhite, H. M. Crosswhite, and J. G. Conway. *J. Chem. Phys.* **64**(9), 3582 (1976).

[33] J. A. Koningstein. *Phys. Rev.* **136**(3A), A717 (1964).

[34] C. Görller-Walrand, E. Huygen, K. Binnemans, and L. Fluyt. *J. Phys. B: Condens. Matter* **6**(38), 7797 (1994).

[35] H. M. Crosswhite and R. L. Schwiesow. *J. Chem. Phys.* **50**(11), 5032 (1969).

[36] J. B. Gruber, B. Zandi, and L. Markle. *J. Appl. Phys.* **83**, 1009 (1998).

[37] G. Blasse and B. C. Grabmaier. *Luminescent Materials*. Springer Verlag, Berlin Heidelberg, (1994).

[38] B. M. Walsh, G. W. Grew, and N. P. Barnes. *J. Phys.: Condens. Matter* **17**, 7643 (2005).

[39] P. A. Tanner and C. S. K. Mak. *Phys. Rev. B* **66**, 165203 (2002).

[40] C. Tiseanu, A. Lupei, and V. Lupei. *J. Phys.: Condens. Matter* **7**(44), 8477 (1995).

[41] J. H. van Vleck. *J. Phys. Chem.* **41**(1), 67 (1937).

[42] P. Scherrer. *Nachr. Ges. Wiss. Göttingen* **2**, 98–100 (1918).

[43] J. I. Langford and A. J. C. Wilson. *J. Appl. Cryst.* **11**, 102–113 (1978).

[44] B. E. Warren. *X-Ray Diffraction*. Dover Publications, (1990).

[45] G. S. Ofelt. *J. Chem. Phys.* **38**, 2171 May (1963).

[46] G. Grenet, M. Kibler, A. Gros, J. C. Souillat, and J. C. Gâcon. *Phys. Rev. B* **22**(11), 5052 (1980).

[47] E. B. Brackett, T. E. Brackett, and R. L. Sass. *J. Phys. Chem.* **67**(10), 2132 (1963).

[48] E. Monberg and Y. Ebisuzaki. *J. Cryst. Growth* **21**, 307–309 (1974).

[49] P. Mikhail, K. Ramseyer, G. Frei, F. Budde, and J. Hulliger. *Optical Communications* **188**, 111 (2001).

[50] K. Kojima, A. Kubo, M. Yamashita, N. Wada, T. Tsuneoka, and Y. Komatsubara. *J. Lumin.* **87-89**, 697 (2000).

[51] A. Saissy, N. Azami, J. Jones, and G. Maze. *Appl. Opt.* **36**(24), 5931–5933 (1997).

[52] J. B. Gruber, B. Zandi, and M. F. Reid. *Phys. Rev. B* **60**(23), 15643 (1999).

[53] A. Edgar, S. Schweizer, S. Assmann, J. M. Spaeth, P. J. Newman, and D. R. MacFarlane. *J. Non-Cryst. Solids* **284**, 237 (2001).

[54] G. Liu and H. A. Eick. *J. of the Less Common Metals* **129**, 47 (1989).

[55] A. Edgar, M. Secu, G. V. M. Williams, S. Schweizer, and J.-M. Spaeth. *J. Phys.: Condens. Matter* **13**, 6259–6269 (2001).

[56] W. Shockley and H. J. Queisser. *J. Appl. Phys.* **32**(3), 510–519 (1961).

[57] J. Lucas, M. Chanthanasinh, M. Poulain, M. Poulian, P. Brun, and M. J. Weber. *J. Non-Cryst. Solids* **27**(2), 273–283 (1978).

[58] A. T. Stanley, E. A. Harris, T. M. Searle, and J. M. Parker. *J. Non-Cryst. Solids* **161**, 235–240 (1993).

[59] K. Binnemans, D. Verboven, C. Görller-Walrand, J. Lucas, N. Duhamel-Henry, and J. L. Adam. *J. Non-Cryst. Solids* **204**(2), 178–187 (1996).

[60] M. D. Baró, A. Otero, S. Suriñach, A. Jha, S. Jordery, M. Poulain, A. Soufiane, D. W. Hewak, E. R. Taylor, and D. N. Payne. *Mater. Sci. Eng., A* **179-180**(1), 303 (1994).

[61] S. Schweizer, L. W. Hobbs, M. Secu, J.-M. Spaeth, A. Edgar, and G. V. M. Williams. *Appl. Phys. Lett.* **83**(3), 449 July (2003).

[62] S. Schweizer, L. W. Hobbs, M. Secu, J.-M. Spaeth, A. Edgar, G. V. M. Williams, and J. Hamlin. *J. Appl. Phys.* **97**, 083522 (2005).

[63] J. Selling, S. Schweizer, Spaeth J.-M., G. Corradi, Edgar A., and G. V. M. Williams. *phys. stat. sol (c)* **2**(1), 592 (2005).

[64] S. R. Bullock, B. R. Reddy, P. Venkateswarlu, S. K. Nash-Stevenson, and J. C. Fajardo. *Optical and Quantum Electronics* **29**, 83–92 (1997).

[65] T Catunda, L . A. O. Nunes, A. Florez, Y. Messaddeq, and M. A. Aegerter. *Phys. Rev. B* **53**(10), 6065–6070 (1996).

[66] P. Würfel. *Physics of Solar Cells - From Principles to New Concepts*. WILEY-VCH Verlag GmbH & Co. KGaA, Weinheim, (2005).

[67] W. Kauzmann. *Chem. Rev.* **43 (2)**, 219–256 (1948).

[68] A. Hruby. *Czech. J. Phys. B* **22**, 1187 (1972).

[69] M. Saad and M. Poulain. *Mater. Sci. Forum* **19-20**, 11 (1987).

[70] M.S. Chen. *J. Non-Cryst. Solids* **27**, 257 (1978).

[71] T. Ozawa. *Polymer* **12, Issue 3**, 150–158 (1971).

[72] M. Avrami. *J. Chem. Phys.* **7**(12), 1103 (1939).

[73] M. Avrami. *J. Chem. Phys.* **8**, 212 (1940).

[74] M. Avrami. *J. Chem. Phys.* **9**(2), 177 (1941).

[75] A. Jeziorny. *Polym. J.* **19**(10), 1142–1144 (1978).

[76] Z. Zhang, C. Xiao, and Z. Dong. *Thermochim. Acta* **466**(1-2), 22–28 (2007).

E List of Publications

(1) B. Ahrens, B. Henke, P. T. Miclea, J. A. Johnson, S. Schweizer
Enhanced up-converted fluorescence in fluorozirconate based glass ceramics for high efficiency solar cells
Proceedings of SPIE: Photonics for Solar Energy Systems II, **7002**, 700206 (2008)

(2) B. Ahrens, C. Eisenschmidt, J. A. Johnson, P. T. Miclea, S. Schweizer
Structural and optical investigations of Nd-doped fluorozirconate-based glass ceramics for enhanced upconverted fluorescence
Appl. Phys. Lett., **92**, 061905 (2008)

(3) S. Schweizer, P. T. Miclea, B. Henke, B. Ahrens
Up- and down-conversion in fluorozirconate based glass ceramics for high efficiency solar cells
Proc. of 23rd European Photovoltaic Solar Energy Conference (EU PVSEC), Feria Valencia, Valencia, Spain (2008)

(4) B. Ahrens, J. Selling, C. Eisenschmidt, A. Engel, S. Schweizer
Sm-activated barium halide nanocrystals in fluorozirconate glasses
J. Phys.: Condens. Matter, **20**, 295227 (2008)

(5) B. Ahrens, P. Löper, J. C. Goldschmidt, S. Glunz, B. Henke, P. T. Miclea, S. Schweizer
Neodymium-doped fluorochlorozirconate glasses as an upconversion model system for high efficiency solar cells
Phys. Status Solidi A, **205**, 2822-2830 (2008)

(6) B. Ahrens, P. T. Miclea, S. Schweizer
Upconverted fluorescence in Nd^{3+}-doped barium chloride single crystals
J. Phys.: Condens. Matter, **21**, 125501 (2009)

(7) B. Henke, B. Ahrens, J. A. Johnson, P. T. Miclea, S. Schweizer
Erbium-doped Fluorozirconate Glasses For High Efficiency Solar Cells
Prog. Photovoltaics Res. Appl., (submitted)

(8) B. Henke, B. Ahrens, P. T. Miclea, C. Eisenschmidt, J. A. Johnson, and S. Schweizer
Erbium- and chlorine-doped fluorozirconate-based glasses for up-converted fluorescence
J. Non-Cryst. Solids (accepted)

In Preparation

(1) B. Henke, J. A. Johnson, B. Ahrens, P. T. Miclea, S. Schweizer
Saturation effects in the up-conversion efficiency of Er-doped fluorozirconate glasses
J. Phys.: Condens. Matter

(2) B. Ahrens, B. Henke, J. A. Johnson, P. T. Miclea, S. Schweizer
Upconverted fluorescence in Er-doped fluorozirconate based glass ceramics for high efficiency solar cells
Proc. of SPIE

(3) S. Schweizer, B. Henke, J. A. Johnson, B. Ahrens, P. T. Miclea
Progress on erbium-doped fluorozirconate glass ceramics for upconversion-based solar cells
Proc. of 24th EU PVSEC

F Declaration

Hereby I declare that this submission is my own work and to the best of my knowledge it contains no materials previously published or written by another person, nor material which to a substantial extent has been accepted for the award of any other degree or diploma. Any contribution made to the research by others, with whom I have worked at University of Paderborn or elsewhere, is explicitly acknowledged in the thesis.

I also declare that the intellectual content of this thesis is the product of my own work, except to the extent that assistance from others in the project's design and conception or in style, presentation and linguistic expression is acknowledged.

Date, Location	Bernd Ahrens

G Acknowledgement

Das Deckblatt der Arbeit trägt zwar nur einen Namen dennoch haben viele Menschen zum Gelingen dieser Arbeit beigetragen und mich auf verschiedenste Art und Weise unterstützt.

Ihnen allen sei mein Dank ausgesprochen.

Als erstes möchte ich mich bei Herrn PD DR. STEFAN SCHWEIZER für die Aufnahme in seine Arbeitsgruppe bedanken. Ebenso für die Möglichkeit der Promotion, die immer freundliche, ermutigende, fordernde und fördernde Betreuung.

Herrn PROF. DR. JÖRG LINDNER danke ich für die Übernahme des Koreferats sowie sein Interesse an dieser Arbeit.

Dank möchte ich DR. BASTIAN HENKE und DR. JULIA SELLING aussprechen, gute Kollegen und Freunde, die in jeder Lebenslage ein offenes Ohr haben, sei es wissenschaftlich oder privat. Auch für ihre gute Laune und den damit verbundenen Spaß bei und nach der Arbeit. JÖRG HALLMANN sei im gleichen Atemzug erwähnt und für Selbiges gedankt.

I would like to thank DR. JACQUELINE A. JOHNSON for reading my thesis and correcting the worst misunderstandings between my and the official English caused by grammatical bloomers.

DR. PAUL MICLEA danke ich für zahlreichen und hilfreichen Diskussionen bezüglich meiner teilweise kreativen Auslegung der optischen Spektroskopie und deren Auswertung.

Auch MARCEL DYRBA und CHRISTIAN PASSLICK sei gedankt für unzählige Gespräche und Diskussionen.

Kollektiv geht mein Dank auch an alle (aktuellen und ehemaligen) Mitarbeiter des A4 FLURES (Uni Paderborn) sowie der AG WEHRSPOHN (Uni Halle/Saale) für das immer gute Arbeitsklima, die kurzweiligen Mittagspausen, interessanten Gespräche, neue Experimente, die Kuchenrunden und den Rest.

Den Mitarbeitern der Kristallzucht, Hr. NIGGEMEIER und Hr. WINTERBERG, als auch Herrn PAULI sei mein Dank.

Bedanken möchte ich mich auch bei meinen ehemaligen Kommilitonen, mit denen ich während des Studiums Vorlesungen gehört und zusammen gelernt habe: MARINA PANFILOVA, ELENA TSCHUMAK, STEPHAN BLANKENBURG und STEFAN WIPPERMANN.

Ebenso bedanke ich mich bei allen, die nicht namentlich Erwähnung fanden, aber zum Gelingen dieser Arbeit, physikalisch oder privat, beigetragen haben.

Insbesondere danke ich meinen FREUNDEN, GESCHWISTERN und ELTERN, die mich immer nach besten Kräften unterstützt haben, mich aber auch nicht zweifeln ließen, dass eine Welt außerhalb des Studiums und der Arbeit existiert.

Support

This work was supported by the FhG Internal Programs under Grant No. Attract 692 034. Funding by the German Science Foundation (DFG project PAK88 - NanoSun) and the Federal Ministry of Education and Research (BMBF) within NanoVolt is gratefully acknowledged.